Studies on Shape Defined Pt-alloy Based Nanoparticles for the Electrochemical Reduction of Oxygen

vorgelegt von

Master of Science

Vera Beermann

geb. in Berlin

von der Fakultät II – Mathematik und Naturwissenschaften

der Technischen Universität Berlin

zur Erlangung des akademischen Grades

Doktorin der Naturwissenschaften

Dr. rer. nat.

genehmigte Dissertation

Promotionsausschuss:

Vorsitzende:	Prof. Dr. Maria Andrea Mroginski (Technische Universität Berlin)
Gutachter:	Prof. Dr. Peter Strasser (Technische Universität Berlin)
Gutachter:	Prof. Dr. Andreas Friedrich (Universität Stuttgart)

Tag der wissenschaftlichen Aussprache: 22. November 2018

Berlin 2018

Danksagung

Mein großer Dank gilt Prof. Peter Strasser für die Bereitstellung dieses großartigen und spannenden Themas, die finanzielle und fachliche Unterstützung, aber auch die wissenschaftlichen Freiheiten und das Vertrauen nach eigenen Ideen und Vorstellungen forschen zu dürfen. Zusätzlich möchte ich ihm für die unzähligen Möglichkeiten von Konferenzteilnahmen und für die Motivation und Unterstützung meines Forschungsaufenthalt in der Gruppe von David Muller an der Cornell University danken.

Ich danke Prof. Andreas Friedrich, der sich bereit erklärt hat, meine Arbeit als Gutachter zu bewerten. Mein herzlicher Dank geht auch an Frau Prof. Maria Andrea Mroginski für die Übernahme des Prüfungsvorsitzes.

Marc Heggen und Martin Gocyla möchte ich für die tolle und zuverlässige Zusammenarbeit und die großartigen TEM, STEM und EDX Bilder/Mappings im Rahmen unseres gemeinsamen DFG Projekts danken.

Ich bedanke mich bei Prof. David Muller, Megan Holtz, Elliot Padgett und dem Rest der Muller Gruppe für die lehrreiche, spannenden und tolle Zeit die ich bei und mit ihnen im Sommer 2016 verbracht habe und die guten wissenschaftlichen Diskussionen weit über diese Zeit hinaus.

Ohne meine (ehemaligen) Kollegen der Arbeitsgruppe Strasser wäre die Zeit nicht annähernd so effektiv, lehrreich, produktiv, erträglich und spaßig gewesen. Deswegen gilt mein ganz besonderer Dank all denen: mit denen ich gute wissenschaftlich Diskussionen führen konnte, die mir mit Rat, Tat und Messungen zur Seite standen, mit denen jedes Kicker-match eine willkommene Pause und Ablenkung war, mit denen die ein oder andere gute, feucht-fröhliche Party gefeiert wurde, die die perfekte Konferenz- und Reisebegleitung waren, die für leckeres selbst gekochtes Essen inklusive „Kochkurs“ gesorgt haben, die die Pflanzen in unseren Büro gepflegt, für gute Stimmung und unzählige Lachtränen gesorgt haben, die immer ein offenes Ohr zu allen möglichen Belangen hatten, die nicht nur Kollegen sondern auch gute Freunde geworden sind und die meinen Alltag einfach ein bisschen besser gemacht haben. Danke!

Ich danke Alexandra Martino, Daniel Jalalpoor, Henrike Schmies, Nina Erini, Nhan Nong-Reier, Stefanie Kühl, und Alexander Denisiuk herzlich für das Korrekturlesen meiner Arbeit.
Außerdem gilt mein Dank Sabrina Wenzel für die Unterstützung in organisatorischen Angelegenheiten, Astrid für die unzähligen ICP Messungen, Annegret für die Kaffeepausen, den Kollegen aus der Feinmechanischen Werkstatt für viele Reparaturen und Maßanfertigungen vor allem für das FTIR, Carsten aus der Glasbläserwerkstatt für verschiedenste Glas-Geräte und Axel Schiele für die Reparatur unterschiedlichster Elektronik.

Zuletzt gilt mein Dank meinen guten Freunden aus dem Studium mit denen ich mich immer toll austauschen konnte, meinen engen Freunden aus meinem privaten Umfeld, die immer für mich da waren, meiner Familie und meinem Freund Alex, die mich zu jeder Zeit liebevoll unterstützt haben.

Table of Content

Zusammenfassung

Wasserstoff-Brennstoffzellen stellen eine attraktive Technologie der Energiebereitstellung aus umweltschonenden und nachhaltigen Energiequellen dar. Allerdings werden für ihren Betrieb derzeit noch teure Platin-Katalysatoren verwendet, welche zudem nicht die gewünschte Leistung erbringen. Hauptgrund dafür sind die großen Verluste an der Kathoden-Seite, die die Reduktion von Sauerstoff katalysieren soll. Eine kostengünstige und leistungsstarke Alternative bieten platinbasierte nanoskalige Legierungen, wobei sich Platin-Nickel Legierungen (Pt-Ni) als besonders effizient gezeigt haben. In oktaedrischer Form bieten diese zudem erhöhtes Sauerstoff-Reduktionsvermögen im Vergleich zu ihrem sphärischen Gegenstück.

Ziel dieser Arbeit war es robuste Synthese-Bedingungen zu entwickeln und anzuwenden, um oktaedrisch geformte Pt-Ni Legierungs-Nanopartikel geträgert auf porösem Kohlenstoff (Pt-Ni/C) herzustellen. Verschiedene Variationen sollten es ermöglichen, Struktur-Aktivitätsbeziehungen zu entwickeln und daraus Rückschlüsse auf optimierte Katalysatoroberflächen zu ziehen. Dazu wurde die Partikeloberfläche mit Rhodium (Rh) als drittes Metall dotiert, die Partikel nach der Synthese thermisch behandelt oder die Oberflächen mit Säure verändert. Die verschiedenen Materialien wurden in Bezug auf die Sauerstoff-Reduktionsaktivität und ihre elektrochemische Langzeitstabilität mit Hilfe einer rotierenden Scheibenelektrode getestet. Dotierung mit Rh führte zu einem enormen Stabilitätsgewinn, wohingegen eine thermische Behandlung die Anfangsaktivität der Partikel erhöhte und die Behandlung mit Säure zu Einbußen in der Anfangsaktivität führte. Neben der Zuhilfenahme von verschiedenen physikalischen Charakterisierungsmethoden, konnten vor allem durch fortgeschrittene elektronenmikroskopische Methoden, Röntgenbeugung und Infrarotspektroskopie (IR) atomare Veränderungen und Unterschiede der Materialien festgestellt werden. Dies ermöglichte es Rückschlüsse auf das unterschiedlichen Aktivitäts- und Stabilitätsverhalten zu ziehen.

Ein besonderes Highlight dieser Arbeit stellen die verwendetem *in situ* Methoden dar, wodurch es möglich war, Katalysatoreigenschaften in unterschiedlichen Umgebungen zeitaufgelöst zu untersuchen. Das Verhalten während der thermischen Behandlung wurde mit Hilfe von Röntgendiffraktometrie und Elektronenmikroskopie im Detail untersucht. Das Adsorptionsverhalten von Kohlenstoffmonoxid bei unterschiedlichen elektrochemischen Potentialen wurde mit Hilfe von *in situ* IR Spektroskopie bestimmt und die potentialabhängige Degradation von Pt-Ni/C *in situ* in einer Flüssigzelle im Elektronenmikroskop untersucht.

Die Ergebnisse dieser Arbeit bieten attraktive Ansätze zur Aktivitäts- und Stabilitätsoptimierung von oktaedrisch geformten Pt-Ni Nanopartikeln und verdeutlichen das großes Potential als Verwendung in effizienten und kostengünstigen Brennstoffzellen.

Abstract

Fuel cells represent an almost ideal technology to provide electricity from sustainable energies. However, to date expensive platinum catalysts are used which do not provide sufficient performances at the cathode side where the oxygen reduction reaction (ORR) takes place. A cost-efficient and active alternative is represented by the group of Pt-Ni alloys. Octahedral shaped Pt-Ni alloy nanoparticles exhibit further improved oxygen reduction reaction activities in comparison to their spherical shaped counterparts.

This work dealt with the development and application of robust and reliable synthesis protocols for octahedral shaped Pt-Ni alloy nanoparticles supported on carbon (Pt-Ni/C). Variation of the synthesis should serve to establish structure-activity relationships, which allow drawing conclusions regarding optimized catalyst surfaces. These variations include surface doping of particles with a third metal (Rh), thermal annealing after synthesis or surface treatment with acids. The resulting materials were investigated in terms of their ORR activity and their electrochemical long-term stability using a rotating disc electrode setup. Surface doping with Rh significantly increased the durability, while thermal annealing led to an improved initial activity and acid leaching to a drop in activity. Besides using several physical characterization methods, advanced electron microscopy, X-ray and infra-red (IR) spectroscopy were used to track atomic changes and differences among the materials. From that, substantial conclusions regarding activity and stability characteristics were made.

A highlight of this work was the use of different *in situ* methods, allowing a time-resolved investigation of detailed catalyst characteristics in different environments. Changes during thermal annealing were investigated using X-ray diffraction and electron microscopy. The potential dependent adsorption behavior of carbon monoxide was studied using *in situ* IR spectroscopy. *In situ* liquid electrochemical electron microscopy was applied in order to study the degradation behavior of the material during different potential sequences.

The results of this work provide attractive possibilities to improve the activity and stability of octahedral shaped Pt-Ni nanoparticles and demonstrate the great potential of this group of materials for cost efficient and high performance fuel cell catalysts.

1. Introduction

The global increase in energy demand and the simultaneous rising awareness of the need for safe, sustainable and economically friendly energy sources have initiated a large discussion about future energy sources and supply[1]. Renewable energies such as wind-, hydro- and solar-energy are clean, safe and inexhaustible alternatives in contrast to fossil fuels and nuclear power, which supports the decarbonization of the electricity industry and reducing our society's carbon emissions. However, these energy sources face significant challenges, including a mismatch between peak output and peak demand which results in power grid instabilities[2,3]. Efficient storage systems are needed in order to compensate for the difference between peak and demand., e.g. pumped hydro, compressed air and battery storage systems[4]. Another promising concept is the use of hydrogen as an energy storage and conversion medium. In this concept, when the electricity (produced by renewable sources) surpasses the demand, the excess energy is used to split water into hydrogen and oxygen molecules, converting and storing the energy chemically in the hydrogen molecule. *Vice versa*, when the supply is insufficient for the demand, chemical energy stored in the hydrogen molecule can then be converted into electrical energy *via* the electrochemical reaction in fuel cells (see Scheme 1.1)[5]. These combined systems consist of an electrolyzer, hydrogen storage tanks and a fuel cell. Hydrogen is stored stationary or is distributed, and can later be used as a valuable compound for industrial applications (e.g. ammonia and methanol synthesis, refineries) or in the fuel cell device (see Scheme 1.1).

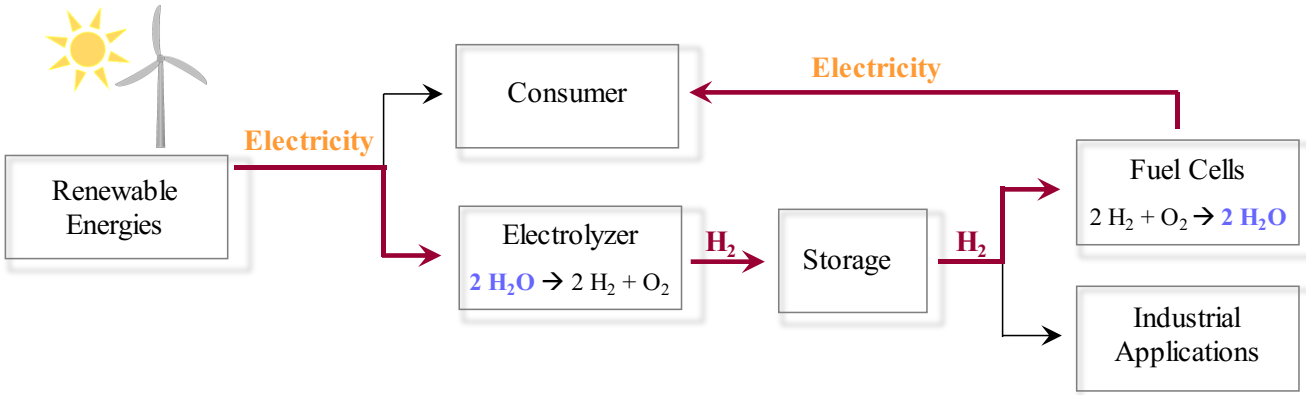

Scheme 1.1 Schematic illustration of possible energy pathways obtained from renewable energies directly to a consumer or *via* electrolyzers, hydrogen storage, hydrogen use in industrial applications, or re-electrification in a fuel cell.

Currently this energy conversion process is accompanied by a significant amount of energy loss. The so-called "round trip efficiency", the product of the overall efficiency for the electrolysis process and the overall efficiency of the fuel cell process, is still as low as 30-40 % using recent technologies[6-9]. The major challenges are ensuring a cost efficient and environmentally conscious production of hydrogen (electrolyzer cells), the development of hydrogen storage systems for stationary and vehicular applications, as well as the costs and efficiency of the fuel cell[5,10]. Due to their quiet operation, reliability, efficient fuel conversion (2-3 times better

than an internal combustion engine), portable character and environmental compatibility, fuel cells are widely accepted and preferred as efficient power generation devices[8,11]. Additionally, their only by-product is water which is becoming very attractive in terms of environmental regulations. For fuel cells, the US department of energy (DOE) defined a set of targets, characteristics and performances goals to meet modern energy and performance requirements[12]. One of the major targets is to lower the costs for fuel cell stacks operating on hydrogen from 26 $/kW$_{net}$ (2015) to 20 $/kW$_{net}$ (2020) and finally to 15 $/kW$_{net}$ as a long-term target. An important parameter influencing the costs is the amount of precious metal on the electrodes, which is currently at 0.16 g/kW and should be reduced to 0.125 g/kW by 2020.

1.1 Proton Exchange Membrane Fuel Cells (PEMFCs) and Oxygen Reduction Reaction (ORR)

The first fuel cell systems were developed by NASA for aerospace programs in the 1960s for efficient power supply and water production[13]. Since then fuel cells have been used for several industrial applications such as backup power for residential and industrial buildings or as power-providing technology in vehicles[14,15]. Emission free, clean and quiet fuel cell busses drive through Cologne and Amsterdam developed in a project funded by the European Union[16]. Fuel cell cars are produced by different manufactures, and already sold in considerable amounts[17,18].

Several types of fuel cells using hydrogen at the anode side and oxygen at the cathode side are known and utilized, such as polymer electrolyte membrane fuel cells (PEMFCs), alkaline fuel cells (AFCs), phosphoric acid fuel cells (PAFCs), molten carbonate fuel cells (MCFCs) or solid oxide fuel cells (SOFCs), which mostly differ in their operating temperature and electrolyte/membrane. Due to its solid electrolyte/membrane (which is corrosion stable), quick start-up potential and low operating temperature of 60 °C the PEMFC is frequently used in stationary and mobile applications[19]. The low operation temperature however is both an advantage and a disadvantage at the same time as it requires expensive electrocatalysts as electrode materials.

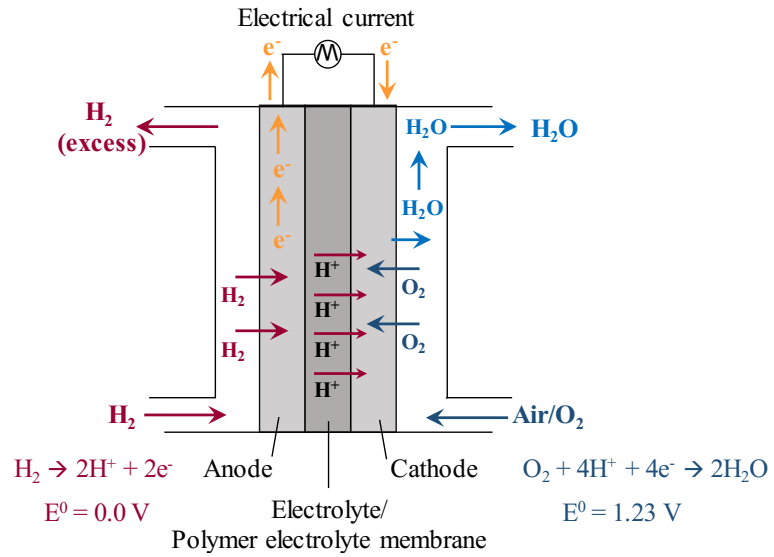

Figure 1.1 Schematic illustration of the working principle of a polymer electrolyte membrane fuel cell and the corresponding reactions taking place at the anode and cathode side.

The general principle of a PEMFC is shown in Figure 1.1. Hydrogen molecules first adsorb on the anode and dissociate into hydrogen atoms, then each atom releases one electron to form a proton (oxidation). The protons pass through a proton conductive membrane to the cathode while the electrons pass through an outer electrical circuit generating electrical current. At the cathode, oxygen adsorbs on the catalyst surface and being reduced

by a 4-electron reduction process. This 4-electron reduction process, the oxygen reduction reaction (ORR), is the bottleneck of the fuel cell performance which will be discussed later.

An ideal single fuel cell would provide a cell voltage of 1.23 V (25 °C, 1 atm), which is reduced to 1.18 V at its operation temperature of 60 °C. As the low cell voltage does commonly not meet the requirements of any consumer, the single cells are stacked, adding up the cell voltage of each cell. Several factors further reduce the cell voltage of each cell: fuel crossover and internal current, Ohmic losses, concentration losses, and activation losses[20]. Activation losses originate directly from the electrode material, the catalyst, itself.

A

(1) $O_2 + 4H^+ + 4e^- + * \longrightarrow OOH^* + 3H^+ + 3e^-$

(2) $OOH^* + 3H^+ + 3e^- \longrightarrow O^* + 2H^+ + 2e^- + H_2O$

(3) $O^* + 2H^+ + 2e^- + H_2O \longrightarrow OH^* + H^+ + e^- + H_2O$

(4) $OH^* + H^+ + e^- + H_2O \longrightarrow 2H_2O$

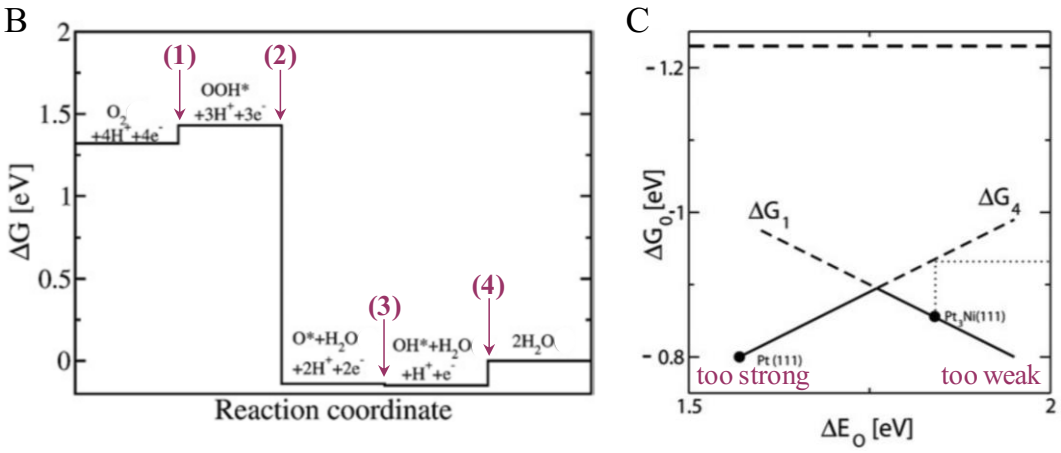

Figure 1.2 Four electron transfer of the oxygen reduction reaction. **A**) Reaction steps with corresponding intermediates and surface adsorbates marked with *. **B)** Free energy diagram of the 4 reaction steps at 0.9 V_{RHE} on a Pt(111) surface with the respective intermediates[21]. C) Volcano plot of the rate determining steps ΔG_1 and ΔG_4 as a function of ΔE_O at E = 0[21]. (Figures B and C adapted from Ref. 21. Reprinted with permission from The Royal Society of Chemistry)

The ORR is the most limiting factor of the fuel cell performance, as it is around 100 times slower than the hydrogen oxidation reaction (HOR) on the anode side. The complex four-electron mechanism proposed for the complete reduction of oxygen to water involves three different adsorption species, which exhibit different adsorption strength to the catalyst surface (Figure 1.2A). First, gaseous oxygen adsorbs on the catalyst surface and an oxygen atom gets protonated coupled to an electron transfer (1). A second proton and electron are transferred to the same oxygen atom, cleave the bond between the oxygen atoms and water is released (2). The remaining adsorbed oxygen is then protonated (3) in two steps (4), again coupled to the transfer of two electrons,

respectively, forming water which gets released[21]. Nowadays, platinum is primarily used as electrode material. On a pure Pt surface however, some intermediates bind too strongly and others bind too weakly and thus, a compromise between adsorption energies has to be achieved in order to obtain high reaction rates.

The calculated free energy changes at 0.9 V_{RHE} associated with each reaction step on Pt(111) surfaces are shown in Figure 1.2B[21]. Steps (1) and (4) are uphill under these conditions and are therefore rate-determining. In step (1) oxygen binds too weakly to the catalyst surface and the protonation is hindered, whereas in step (4) a second proton transfer occurs, resulting in the release of water, which is hindered if the intermediate binds too strong to the catalyst surface. Both of the rate determining steps depend significantly on the adsorption energy of the respective intermediate to the metal surface. The adsorption energy of all intermediates occurring during the ORR can be correlated linearly to the adsorption energy of oxygen (ΔE_O)[22]. The Gibbs free energies of the two rate limiting steps plotted against ΔE_O result in a volcano plot as shown in Figure 1.2C (solid line)[21]. The overpotential for the ORR at a certain adsorption energy is represented by the difference between the dashed vertical line at $\Delta G_0 \approx -1.2$ eV and the respective point on the solid volcano curve. Thus, the optimal compromise between adsorption energies with the lowest overpotential is located at the top of the volcano. In the illustrated example (Figure 1.2C), Pt(111) would bind oxygen species from step (4) too strong and Pt_3Ni(111) oxygen species from step (1) too weak.

1.2 Shape Defined Pt-alloy based ORR Electrocatalysts and their Current Status in Literature

As shown above, for sufficient fuel cell performance the kinetics of the cathode material need significant improvement. Nanoparticles, defined as particles between 1 and 100 nm in size, exhibit an optimized utilization of expensive Pt in comparison to bulk Pt electrodes, due to increased surface area. Recently, technical roadmaps toward reducing the noble metal cost of fuel cell catalysts have involved the transition from pure Pt catalysts to Pt alloys. It has been successfully shown that alloying Pt with 3d transition metals like Fe, Co, Ni, Cu leads to improved activities, reduces the amount of Pt needed for desired fuel cell performance, and reduces the costs[23-34]. Among others, Ni has been shown to be a promising candidate to form alloys with Pt, especially for low Pt-content alloys[28,35,36].

Voltammetric dealloying is an effective concept in order to generate Pt-rich surfaces with 3d transition metal accumulation in the sub-surface and particle core, schematically illustrated with Pt-Ni in Figure 1.3A. A compact Pt-shell is formed for particles with a sufficiently small size and large Pt content. Larger particles tend to form hollow or porous structures[37-39]. The improvement of the ORR activity when alloying and subsequently (surface-) dealloying Pt-M is mostly based on compressive strain effects.

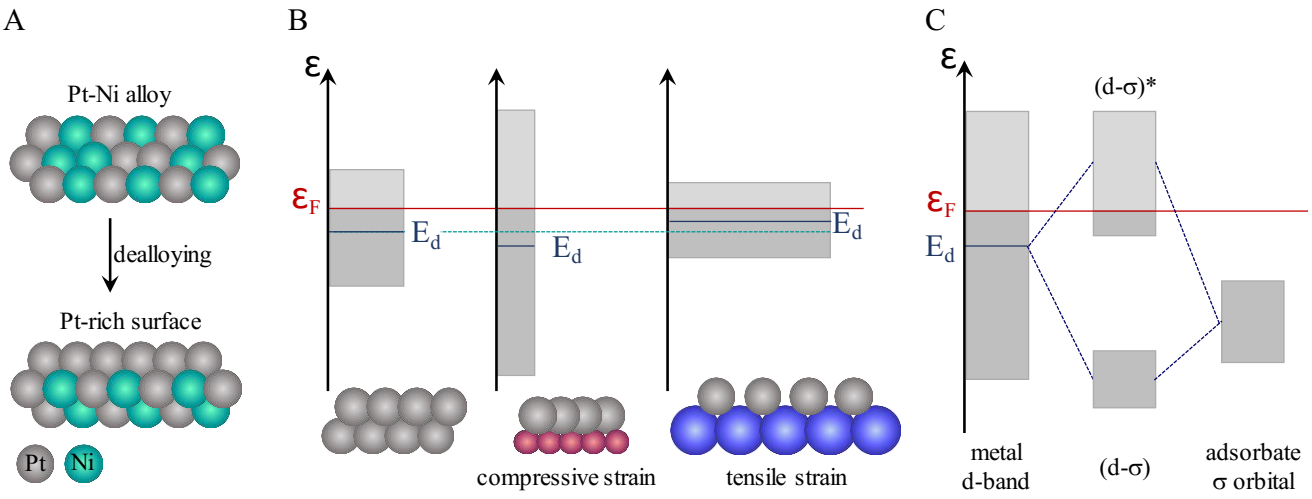

Figure 1.3 Effects of alloying/dealloying on a catalyst surface and its electronic properties. **A)** Schematic illustration of dealloying of a Pt-Ni alloy resulting in a Pt-rich surface. **B)** d-band model showing the shifts of the d-band center resulting from compressive and tensile strain in comparison to the pure metal surface. **C)** Adsorbate metal interaction described by the molecular orbital energy diagram showing the overlap of metal d-band orbitals and the adsorbate σ orbital. The formation of a filled bonding (d-σ) and partially filled antibonding (d-σ)*.

The effect of alloying Pt with 3d transition metals and the resulting change in strain and coordination number of surface atoms, can be qualitatively explained by the d-band model (Figure 1.3B)[40]. Compressive strain in the Pt-rich surface layer, induced by underlying smaller Ni atoms, leads to the expansion of the Pt metal d-band. For

late transition metals the d-band is more than half-filled, thus the Fermi level is energetically higher than the d-band center. In order to preserve the d-band filling when the band is expanding, the whole d-band needs to shift down, resulting in a downshift of the d-band center. Tensile strain has an opposite effect on the position on the d-band center of late transition metals (Figure 1.3B). For early transition metals with a less than half-filled d-bands compressive and tensile strain each have an opposite effect, where an expanded band leads to an up-shift of the d-band center. The position of the d-band center is of fundamental importance for the resulting interaction of the metal surface with an adsorbate as: the binding energy of an adsorbate to a metal surface is mostly determined by the electronic structure of the metal surface. For gaseous adsorption generally, the incompletely filled orbitals of the adsorbate (e.g. 1s state of H_2, 2p state of O_2) interact with the 6s band of Pt, resulting in a low-energy bonding molecular orbital (MO) and an empty antibonding MO. The bonding (d-σ) and an antibonding (d-σ)* states are formed by the hybridization of the metal d-band and the adsorbate orbital as illustrated in Figure 1.3C. The filling of the (d-σ)* state defines the strength of the metal-adsorbate interaction which is influenced by the location of the d-band center with respect to the Fermi level. Therefore, a higher filling of the d-band results in a weaker Pt-adsorbate binding. If the d-band center is shifted to higher energy values, the (d-σ)* state is lower filled, resulting in stronger bonding with an adsorbate. Thus, in case of fuel cell applications, oxygen intermediates that bind too strongly to the pure Pt surface, exhibit lower binding strength when the d-band center is shifted to lower values, which would lead to higher filled (d-σ)* state, reduced binding strength and therefore a reduced overpotential (which is the case for Pt-Ni alloys)[41-44].

Due to the ORR being a structure-sensitive reaction, the electronic structure of a metal surface and the surface geometry of a catalyst are both important parameters that need to be considered in catalyst design. In 2007, Stamenkovic *et al.* demonstrated the different characteristics of certain low index Pt and Pt_3Ni single crystal surfaces and their corresponding ORR activities. For Pt in aqueous $HClO_4$ electrolyte the specific activities increase in the order of Pt(100) << Pt(111) ≈ Pt(110), while for Pt-Ni alloys the order changes to (100) < (110) << (111)[45]. Figure 1.4A illustrates the activity trends achieved for single crystals with different surface orientations in comparison to each other and to pure Pt with the same orientations. These findings stimulated the intensive research on octahedral Pt-Ni nanoparticles enclosing {111} surfaces. Certain nanoparticle shapes imply the preferred exposure of particular surface terminations, such as cubes (100 surfaces) or octahedra (111 surfaces) in cubic symmetries. Combining the benefits of alloying Pt and favorable shapes has resulted in record-breaking activities reported in the decade (Figure 1.4B)[46-51]. In particular, octahedral-shaped Pt-Ni nano-alloys represent a very promisingly active shape-controlled catalyst.

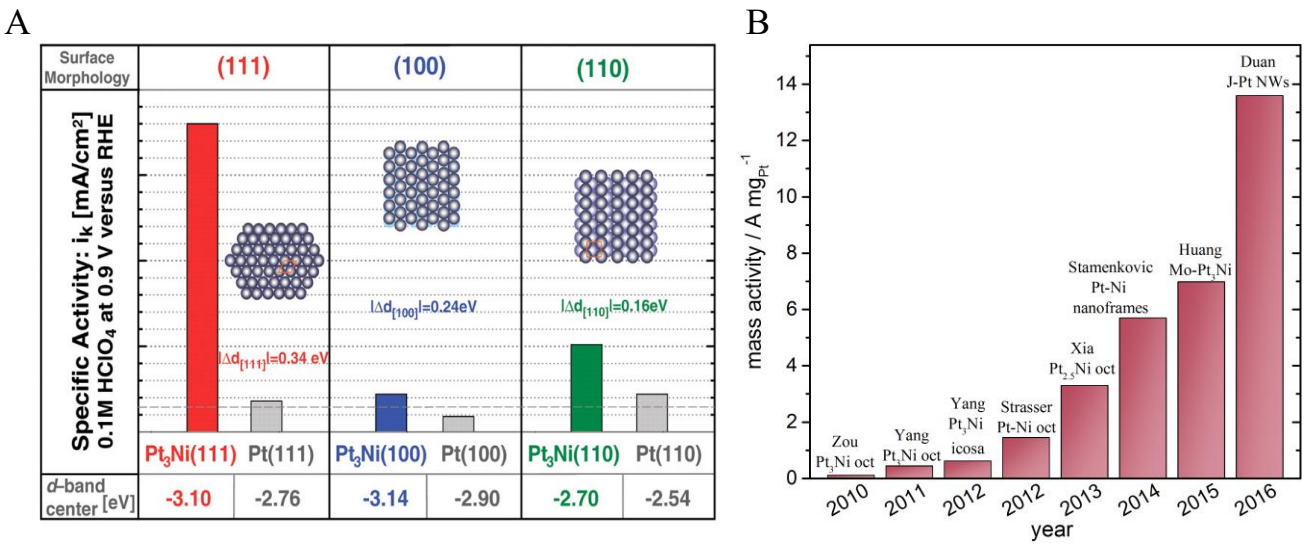

Figure 1.4 Activity Trends on different Pt-based surfaces. **A)** Influence of the different $Pt_3Ni(hkl)$ surface orientations on the electrocatalytic ORR performance measured at 0.9 V_{RHE}. Horizontal dashed gray line corresponds to the specific activity of polycrystalline Pt[45]. Δd(hkl) values indicate the d-band center shift in comparison to the respective Pt(hkl) surfaces. **B)** Evolution of ORR activities in the last years[48-50,52-56]. (Figure A adapted from Reference 45. Reprinted with permission from AAAS)

In 2010, Zhang *et al.* described a successful synthesis of Pt_3Ni nanocubes and octahedra and compared the activities in terms of their (110) and (111) surface structures using a wet chemical synthesis route including long chained surfactants[52]. Three years later the group of Xia was able to achieve Pt-Ni octahedral nanoparticles with a "record breaking" activity of 3.3 A mg_{Pt}^{-1} for the ORR using a similar method[48,57]. Another synthesis for Pt-Ni octahedral nanoparticles was introduced by Cui *et al*. who used a DMF-based solvothermal method. The particles resulting from this method also indicate an exceptional high activity for ORR[47,55,58,59].

While spherical Pt-M alloy fuel cell catalysts are beginning to be deployed in commercial fuel cell applications[60,61], shape-controlled particles still face challenges in terms of stability, especially in the final membrane electrode assembly (MEA) device[60,62]. Shaped Pt-Ni nanoparticles have been observed to quickly lose their octahedral shape after cycling, in part due to nickel dissolution[47,63].

Trimetallic octahedral nanoparticles based on Pt-Ni present a potential class of stable and active nanoparticles. Choi *et al.* reported high activities for Pd@Pt-Ni octahedral nanoparticles with an exceptional durability under ORR conditions[64]. Pt_2CuNi octahedral nanoparticles retain 68 % of their initial ORR activity after 10,000 voltage cycles[65]. Pt-Ni-Co systems also show promising ORR activities and stabilities in comparison to their bi-metallic counterparts[66,67]. For $PtNi_{0.55}Co_{0.1}$/C octahedra a 14.7 times improvement of mass activity in comparison to commercial Pt/C (0.19 A mg_{Pt}^{-1}) was found by Zhao *et al.*[67]. Besides adding a third metal, Pt-Ni octahedral surface doping was shown to be an effective way to maintain highly effective Pt-Ni ORR performances and at the same time improve their stability. A systematic study on octahedral Pt-Ni particles, doped with a set of transition metals has been reported by Huang and co-workers. They found an enhancement in ORR activity and durability in terms of shape and ORR performance after 8,000 potential cycles (still 95 % of the initial activity)

for the particles surface-doped with Mo[50,68]. Recently, doping with other elements such as halides[69] or galium[70] have been shown to improve the durability of octahedral nanoparticles. Li *et al.* discussed Fe-doped octahedral Pt_3Ni nanocrystals which showed a stable octahedral shape after 16,000 potential cycles in acidic media while losing only around 25 % of mass activity[49]. DFT calculations suggest a suppressed surface segregation of Pt-surfaces in the presence of Rh[71]. Yan *et al.* discussed cubic and octahedral Pd-Rh alloys with different metal ratios as stable electro-catalysts for the ORR and obtained the lowest mass-activity loss of only 20 % in acidic media for the most Rh-rich particles, which consist of 80 % Rh and 20 % Pd[50]. Although Rh has a negative influence on the initial activity itself (0.12 A mg_{Pt}^{-1}), it significantly improves the stability towards the ORR.

Another strategy to improve the octahedral shape and performance stability is to employ sufficient post-synthesis treatments such as complex multi-step washing, drying, acid/base treatments or thermal annealing protocols. These treatments tune and change the particles' surface and sub-surface compositions and therefore strongly influence the interfacial catalysis. Besides potentially optimized surface conditions, these procedures offer the opportunity to simultaneously generate clean nanoparticle surfaces. These are often strongly covered with organic surfactants originating from the synthesis and might block ORR reaction sides. Treatment with acid and alkaline solvents have been described to successfully clean, modify, and tune particle surfaces geometries and surface compositions[48,57,63,72] as well as a variety of thermal annealing procedures[73,74]. Arán-Ais *et al.* systematically investigated the influence on the surface elemental composition and the resulting electrochemical responses after treatment of their Pt-Ni octahedral particles with strong acid or base. They found that an alkaline treatment was suitable to clean the particle surface without leaching Ni from the surface while acid treatment generated a Pt rich surface[75]. Annealing was discussed as a powerful tool to induce octahedral facet healing of concave octahedral surfaces by Gan *et al.* With the use of transmission electron microscopy (TEM), Gan *et al.* observed the initial concave octahedral facets become smooth with increasing temperature[76].

Even though shape and performance durability significantly improved, a lot of effort had to be made in order to understand degradation behavior in detail to even further improve catalyst materials. Various physical characterization methods have been used to gain a better understanding of the morphology and composition of fuel cell catalyst materials before and after degradation. Most of the work to date has relied on *ex situ* characterization techniques, often involving scattering from X-ray, light or electrons to describe the material. For fuel cell catalyst nanoparticles, TEM is a popular method to determine the particle shape and distribution on the support material, as well as elemental distribution and stability. Identical location TEM (IL TEM) has been used extensively for Pt-based nanoparticle material to monitor and study changes of identical particles or catalyst parts before and after electrochemical treatment[77-81]. In addition to *ex situ* techniques, there has been a recent surge of interest and capability in *in situ* and *operando* methods that enable probing the material under working conditions, garnering valuable understanding of material operation and degradation[82-94]. Lately, several groups

reported *in situ* electrochemical TEM investigations on fuel cell materials[95,96] and lithium ion battery materials[83,97-101, 102-104]. These experiments typically use liquid-cell systems in conventional TEMs with SiN windows on chips encapsulating a thin liquid layer. Using this powerful tool, it is possible to perform conventional electrochemistry and electrocatalysis while imaging the reactive particles of interest in real time on the nanometer scale, obtaining *operando* information about the nanocatalyst at work.

2. Goals and Objectives

This work aims at investigating Pt-Ni-alloy based shape selected octahedral nanoparticles for the electrocatalytic reduction of oxygen. Using Pt-Ni alloys as a starting material, the investigation focuses on the influence of surface doping with a third metal and post synthesis treatments including thermal annealing and acid treatments. The resulting catalytic activities, as well as shape- and performance stability are studied systematically and attributed to detailed surface and sub-surface characteristics in order to establish reliable structure-activity relationships. Nanoparticles are investigated using advanced electrochemical methods and (*in situ*) spectroscopic methods such as Fourier transformed infra-red (FTIR) spectroscopy and scanning transmission electron microscopy energy dispersive X-ray (STEM EDX) spectroscopy. Electron microscopy is a major technique in order to determine the nanoparticles' shape after preparation and electrochemical application. A detailed understanding of the degradation behavior in order to develop new roadmaps for octahedral nanoparticle designs is one of the major goals. Advanced *in situ* STEM electron microscopy is used to real time image degradation processes of a chosen Pt-Ni octahedral particle system under working conditions in the native electrochemical environment.

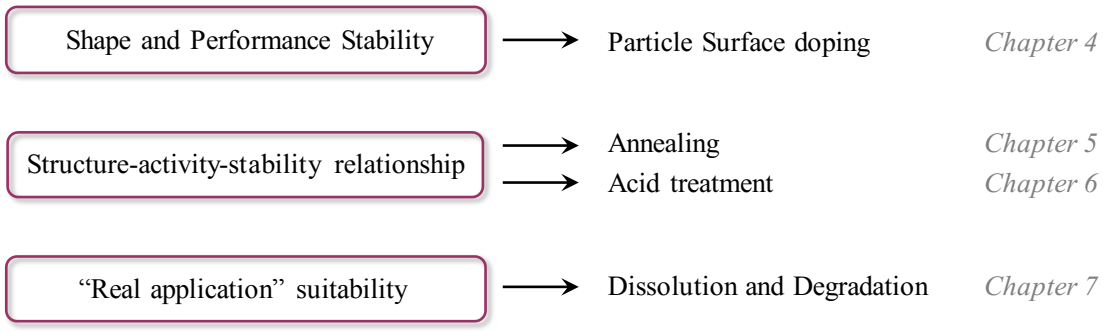

Figure 2.1 Schematic overview of scientific questions and goals dealt with in the course of this work.

As Pt-Ni octahedral nanoparticles suffer from strong degradation, resulting in low shape and performance stability. A novel strategy to enhance both is developed and described in Chapter 4. For this, the octahedral particles are surface doped with Rh and carefully characterized in terms of their shape stability and electrocatalytic ORR performances.

Thermal annealing is frequently used in order to remove remaining organic molecules from the catalyst surface originating from the synthesis, but its impact on the catalyst surface and sub-surface composition and condition is poorly understood. Chapter 5 addresses the effect of thermal annealing on the octahedral nanoparticle surface, the resulting elemental distribution, composition, surface characteristics, and the ORR performances. Advanced (*in situ*) microscopy and spectroscopy in combination with electrochemical surface characterization are used to elucidate delicate surface differences induced by temperature.

A subsequent study described in Chapter 6 investigates another aspect of post synthesis treatments. Here, the impact of an acetic acid treatment coupled to an annealing protocol on the catalytic surface is discussed. Electrochemical CO oxidation voltammetry is used as a probe in order to analyze the nanoparticle surface characteristics and to derive valuable information in terms of catalytic behavior, surface and sub-surface condition, and Pt *versus* Ni enrichment in the surface.

The detailed degradation mechanism of Pt-Ni octahedral nanoparticles is a challenging issue. Therefore, *in situ* liquid electrochemical STEM is used and described in Chapter 7. In contrast to *ex situ* or identical location TEM methods, this enables the exclusion of changes due to drying and transferring to a different atmosphere. A set of different stress protocols were applied in order to study the dissolution and degradation behavior of Pt-Ni octahedral nanoparticles on a second-based time scale.

3. Theoretical Aspects and Experimental Procedures

Experimental Procedures reproduced in part with permission from Nano Lett.*,* **2016**, *16 (3), pp 1719–1725* and J. Am. Chem. Soc., **2017**, *139 (46), pp 16536–16547.*

A List of Chemicals listing Acronyms, Purity/Concentration and Supplier is attached to the Appendix Section at page 120.

3.1 Synthesis of Octahedral Pt-Ni Nanoparticles

The development, investigation, and adjustment of suitable synthesis parameters for Pt-Ni octahedral nanoparticles are of essential importance to carefully study and compare their characteristics. Robust synthesis methods are needed in order to reliably prepare these particles with a narrow size-distribution, homogeneous elemental distribution among the particles and consistent quality. In this work, a wet-chemical synthesis approach was used allowing a careful fine-tuning of the resulting particle characteristics.

3.1.1 Theoretical Aspects

Complex physical processes influence the formation if certain shapes during nanoparticle formation, which are not fully understood yet. For face centered cubic (fcc) single crystal metals Wulff's theorem describes an equilibrium shape of a truncated octahedron (Wulff polyhedron). Shapes of particles prepared in solution under non-equilibrium conditions differ from the expected shape, which is due to changed surface energies by capping agents, impurities, solvents, and defects occurring during nucleation. These effects result in a total free energy, which is lower than the one of the Wulff polyhedron.

The growth of nanoparticles can be generally divided into three distinct stages: (I) nucleation, (II) evolution into seeds, and (III) growth into nanocrystals, as described by LaMer in 1950 (Figure 3.1A)[105]: Zero-valent metal atoms are generated in the nucleation stage (I) in which the metal precursor decomposes. When the concentration metal atoms reaches a point of super saturation (c_{nu}), the atoms start to aggregate and build small seeds, resulting in a drop of concentration of the metal atoms below the super saturation limit (II). Continuous (local) supply of decomposing precursor induces further growth of the seeds into nanocrystals (III). The character of the seeds formed in stage (II) is of fundamental importance for the resulting nanocrystal shape (Figure 3.1B)[106]. Thermodynamic and kinetic factors control the formation of different seed structures, namely single crystal, single twinned, or multiple twinned structure. The thermodynamic control leads to the formation of the most stable particle surface, thus with the smallest interfacial free energy (γ).

$$\gamma = \frac{1}{2} N_b \varepsilon \rho_a \qquad \text{Eq. 1}$$

For the formation of a new surface, crystal symmetry is lost due to broken bonds at the surface. Eq. 1 describes the interfacial free energy given by the number of broken bonds (N_b), the bond strength (ε), and the density of the surface atoms (ρ_a). Seeds further grow to nanocrystals by the supply of metal atoms which is controlled by the competition between the decrease in bulk energy (favoring growth) and an increase in surface energy

(favoring dissolution). Fcc structures with the same lattice constant show the following trend in surface energies: $\gamma_{\{111\}} < \gamma_{\{100\}} < \gamma_{\{110\}}$. This suggests, that the most stable surface is obtained for octahedral nanoparticles enclosing {111} facets. However, octahedra exhibit a larger surface than cubes with the same volume, which promotes the formation of thermodynamically favored cuboctahedral particles. Kinetically controlled multiple twinned seed formation can be realized by keeping the rates of atomic generation sufficiently low using specific reducing agents. Multiple twinned seeds result in decahedrons or icosahedrons by random hexagonal packing (Figure 3.1B)[107].

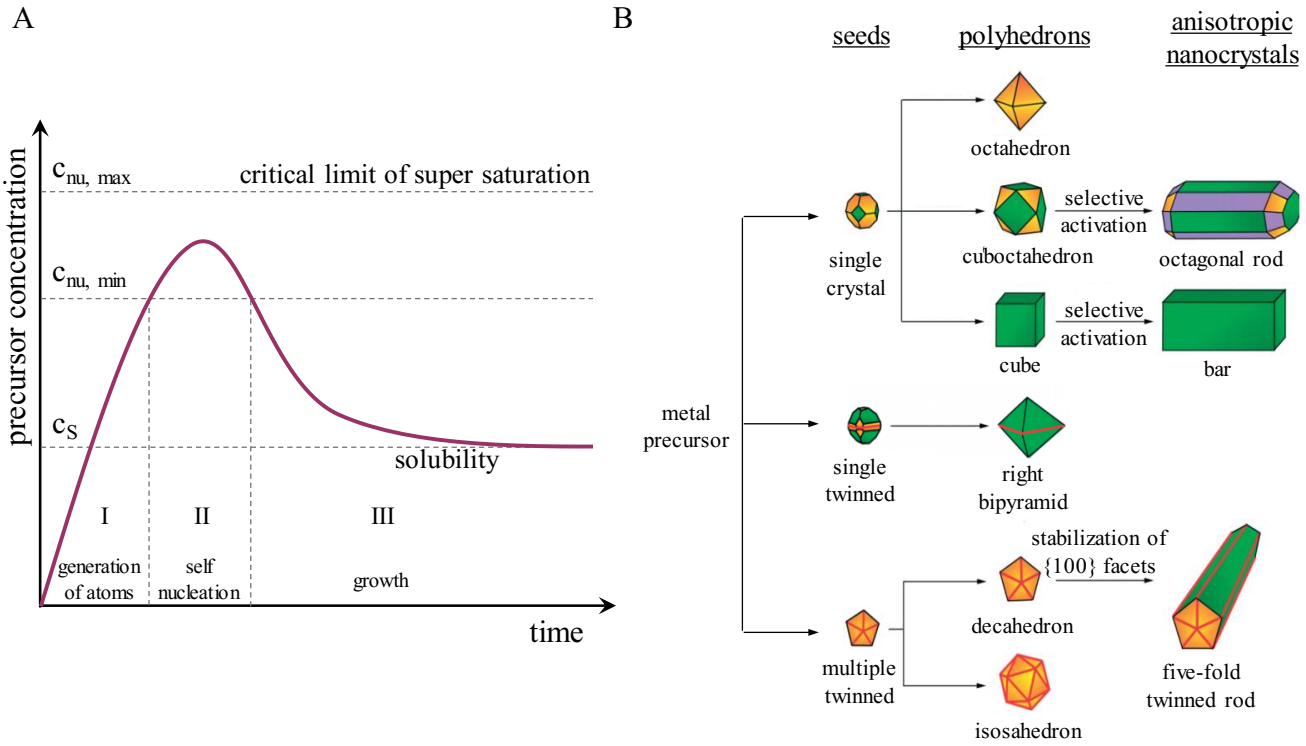

Figure 3.1 Development of nanoparticles: **A)** LaMer's nucleation model showing the concentration of metal atoms *versus* time during nanoparticle formation. First (I), atoms are generated, second (II), atoms nucleate, and third (III), nuclei start to grow. **B)** Possible reaction pathway leading from seeds with single crystal, single twinned, or multiple twinned structures to metal nanocrystals with different shapes, {100} green, {111} orange and {110} purple[106,107]. (Figure B adapted from reference 107. Reprinted with permission from Wiley)

Figure 3.1B illustrates the resulting polyhedron from different seeds. Cubes, cuboctahedra and octahedra grow out of single crystal seeds, while single and multiple twinned seeds form right bipyramids, decahedra or isosahedra. The particle shapes obtained for the polyhedrons are shown in Figure 3.1B. These can be tuned by capping agents, i.e. from gas phase or from the solution. Chemisorption of different species onto the metal nanoparticle surface thermodynamically control the morphological character of the resulting nanoparticles. These capping agents preferentially bind to certain low-index planes like {100}, {110}, and {111} facets and therefore hinder further growth of the respective facet[108]. For example, if the {111} facets of a cuboctahedral particle are blocked the particle continues to grow at the {100} facets, resulting in an octahedral shape providing {111} facets (Figure 3.2). Blocking of the {100} facets would have the opposite effect, resulting in a cubic particle shape.

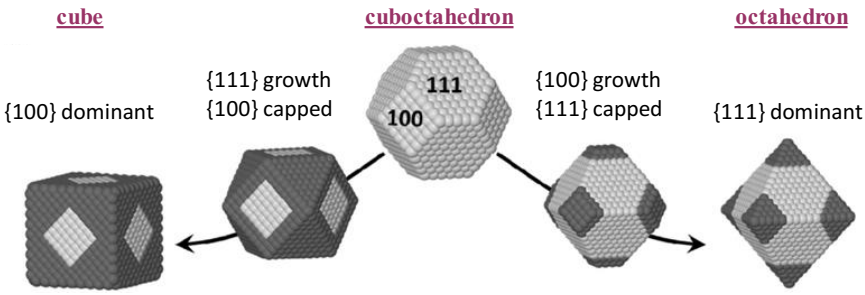

Figure 3.2 Model of the anisotropic growth process of a cuboctahedron exhibiting {111} and {100} facets. Protected {111} facets induce a growth of the {100} facets until only {111} facets are present. If {100} facets are protected, {111} grow until they disappear[109]. (Adapted from reference [109]. Reprinted with permission from Elsevier)

Capping agents can result from the decomposition and release of the metal precursor itself, e.g. anions like acetylacetonate (acac), acetate (OAc) or carbon monoxide (CO), or it can be added to a solution phase synthesis. The chemical interaction of a capping agent with the particle surface controls the free energies of different crystallographic planes and consequently their growth rates. Typical examples for capping agents implemented during the synthesis are oleylamine (OAm), oleic acid (OAc), or polyvinylpyrrolidone (PVP)[108]. A careful choice of synthetic parameters such as reducing agents, capping agent type and concentration, precursor(-anion), reaction temperature, and time open great opportunities to tune and change the morphology of resulting nanoparticles prepared by a wet chemical synthesis approach.

3.1.2 Experimental Procedure

Synthesis of Pt-Ni/C

Pt-Ni octahedral nanoparticles were prepared by adding $Pt(acac)_2$, $Ni(acac)_2$, OAm and OAc into a three-neck-flask under reflux. The reaction mixture was stirred for 10 minutes under nitrogen atmosphere at 60 °C, followed by raising the temperature to 130 °C when $W(CO)_6$ was added rapidly, nitrogen purging was stopped and the reaction mixture was heated to 230 °C and stirred for 50 minutes. (*In of case Pt-Ni-Rh, $Rh(acac)_3$ was added dissolved in 3 mL Bn_2O after 30 minutes and stirring at 230 °C was continued for additional 20 minutes*). Then, the reaction mixture was cooled down to room temperature (RT) and toluene and ethanol were added. The supernatant was removed by centrifugation (7800 rpm for 5 min) and dispersed in toluene. The dispersion was added to a dispersion of Vulcan XC 72R in toluene (total volume ~40 mL). The mixture was cooled in an ice bath and sonicated with an ultrasonic horn for 1 h. Subsequently, ethanol (~10 mL) was added, the catalyst was centrifuged (7800 rpm for 15 min), washed with ethanol (~30 mL) three times, and freeze dried under vacuum for 12 h. The resulting particles were subjected to different post synthesis treatments. Details on amount of substance are listed in Table 3.1.

Table 3.1 Amount of chemical substances used in the synthesis protocols to prepare Pt-Ni octahedral based nanoparticles and the corresponding post synthesis protocols for the respective studies described, investigated and discussed later on in Chapters 4-6.

		Chapter 4		Chapter 5 and 7	Chapter 6
$Pt(acac)_2$	/ mmol	0.102	0.078	0.407	0.407
$Ni(acac)_2$	/ mmol	0.234	0.234	0.934	0.934
$Rh(acac)_3$	/ mmol	0.017	-	-	-
OAm	/ mL	12	12	48	48
OAc	/ mL	8	8	32	32
$W(CO)_6$	/ mmol	0.389	0.389	1.591	1.591
Toluene	/ mL	10	10	20	20
EtOH	/ mL	30	30	60	60
Vulcan	/ mg	40	40	160	160
Post synthesis treatment		*Acetic acid leaching* (30 minutes)		*Annealing* (180, 300 and 500 °C)	1) *Acetic acid leaching* (60 minutes) 2) *Annealing* (300 and 500 °C)

Acetic acid leaching

The supported particles were added to acetic acid (~45 mL) and refluxed for 30 or 60 minutes at 60 °C. After the mixture was cooled down to RT, the particles were washed with ethanol (30 mL) three times and dried for 12 h on air or using a freeze dryer.

Annealing

The obtained powder was heated to 180 °C at a rate of 10 K min^{-1} in a tube furnace in synthetic air atmosphere and left for 30 min. After purging with N_2 for 30 min, the atmosphere was changed to hydrogen (4%/Ar) and the temperature was either held at 180 °C or raised at a rate of 10 K min^{-1} to 300 or 500 °C and left for 1 h. Afterwards it was allowed to cool to RT in N_2.

Synthesis of Pt/C

Platinum nanoparticles were synthesized using a wet-chemical synthesis route based on previous work[27]. $Pt(acac)_2$ (0.6 mmol), 1,2-tetradecanediol (1.2 mmol), OAm (300 µL), OAc (300 µL) were dispersed in dibenzyl ether (50 mL). The mixture was stirred in N_2 atmosphere and the temperature was raised to 80 °C and held for 5 minutes. Afterwards the temperature was raised with a rate of 1 K min^{-1} to 165 °C, kept for 1 h and cooled down to RT. Then, ethanol (30 mL) and DCM (5 mL) were added, Vulcan XC 72R (100 mg) was dispersed in toluene (50 mL) and both were combined. The mixture was stirred overnight. The supernatant was removed by centrifugation (7800 rpm, 15 min) and washed with ethanol (40 mL) three times. The resulting catalyst was freeze dried for 12 h.

Synthesis of Ni/C

Face centered cubic Ni nanoparticles were synthesized using a modified version of the metal oleate route[28]. $NiCl_2 \cdot 6H_2O$ (10 mmol), sodium oleate (20 mmol), Milli-Q water (15 mL), methanol (20 mL) and *n*-Hexane (35 mL) were mixed in a round bottom flask and heated to ~65 °C for 4 h under reflux. The colored upper organic phase containing the Ni-oleate complex was cooled down to RT and washed five times with Milli-Q water in order to remove excess of salt. The Ni-oleate complex (1.4 mmol) was placed in a 3-neck flask and the *n*-hexane phase was evaporated off at 115 °C for 1 h in air. The dry Ni-oleate complex was stirred and redispersed in 1-octadecene (40 mL), oleic acid (0.23 mL, 0.7 mmol) and CTAB (1.4 mmol) and heated to 160 °C for 20 minutes under N_2 atmosphere. The mixture was then heated to 300 °C with a ramping of 5 K min^{-1} for 50 minutes and cooled down to RT using a water bath. Vulcan XC 72R (~20 wt%) was dispersed in *n*-Hexane (40 mL) and ethanol (20 mL) under sonication and the nanoparticles were added dropwise to the carbon under sonication during cooling with an ice bath. The nanoparticle-carbon mixture was left for additional 30 minutes in the sonication bath and for additional 20 h under magnetic stirring at RT. The supported nanoparticles were washed five times in hexane (15 mL) and ethanol (15 mL) and freeze dried for 12 h.

3.2 Electrochemical Methods

Electrochemical characterization methods such as cyclic voltammetry and CO oxidation are of fundamental importance for this work as they allow the careful determination of electrocatalytic surface characteristics and electrochemical stability under operation of the obtained electrocatalytic materials. Furthermore, the electrocatalytic oxygen reduction reaction performance of the materials was identified using linear sweep voltammetry.

3.2.1 Theoretical Aspects

All electrochemical characteristics are investigated using a conventional three-electrode glass cell equipped with a working electrode (WE), a counter electrode (CE) and a reference electrode (RE). Each electrode is placed in separate compartments, all immersed with the same electrolyte and connected to each other *via* a frit. The WE, connected to a rotator, is in the center and the CE and RE on opposite sites. The RE is connected through a Luggin-Haber capillary, building a circuit with high impedance. As a result, only negligible current passes through the RE itself, allowing a constant potential during the measurements. The measured current of the investigated electrochemical reaction passes between WE and CE. The potential difference between the WE and RE is controlled by a potentiostat, retrieving the resulting currents passing through WE and CE.

Cyclic Voltammetry

Cyclic voltammetry (CV) is used in order to characterize the catalyst surface and to obtain an electrochemically stable surface. During this surface conditioning, remaining side products originating from the catalyst preparation are removed and less novel compounds in the catalysts surface are oxidized and dissolved. For this, the potential of the working electrode is linearly changed between an upper and a lower potential with a constant scan rate. The resulting measured currents consist of a Faradaic and a non-Faradaic proportion. Faradaic current occurs when a chemical reaction is taking place, i.e. electrons, are transferred across the electrode-electrolyte interface. The charging and discharging of the electrochemical double layer is a non-faradaic process. The electrochemical double layer can be described as a capacitor, which is built between the charged metal plane of the electrode and a layer of electrolyte ions with the opposite charge. The combination of both currents results in the characteristic fingerprint of the electrochemical surface.

$$ECSA = \frac{Q_{ox}}{Q_{adsorbent}^{theo} \cdot v \cdot m_{cat}} \qquad \text{Eq. 2}$$

The electrochemically active surface area (ECSA) can be determined from the CVs by integrating the Faradaic currents over the respective potential range. The resulting charges (Q_{ox}) are normalized to the product of the charge of the respective adsorbent ($Q_{adsorbent}^{theo}$), the scan rate (v) and the mass of catalyst material (m_{cat}) according to Eq. 2.

For the electrochemical surface characterization of Pt-based systems, common surface adsorbates are hydrogen and carbon monoxide (CO). Hydrogen under potential deposition (H_{upd}) happens during electrochemical potential cycling in aqueous electrolyte according to Eq. 3 (in acidic medium).

$$H_3O^+ + Pt + e^- \leftrightarrow Pt - H + H_2O \qquad \text{Eq. 3}$$

From the resulting CVs the ECSA is determined by integrating the area below the current profile caused by the desorption of hydrogen between ~0.05 and 0.4 V_{RHE} from the under potentially deposited hydrogen, subtracting the capacitive current and normalizing it to 210 µC cm^{-2} (Q_H^{theo}) for a single electron transfer process according to Eq. 3.

The adsorption and subsequent oxidation of carbon monoxide takes place according to Eq. 4. The resulting CO oxidation peak at around 0.7 V_{RHE} is integrated and normalized to 420 µC cm^{-2} (Q_{CO}^{theo}) for a two electron transfer process according to Eq. 2.

$$Pt - CO + 3H_2O \leftrightarrow CO_2 + Pt + 2H_3O^+ + 2e^- \qquad \text{Eq. 4}$$

The adsorption and oxidation of different probe molecules provides not only information about the ECSA but also about surface and sub-surface characteristics of electrochemical surfaces. Characteristic redox waves and current peaks occurring during potential cycling provide additional information about the presence of different surface geometries.

One prominent example, the cyclic voltammograms of Pt nanoparticles with different shapes exposing certain surface geometries were described and discussed by Solla-Gullón *et al.* (Figure 3.3).

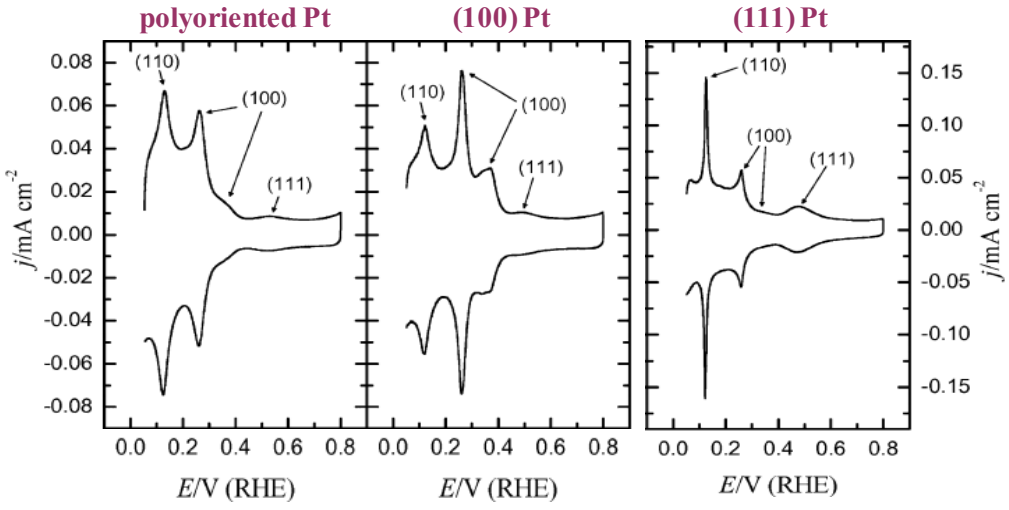

Figure 3.3 Cyclic voltammograms of Pt nanoparticles with different surface geometries. Polyoriented Pt, (100) Pt, and (111) Pt surfaces measured in 0.5 M H_2SO_4 with 50 mV s^{-1} scanrate[110]. (Adapted from Ref. [110]. Reprinted with permission from The Royal Society of Chemistry)

The voltammogram for the semi-spherical polyoriented Pt nanoparticles shows adsorption states at 0.12 and 0.27 V_{RHE} related to (110) and (100) sites. An additional small shoulder is present at 0.35 V_{RHE}, which is associated with (100) terraces. Adsorption also happens at around 0.5 V_{RHE}, provoked by some ordered (111) domains. The described domains reflect different surface compositions of the nanoparticle surface. Preferentially cubic (100) Pt particles show a main peak at 0.27 V caused by (100) edges and corners of the Pt surface sites which is more pronounced than for the polyoriented Pt nanoparticles. This is in agreement with the cubic shape of the particles. Pt nanoparticles featuring mostly tetrahedral and octahedral shaped nanoparticles with (111) Pt domains, show sharp peaks at 0.12 and 0.5 V_{RHE}. Less intensive peaks are present between 0.35-0.38 V_{RHE} representing the (100) surface domains cause by edges and corners between (111) surfaces. This study illustrates the meaningfulness of cyclic voltammetry in order to derive information about surface characteristic of Pt-based nanoparticles[110].

Linear Sweep Voltammetry

Linear sweep voltammetry (LSV) is used to determine the electrocatalytic performance of a catalyst. In contrast to the cyclic voltammetry, the potential is linearly changed in one direction with a constant scan rate. For the determination of the ORR activity of Pt-based systems, an anodic potential scan from 0.05 to ≤1.0 V_{RHE} is used. For the evaluation of the resulting voltammogram the kinetic current density (j_{kin}) is calculated according to Eq. 5

$$\frac{1}{j} = \frac{1}{j_{kin}} + \frac{1}{j_D} \qquad \text{Eq. 5.}$$

The diffusion limited current density (j_D) is taken from the diffusion limited region with constant current density of the LSV between ~0.05 and ~0.6 V_{RHE}. For Pt-based systems, the current density (j) is widely agreed to read off in the linear region at 0.9 V_{RHE}. The resulting kinetic current density can further be normalized to the ECSA, giving the specific activity (j_s) or to the amount of Pt or Pt-group metals (PGM) on the electrode, resulting in the mass based activity (j_m).

3.2.2 Experimental Procedure

A 5 mm diameter glassy carbon electrode coated with the respective catalyst material was used as WE. The CE was a Pt gauze providing a large surface area to minimize current limitations and the RE (mercury/mercury sulfate, Hg/Hg_2SO_4, MMS, 0.722 V_{RHE}) was freshly calibrated before each measurement. 0.1 M $HClO_4$ (diluted from 70 % conc. $HClO_4$ with milli-Q water) was used as electrolyte. All measurements were performed with a BioLogics Science Instruments potentiostat SP-150 and SP-200.

To prepare the WE, an ink was coated on the glassy carbon electrode. Therefore, 3 mg of the catalyst powder (~20 $wt\%_{Pt}$) was dispersed into 2.5 mL milli-Q water, 20 µL Nafion and 0.5 mL *iso*-propanol using a

probe-sonifier. 10 µL of the resulting dispersion was dropped on a pre-cleaned and polished glassy carbon electrode to achieve a Pt loading of ~10 µg cm^{-2}. The ink on the electrode was allowed to dry at 60 °C for 10 min.

For every electrochemical measurement, the WE was lowered at a potential of 0.05 V_{RHE} into the electrolyte. CV was performed in nitrogen (N_2) saturated electrolyte between 0.05 and 1.0 V_{RHE} with 100 mV s^{-1} and 0 rpm. After approximately 20 cycles, a constant CV was obtained. For CO oxidation, the WE was held at 0.05 V_{RHE} with a rotation speed of 400 rpm in CO saturated electrolyte until a very low constant current was achieved (~5 min) and CO was removed from the electrolyte with N_2 effervescing. Three CVs in N_2 saturated electrolyte between 0.05 and 1.0 V_{RHE} with 50 mV s^{-1} and 0 rpm were recorded. After electrode-conditioning LSV was performed between 0.05 and 1.0 V_{RHE} in anodic direction with 5 mV s^{-1} and 1600 rpm in O_2 saturated electrolyte. Stability measurements of 4k and 8k cycles were performed by cycling between 0.5 and 1.0 V_{RHE} with 50 mV s^{-1} and between 0.6 and 1.0 V_{RHE} with 100 mV s^{-1} for 30k cycles, all in N_2 saturated electrolyte with 0 rpm.

All potentials presented are iR corrected, where the uncompensated ohmic resistance (R) was determined by potentiostatic electrochemical impedance spectroscopy (PEIS) at 0.4 V_{RHE} in N_2 saturated electrolyte.

3.3 (*In situ*) (Scanning) Transmission Electron Microscopy

In this work, conventional Transmission Electron Microscopy (TEM) was used in order to (1) check for the nanoparticle distribution on the carbon support surface, (2) study and identify the nanoparticle shape, and (3) determine the particle size of the initial material, after electrochemical testing, acid leaching, and thermal treatments. Advanced electron microscopy such as High Angle Annular Dark Field Scanning Transmission Electron Microscopy (HAADF STEM) coupled with Energy Dispersive X-ray spectroscopy (EDX) provides insights into detailed atomic and elemental structures of the nanoparticles. In situ heating and liquid electrochemical TEM techniques are powerful tools in order to describe phenomena observed ex situ in more detail and time resolved which allows valuable conclusions to be drawn.

3.3.1 Theoretical Aspects

The smallest distance a human eye can resolve is about 0.1 to 0.2 mm. An ordinary light microscope, operating in the visible light range between 400 to 700 nm, is suitable to study specimens like a human hair, which has dimension between 50 and 100 µm. In principle, transmission electron microscopes (TEMs) operate in the same way like common light microscopes but instead of using visible light they use electrons. The wave-particle dualism of electrons (Louis de Broglie, 1925) is of fundamental importance for electron microscopy as the wave properties of electrons are essential. According to Rayleigh, the smallest distance (δ) a microscope can resolve is given by the wavelength (λ), refractive index (μ), and the semi-angle of collection of the magnification lenses (β).

$$\delta = \frac{0.61\,\lambda}{\mu\,sin\,\beta} \qquad \text{Eq. 6}$$

According to Eq. 6, radiation with a smaller wavelength allows the resolution of smaller distances in the investigated material and, thus, higher magnification can be reached. De Broglie also introduced the dependence of the resulting wavelength on the energy (E) of the electron.

$$\lambda = \frac{1.22}{E^{1/2}} \qquad \text{Eq. 7}$$

As a result of the simplified Eq. 7, electrons with large energies have small wavelength and, therefore, allow the resolution of smaller objects.

$$\lambda = \frac{h}{(2m_0 eV)^{1/2}} \qquad \text{Eq. 8}$$

Eq. 8 describes the resulting wavelength (λ) of an applied acceleration voltage (V), using Planck's constant (h), the electron mass (m_0) and the elementary charge of an electron (e).

By increasing the acceleration voltage, the wavelength of electrons decreases. TEMs currently operate mostly at 200 to 400 kV and offer high magnifications and resolutions due to major breakthroughs in spherical- and chromatic aberration corrections[111].

1932, Knoll and Ruska reported the first concept for an electron microscope, which was awarded with the Noble Prize for Physics in 1986. Since then, electron microscopy was used extensively in several different manners, such as transmission electron microscopes (TEM) or scanning transmission electron microscopes (STEM) among several others.

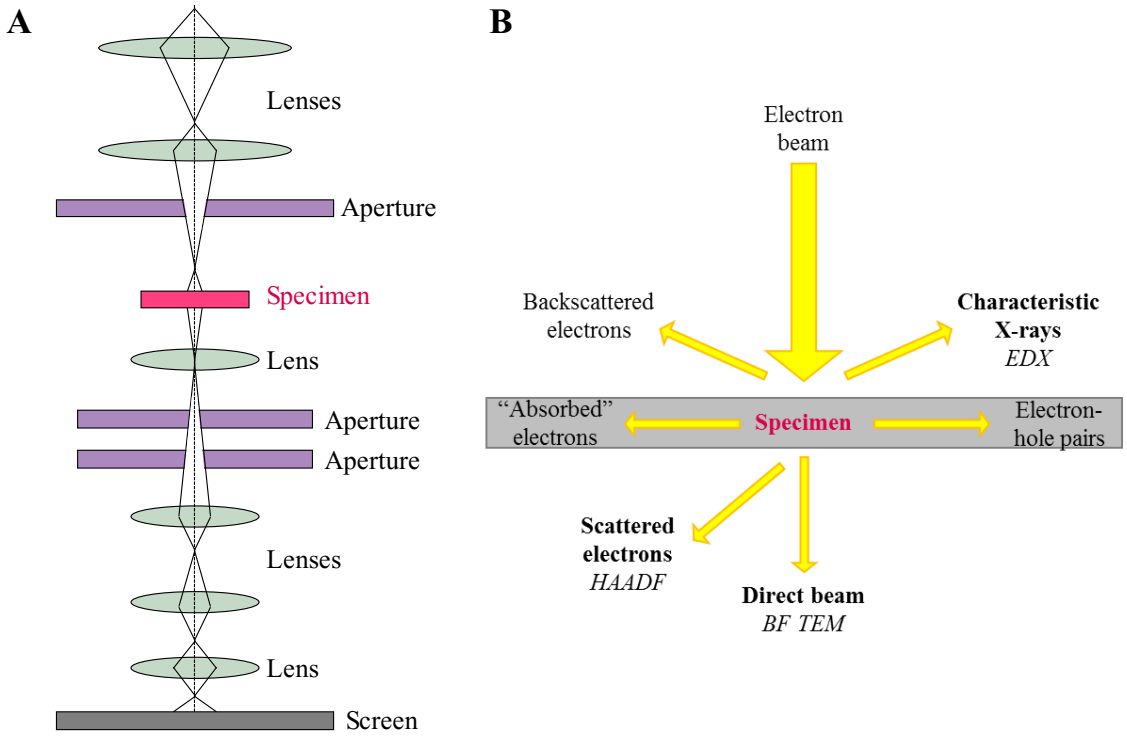

Figure 3.4 A) Schematic illustration of a transmission electron microscope column illustrating the different lenses, apertures and the beam pathway. **B)** Interaction of an electron beam with a thin species and the possibly resulting signals, which can mostly be detected with a TEM.

Figure 3.4A schematically illustrates the general design of a TEM column. The electrons are emitted from an electron gun in the very top of the column, travelling a pathway through a set of electromagnetic condenser lenses and the condenser aperture before reaching the specimen. Behind the sample, the objective aperture, intermediate lenses and projector lenses can be tuned in order to choose between imaging or diffraction mode, to focus the resulting image focus or and to change the contrast. The lenses double in function as electromagnetic lenses that can adjust the electron beam. When the electrons interact with a specimen several processes can take place and, therefore, different signals can be detected in an electron microscope (Figure 3.4B)[111].

The direct beam (transmitted beam) is used to create a bright field (BF) image in TEM. The electron beam is transmitted through a thin specimen (<100 nm thick) and an image is formed by the interaction of electrons with

the specimen. The resulting image is visible using a fluorescent screen or a CCD (charge-coupled device) sensor connected to a computer software. In BF, the images of thicker objects or objects with a higher atomic number appear darker than thinner or lighter objects because they transmit the incident beam weaker and allow less intensity to reach the detector.

Besides the direct/transmitted beam, scattered electrons are often used to create a dark field (DF) image. This is achieved by placing an aperture that blocks the main beam and allows only scattered electrons to pass. A high angle annular dark field (HAADF) detector is used which collects the signal from the scattered electrons in an annulus around the center beam at a very high angle. This has for the advantage of a higher signal collection efficiency than in the direct beam, providing more detailed information about the specimen. In HAADF microscopy, the imaged objects appear brighter in comparison to the background, because the electrons scattered by the object are directly detected. Furthermore, HAADF images allow for Z contrast images, as scattering is highly sensitive to the atomic number of the atoms.

In STEM the electron beam is focused to a fine spot which allows to investigate the specimen point by point in a raster. The combination of STEM with EDX spectroscopy or electron energy loss spectroscopy (EELS) and HAADF imaging (HAADF STEM) allows the analysis in terms of elemental distribution of the investigated objects.

EDX spectroscopy is used for elemental analysis of a specimen. The high-energy electron beam interacts with the atoms of the sample and excites electrons from discrete electron shells in-turn leaving an electron hole, which is subsequently refilled by an electron from a higher energy shell. The energy difference in the shells is released in the form of X-rays. The X-ray radiation is characteristic for the chemical elements present in the sample. By collecting the energy and intensity of the radiation with a X-ray detector, the chemical composition can be determined[111]. In combination with the scanning procedure of the STEM elemental mappings are obtained (STEM EDX).

In Situ Electron Microscopy

In situ electron microscopy is a powerful technique to combine temporal and spatial resolution of processes occurring on or in the investigated specimens in their chosen native environment. In contrast to ordinary *ex situ* TEM investigations, the exact same sample position or particle agglomerate can be investigated over a certain time period. Identical locations (IL) also offers this opportunity when using specialized numbered IL TEM grids however the specimen needs to be dried or cooled down to room temperature and transferred from its native environment to the vacuum in the microscopy column. The possibilities of *in situ* TEM methods comprise a large range of applications and are frequently improved and optimized by several suppliers.

In situ Heating Transmission Electron Microscopy

Temperature is one of the most important parameters influencing materials in terms of their main characteristics such as shape, size, composition, porosity alloy condition among others. *In situ* heating electron microscopy allows tracking of changes of the specimen structure in detail as a function of temperature during heating and subsequent cooling. These studies are typically conducted under high vacuum in the microscope column *via* external electric heating through the heating holder, however some approaches also allow the investigation in different gas atmospheres[112].

In situ Liquid Electrochemistry Microscopy

Observing the processes taking place at a liquid/solid interface is necessary in order to understand and improve materials, especially in the field of electro-catalysis. Early attempts to study liquids in TEM mostly addressed hydrated samples such as life science materials. The concept of investigating liquid samples in the microscope is not a recently founded idea. Figure 3.5 gives a brief overview about historic progress made in terms of electron microscopy and the temporal classification of *in situ* TEM methods.

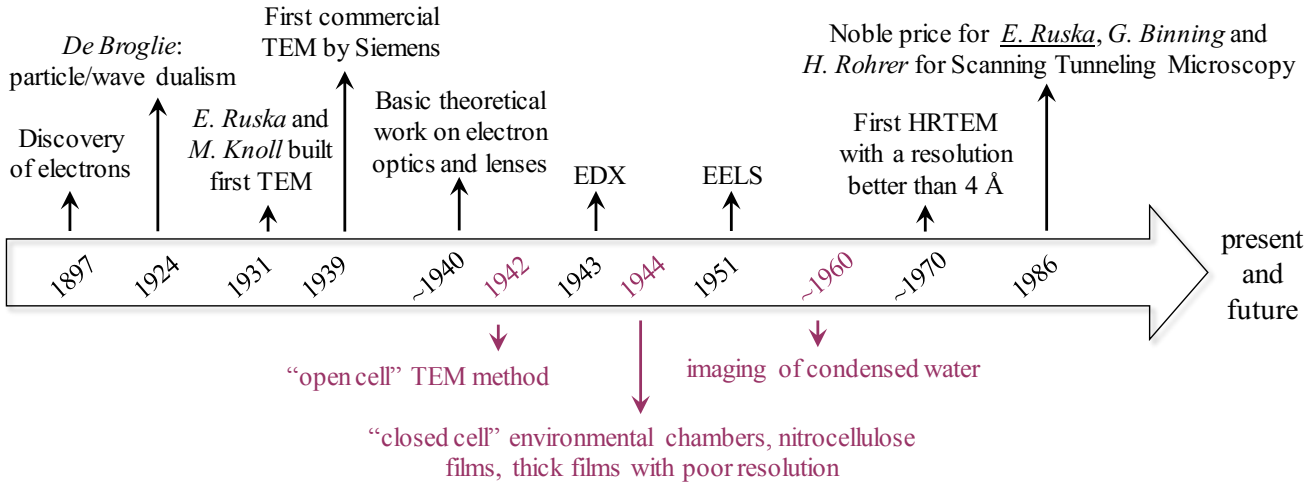

Figure 3.5 Brief historic overview of achievements in TEM and the chronological integration of *in situ* liquid TEM (purple) below the time axis arrow[113].

The first liquid TEM approach was described in 1942 as the "open cell" method. Differential pumping was used to control the pressure at the sample region, which enables imaging in ambient air at up to 0.3 bar. Some years later, the first "closed cell" approach was reported. For this, thin nitrocellulose films were used which were still very thick and provided only poor resolution. In the early 1960s, water was imaged for the first time which was achieved by using an environmental chamber consisting of two thin foils only separated by a few micrometers. Modern microfabrication methods offer the opportunity to equip liquid cells with electrodes and heating functionalities which drastically widened the possibilities in *in situ* liquid TEM imaging[111,113].

Despite the great enhancement of equipment and methods for *in situ* liquid electron microscopy, the possibilities are still limited in their current applications Due to multiple scattering of electrons in the liquid and window layer, a suitable liquid film thickness is of fundamental importance in order to obtain good image contrasts. Figure 3.6A gives an example of a liquid film, covering an agglomerate of Pt nanoparticles supported on carbon. Another significant problem is the interaction of the electron beam with the aqueous media. The radiolysis of water, induced by the electron beam, leads to the formation of hydrogen gas bubbles (see Figure 3.6B), the formation of protons changes the pH and the formation of hydrated electrons which might alter the sample.

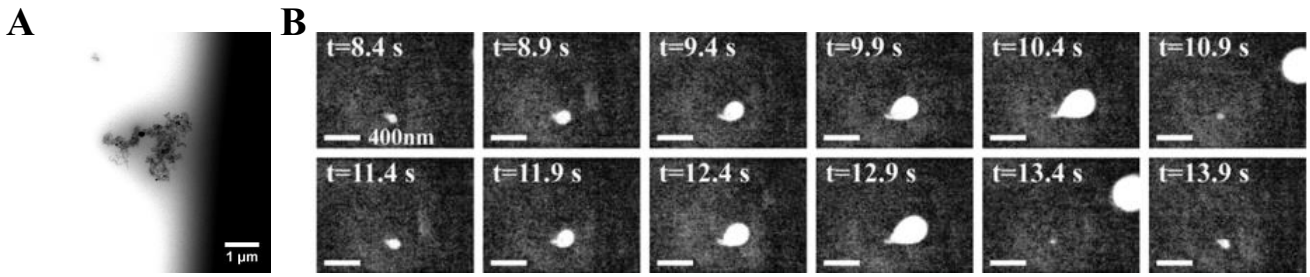

Figure 3.6 Limitations and challenges of *in situ* liquid TEM. **A)** Blurring of the image quality due to thick liquid films covering a particle agglomerate of carbon supported Pt nanoparticles. **B)** Bubble formation in aqueous solution while imaging gold nanorods at pH ~7 due to beam induced radiolysis of water (Figure B reproduced from Ref. [114] with permission from American Chemical Society).

As a consequence of the limitations mentioned above, these investigations require low beam doses in combination with highly sensitive detectors in order to minimize beam induced changes of the sample or "beam damage".

3.3.2 Experimental Procedure

Ex situ transmission electron microscopy (TEM) was performed on a FEI Tecnai G^2 20 S-TWIN with LaB_6-cathode, with 200 kV accelerating voltage and a resolution limit of 0.24 nm. Powder samples were dispersed on a lacey carbon film on a 200 mesh Cu grid.

Scanning transmission electron microscopy (STEM) was performed on a FEI Titan 80-200 (“ChemiSTEM”) electron microscope with a C_s-probe corrector (CEOS GmbH) and a high-angle annular dark field (HAADF) detector[115] at 200 kV accelerating voltage. In order to achieve “Z-Contrast” conditions, a probe semi-angle of 25 mrad and an inner collection semi-angle of the detector of 88 mrad were used. Compositional maps were obtained with EDX using four large-solid-angle symmetrical Si drift detectors. For EDX elemental mapping, Pt L, Ni K and Rh L peaks were used. The margin of error for the EDX composition measurement was estimated to be +/- 2 at.% and a minimum of 20 particles were investigated.

In situ heating TEM was performed using a Protochips Aduro heating holder (Figure 3.7) in a FEI T12 Spirit TEM with a LaB_6 filament and 120kV accelerating voltage. The sample powder was dispersed in iPrOH and dropped on a model E-AHA21 Protochips E-chip, with an amorphous carbon film covering the electron transparent window.

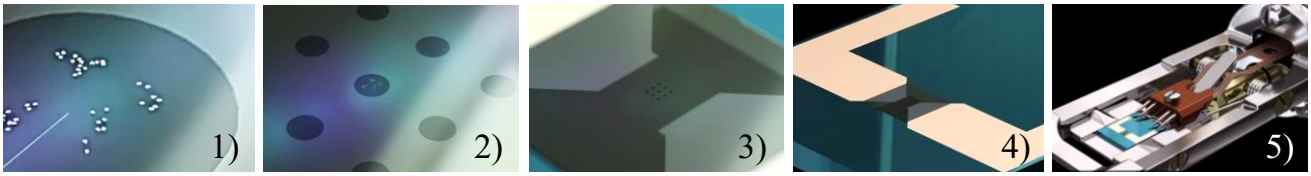

Figure 3.7 Schematic illustration of a heating chip used for *in situ* heating electron microscopy. **1)** Dispersed sample was dropped on the Protochips Chip, **2)** less magnified view of the amorphous silicon nitride window with integrated circuits, the electron transparent windows. **3)** and **4)** less magnified images of the chip which is placed in the heating TEM holder **5)**. Images adapted from reference [116] with permission from Protochips.

For *in situ* liquid electrochemical TEM investigations, a Protochips Poseidon electrochemical cell holder was used (Figure 3.8). The liquid flow cell portion[117,118] and the electrochemical cell design[83] has been discussed previously. The Pt-Ni catalyst nanoparticles were dispersed in isopropanol and drop casted onto the chips with electrodes, which were cleaned prior to use[117]. As a matter of fact, the Pt-Ni catalyst was not only dispensed on the carbon WE, as well as the platinum RE and CE. Due to the RE and CE being composed of platinum and large in size compared to the dispersed nanoparticles, the particles should not affect electrode behavior.

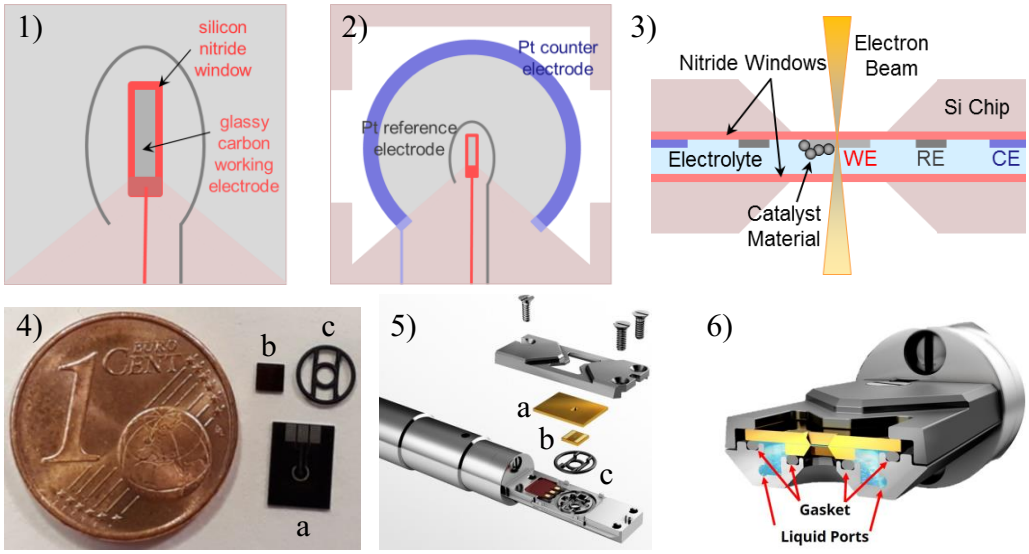

Figure 3.8 Chip design and set up for the *in situ* electrochemical TEM investigation. **1)** Top view of the electrochemical liquid cell chip. The catalysts dispersion is dropped on the glassy carbon working electrode, **2)** less magnified top view of the electrochemical TEM chip showing the glassy carbon working electrode in the center, surrounded by the Pt reference electrode (gray) and the Pt counter electrode (blue). **3)** Side view of the chip with the corresponding bottom chip and the electrolyte layer between the chips. **4)** Dimension of the electrochemistry chip (a), the bottom chip (b) and the gasket (c) in comparison to 1 euro cent. **5)** Assembling in the tip of the TEM holder. **6)** Cross section of the assembled chips with the corresponding liquid flow. Images 5) and 6) are adopted from "Workflow & Training Poseidon Select Version 1.2; Copyright 2017, Protochips, Inc." with permission from Protochips.

Initially, a solution of 0.1 M $HClO_4$ / H_2O (diluted from 70 % conc. $HClO_4$, 99.999 % trace metal bases, Sigma Aldrich with milli-Q water) was flowed into the cell at 300 µL h^{-1} to wet it, and then flowed at 50 µL h^{-1} during the experiment using a syringe pump (Infuse/Withdraw Pump 11 Pico Plus Elite, Harvard Apparatus). The liquid flow refreshes the solution over the course of the several-hour experiment but is sufficiently slow to not to

significantly alter the electrochemistry. The electrolyte layer thickness was 300 nm, estimated by electron energy loss spectroscopy[117]. A "floating-type" Gamry potentiostat was used for the *in situ* TEM measurements. The platinum reference electrode was calibrated in 0.1 M perchloric acid using the well-known characteristics of the hydrogen underpotential deposition region of platinum-based materials. With that, 0.0 V_{RHE} was correlated to -0.8 V_{Pt}. All potentials are reported against the reversible hydrogen electrode (RHE) based on this calibration to allow better comparability to other studies.

In situ microscopy was performed using a monochromated FEI Tecnai F-20 STEM/TEM operated at 200 kV and equipped with a Gatan 865 HR-GIF spectrometer for EELS analysis. Electron beam conditions were selected to optimize imaging conditions while minimizing beam damage, ranging from 30 – 60 $e^- nm^{-2}s^{-1}$ for HAADF-STEM imaging with a 9.6 mrad convergence angle. During control experiments with no electrochemical biasing, we observed that a beam dose of 110 $e^- nm^{-2}s^{-1}$ induced damage while a dose around 60 $e^- nm^{-2}s^{-1}$ did not show significant changes after 10 minutes of imaging. The dose reported is the averaged dose rate over the entire field of view: the probe current was varied between 2.6 and 4.9 pA using the monochromator while maintaining the 9.6 mrad angle. The 4.9 pA probe current was used at lower magnifications with a field of view of 1.01 microns, and the 2.6 pA probe current was used during imaging with a field of view of 517 nm. The number of pixels across all datasets was 512 and the dwell time was 12 µs. For the collected movies a denoising protocol of ImageJ was run to enhance signal to noise[119-121].

Corresponding *ex situ* imaging was performed using a monochromated FEI Titan Themis CryoS/TEM operated at 300 kV, with a 21.4 mrad convergence angle.

3.4 Electrochemical *in situ* Fourier-transform Infra-red Spectroscopy (FTIR)

In this work, Fourier-Transform Infra-red Spectroscopy (FTIR) was used to study the CO band shift under potential control as a function of different Pt-Ni alloy surface. Thereby, very fine and specific surface changes were determined and used to explain ORR performance differences.

3.4.1 Theoretical Aspects

In Infra-red (IR) spectroscopy, a sample is irradiated with infra-red radiation which is usually divided into near-IR (14,000-4,000 cm^{-1}), mid-IR (4,000-400 cm^{-1}) and far-IR (100-10 cm^{-1}) corresponding to wavelengths between 1 mm and 780 nm. The exciting of electromagnetic radiation is absorbed by the sample, causing vibrations in the molecule of the sample when reaching specific energies[122].

FTIR spectrometers are mostly equipped with Michelson-Interferometers because of their time-efficiency in collecting IR spectra, which allows recording of a large quantity of spectra on a suitable lab-time-scale. An interferogram showing the intensity as a function of the mirror position (moving mirror of the Michelson-Interferometer) can be translated to a wavenumber or wavelength dependent spectrum using sophisticated software performing Fourier transformation.

The most common way to study liquids and gasses is to irradiate them and detect the beam passing through the media. This method however is only suitable for transparent or semi-transparent materials. When investigating solids, the attenuated total reflectance (ATR) technique is utilized. In ATR, infra-red light passes through the ATR crystal, forcing total reflection on the sample and forming an evanescent wave interacting with it (Figure 3.9). The penetration depth (d_p) is given by the wavelength, the incidence angle (θ) and the refractive indices of the crystal and the sample medium. A detector then collects the exiting beam[122].

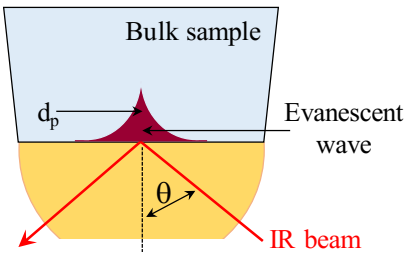

Figure 3.9 Geometry of attenuated total reflection (ATR) IR spectroscopy. The evanescent wave with a certain penetration depth interacts with the bulk sample medium.

ATR is often used to study the surface of the investigated bulk material. Due to the limited penetration depth of a few micrometers, strong overlapping with the surrounding medium of the sample, like air or water (electrolyte), is minimized[123]. When vibrations in the excited molecules cause a change in dipole moment, the investigated sample is IR-active.

Adsorbed CO is widely used to study heterogeneous catalysts and electrocatalysts, because it is an IR active probe molecule, representing e.g. oxygen species or other intermediates on a catalyst surface. The interaction between the CO molecule and the metal particles elucidate the characteristics of the catalytic surface. The adsorption of CO onto a metal surface can be generally described by the Blyholder model, suggesting an electron donation of the CO molecule through a σ bound to the metal orbitals and a back-donation from the metal into the empty 2π* orbitals of CO (see Figure 3.10A). The position of the CO band is influenced by the geometry of the adsorption (see Figure 3.10B), the adsorption site (terrace/edges/corners), the surface coverage causing dipole-dipole interactions, the interaction of CO with surrounding molecules and the strength of the back donation from the metal[124]. Due to the interaction between CO and the metal, the internal bond strength of the CO molecule decreases, leading to an IR band shift to lower wave numbers as compared to CO in gas phase, which is described in Figure 3.10C. A stronger binding to the metal surface causes a weaker internal bond strength of the CO molecule. Consequently, less energy, hence larger wavelength or smaller wavenumbers are needed to cause a vibration.

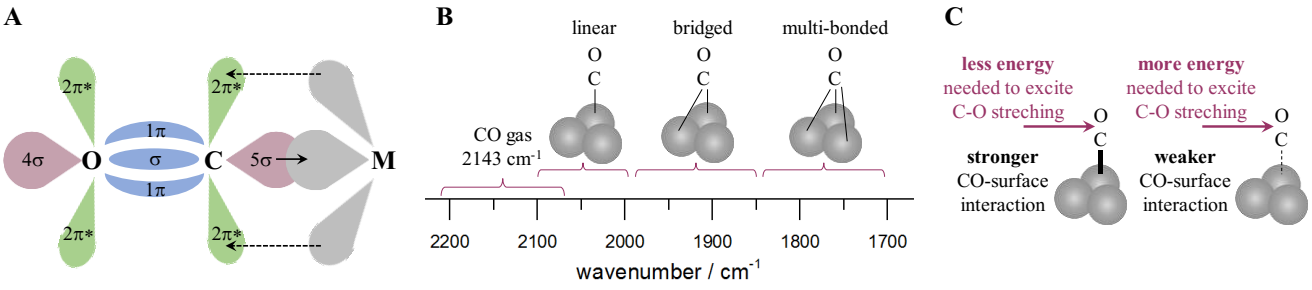

Figure 3.10 General model of possibilities of CO interaction with a metal surface. **A)** Interaction between the CO orbitals and the metal orbitals of adsorbed CO onto a metal surface. **B)** Position of CO band in different adsorption geometries. **C)** Relation between bonding strength and exciting radiation[124].

When investigating CO vibrations on different electrocatalyst surfaces in their operating environment, one of the major challenges is the aqueous media in which these reactions take place. Water usually is an improper medium for IR investigations as it is a strong IR absorber itself. With taking certain care on subtracting the water bands, CO bands become clear to investigate. Still, the presence of water influences the position of the CO band. For instance, for Pt/Al_2O_3 a red shift of around 37 cm^{-1} was observed when CO was adsorbed from a CO saturated solution in comparison to when it was adsorbed from the gas phase. Further, the signal intensity in water significantly decreased. Also, the degree of coverage of CO on the particle surface influences the position of the CO band. Higher wavenumbers were observed with higher coverage due to dipole-dipole interactions. For electrochemical investigations, it is important to consider, that a change in potential causes a change in peak position. As a result, special care has to be taken when comparing CO vibrations on a catalyst surface. Under potential control during electrochemical investigations CO presents an excellent probe molecule to investigate and compare surface binding strength to different catalyst surfaces and to draw important conclusions regarding their electrocatalytic activity[124].

3.4.2 Experimental Procedure

(ATR) FTIR spectroscopy was conducted in an ATR-FTIR setup which allows for the investigation of supported nanoparticle ink films[125]. For the ink solution, 0.5 mL milli-Q water and 0.5 mL isopropanol were mixed with 1.0 mg catalyst powder using a probe-sonifier. The ink solution was deposited directly onto the ATR prism, a ZnSe hemisphere. Figure 3.11 displays the schematic setup of the used electrochemical cell with the IR-prism as the bottom of the cell.

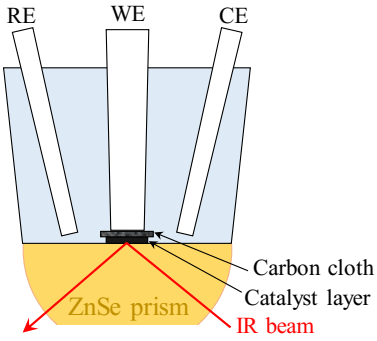

Figure 3.11 Schematic illustration of the FTIR liquid electrochemical cell. The bottom if the electrochemical cell is the ATR crystal on which the catalyst is directly deposited. To allow electrochemical contact and mass transfer, a carbon cloth is placed on top of the catalyst layer before pressing the working electrode (WE) against it.

The electrochemical connection was ensured *via* a carbon cloth (Toray Paper 030) that provides a reservoir of electrolyte over the catalyst, minimizing mass transport limitations and polarization effects, and a Pine glassy carbon rod fixing the carbon cloth (

Figure **3.11**). The spectra were collected in a custom-made glass cell with a Bruker Vertex 70v FTIR spectrometer equipped with a Mecury-Cadmium-Tellurid (MCT) detector cooled with liquid nitrogen. As CE, a platinum mesh was used and as RE a RHE fabricated by purging H_2 over a Pt-mesh. All *in situ* electrochemical measurements were controlled with a Metrohm Autolab PGSTAT204 potentiostat. An unpolarized beam was focused with a Pine Veemax II onto the sample spot of the cell. Each spectrum resulted from 100 to 107 interferograms, which were collected and averaged, with a spectral resolution 4 cm^{-1}. Spectra are given in reflectivity units defined as $R/\Delta R = RE_2\text{-}RE_1/RE_1$ with two single beam spectra R at applied potentials E_1 and E_2. Here, the reference spectrum RE_1 was collected in the same electrolyte (0.1 M $HClO_4$) immediately before the investigated potential scan at the respective start potential.

The complete beam pathway was under vacuum more than 24 hours prior to each measurement. The positions of the bands were determined by taking the band maximum, or, for bipolar bands, by taking the mean value of the maximum and the minimum. Reported error bars are presenting the standard deviation between at least three different and independent measurements of freshly prepared catalyst films.

3.5 Other Methods (XRD, ICP OES and DEMS) – Experimental Procedures

For this work, X-ray diffractometry (XRD) is used to determine the crystal orientation and structure of the synthesized materials, to estimate the particle composition and to check for the formation of an alloy. Inductively Coupled Plasma Optical Emission Spectrometry (ICP OES) serves to determine the elemental composition and the weight based loading of metal on the support material of the prepared catalysts. Differential Electrochemical Mass Spectrometry (DEMS) allows the detection of oxidized carbon support material by tracking the potential and current dependent CO_2 signal.

X-Ray Diffraction (XRD)

X-ray diffraction patterns were collected on a Bruker D8 Advance (Siemens KFL Cu 2K X-ray tube and Lynx Eye Detector) diffractometer in Bragg Brentano geometry using a Cu $K_\alpha 1$. The patterns were recorded between 20-80° with a step size of 0.05° and a 10 s measurement time at each step.

High temperature patterns were collected on the similar Bruker instrument with a Lynx Eye detector and Goebel-mirror. The patterns were recorded between 35-55° with a step size of 0.06° and a measurement time of 8 s at each step. The samples were heated to 180 °C in synthetic air, followed by the heat treatment in 4 % H_2/Ar. The heating and cooling rate was 10 K min^{-1} and before every X-ray measurement the temperature was held for 15 min.

Inductively Coupled Plasma Optical Emission Spectrometry (ICP OES)

To prepare the Pt-Ni-M/C for inductively coupled plasma analysis, around 5 mg of the material were dissolved in 2 mL H_2SO_2, 2 mL HNO_3 and 6 mL HCl applying a temperature of 180 °C and a pressure of 18 bar using of a microwave. After filtration to remove remaining carbon residues the samples were diluted several times to reach concentration of around 5 ppm of the respective metal. An inductively coupled plasma analysis system (ICP OES) (Varian) was used to determine the elemental composition of the synthesized particles. The selected wavelengths for the concentration determination were 203.646; 214.424; 224.552; 265.945; 306.471 nm for Pt, 216.555; 221.648; 222.295; 222.486; 227.021; 230.299; 231.604 nm for Ni and 233.477; 246.103; 249.078; 343.488; 369.236 nm for Rh.

Differential Electrochemical Mass Spectrometry (DEMS)

Differential electrochemical mass spectrometry (DEMS) were recorded using a home designed dual thin-layer electrochemical flow cell partly based the original design reported elsewhere[126]. The gas products from the flow cell was detected using a Prisma™ quadrupole mass spectrometer (QMS 200, Pfeiffer-Vacuum) with two turbomolecular pumps (HiPace 80) operating under 10^{-6} mbar. The electrolyte was separated from the chamber by a 150 µm thick hydrophobic PTFE membrane (Cat. No. PF-003HS for Cobetter® porous size 30 nm). The working electrode has an exposed area of ~ 0.193 cm^2 and pressured against a Teflon gasket to form a thin layer with defined thickness around 100µm. A Pt-mesh was used as counter electrode connected to tangential channel

to main inlet channel and real hydrogen reference electrode (RHE) to monetarize the potential. Measurements were recorded on a Biologic SP-200 potentiostat in 0.1 M $HClO_4$ (diluted from 70 % conc. $HClO_4$, 99.999 % trace metal bases, Sigma Aldrich with milli-Q water). Pt-Ni/C were homogenously dispersed by ultrasonication for 15 min, and drop-dried onto a pre-defined area ~ 0.193 cm^2 with inert Teflon film coated on glassy carbon electrodes (Φ = 10 mm in, HTW GmbH). The glassy carbon electrodes were polished with silica slurries (Buehler) of 1 μm and 0.05 μm in particle size and cleaned in acetone and milli-Q water. The electrolyte flow speed was set at the out let flow cell with a needle valve with 2μL s^{-1} and controlled during experiments with a liquid flow sensor Sensirion SLQ-QT500. Measurements done without any compensation for the ohmic resistance. The WE and Teflon gasket contact were purged with N_2 in order to avoid environment air into the reaction compartment or exchange with MS chamber. The cyclovoltammetric mass spectrometer (MSCV) curves were recorded during cycling form 0.05 V_{RHE} with most anodic potential varying from 1 V_{RHE}, 1.2 V_{RHE} and 1.4 V_{RHE} at a scan-rate of 100mV s^{-1}, with four selective channels recording m/z 44 with electrochemical measurements. To assure optimized detection of products during potential cycling as assessed with mass spectrometer, the ion source was calibrated using calibration protocol presented at Quadera software. The background stability and reproducibility was achieved by baking of vacuum chamber and mass spectrum calibration prior to experimental DEMS measurements. The ionization was preformed with electron beam at 80 eV. The amplification of the secondary electron multiplier (SEM) was setup to be around three orders of magnitude higher with regard to the Faraday detector.

4. Rh-doped Pt-Ni Octahedral Nanoparticles: Understanding the Correlation Between Elemental Distribution, ORR and Shape Stability

Accepted manuscript reproduced with permission from Nano Lett.*, **2016**, 16 (3), pp 1719–1725 (Reference* 63*).*

Parts of this work have been used in the Master Thesis of V.B. entitled "Synthese, Charakterisierung und elektrochemische Untersuchung von formselektierten Platin basierten nanoskaligen Katalysatoren" from 2015.

Vera Beermann, Martin Gocyla, Elena Willinger, Stefan Rudi, Marc Heggen, Rafal E. Dunin-Borkowski, Marc-Georg Willinger, and Peter Strasser, *Nanoletters* **2016**, 16 (3), 1719-1725, DOI: 10.1021/acs.nanolett.5b04636 (https://pubs.acs.org/doi/abs/10.1021/acs.nanolett.5b04636)

V.B. and S.R. planned and designed the experiments. V.B. performed the experiments and analyzed the data. M.G., E.W., M.H., R.E. D.-B., and M.-G.W. performed (scanning) transmission electron microscopy. V.B., M.G., M.H., S.R. and P.S. wrote the manuscript. All authors discussed the results and participated in drawing important conclusions.

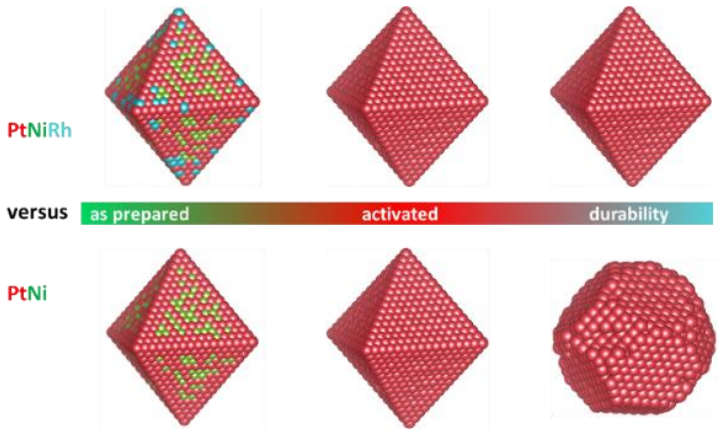

Thanks to their remarkably high activity towards ORR platinum-based octahedrally shaped nanoparticles have attracted ever increasing attention in last years. Although high activities for ORR catalysts have been attained, the practical use is still limited by their long-term stability. In this work, we present Rh-doped Pt-Ni octahedral nanoparticles with high activities up to 1.14 A mg_{Pt}^{-1} *combined with improved performance and shape stability compared to previous bimetallic Pt-Ni octahedral particles. The synthesis, the electrocatalytic performance of the particles towards ORR and atomic degradation mechanisms are investigated with a major focus on a deeper understanding of strategies to stabilize morphological particle shape and consequently their performance.*

Rh surface doped octahedral Pt-Ni particles were prepared at various Rh levels. At and above about 3 at.% the nanoparticles maintained their octahedral shape even past 30,000 potential cycles, while undoped bimetallic reference nanoparticles show a complete loss in octahedral shape already after 8,000 cycles in the same potential window. Detailed atomic insight in these observations is obtained from aberration-corrected scanning transmission electron microscopy (STEM) and energy dispersive X-ray (EDX) analysis. Our analysis shows that it is the migration of Pt surface atoms, not – as commonly thought - the dissolution of Ni that constitutes the primary origin of the octahedral shape loss for Pt-Ni nanoparticles. Using small amounts of Rh we were able to suppress the migration rate of platinum atoms and consequently suppress the octahedral shape loss of Pt-Ni nanoparticles.[63]

In this chapter, we present an investigation of newly designed near-surface *Rh*-doped *Pt-Ni* octahedral nanoparticles supported on carbon. This novel catalyst exhibits exceptional shape stability and remarkable high ORR activity and electrochemical stability compared to a *Pt-Ni* octahedral catalyst. Both catalysts were synthesized using a modified organic phase reduction method, where Rh was added at a later stage of the synthesis protocol to settle Rh mainly on the surface[48,52,127]. To the best of our knowledge we are first, who show, that Rh has a beneficial influence on electrochemical and octahedral shape stability of bi- or trimetallic *Pt-Ni* nanocatalysts, which represents a new class of stable octahedral shaped *Pt-Rh-Ni* nanoparticles during the electrochemical treatment for the ORR.

4.1 Results

Platinum-rhodium-nickel particles with 3 at.% Rh have been synthesized using a solvothermal method with oleylamine and oleic acid as solvents and tungsten hexacarbonyl as reducing and shape directing agent, followed by an acetic acid treatment to purify the particle surface and adjust the noble-metal-to-nickel ratio. The same method was used to synthesize bimetallic *Pt-Ni* octahedral particles, which supposed to serve as a comparison and reference.

The elemental composition and the Pt-based weight loadings on the carbon support vulcan XC 72R were determined by the use of ICP OES. After acetic treatment (*initial*) the compositions were $Pt_{81}Ni_{19}$ and $Pt_{71}Rh_3Ni_{26}$ and the Pt-based weight loading was 26 wt% for *Pt-Ni/C* and 24 wt% for *Pt-Rh-Ni/C,* respectively.

X-ray powder diffraction patterns for both catalysts show a single face-centered cubic structure (Figure 4.1). Compared to pure Pt reflexes, the reflexes of both samples are shifted to higher 2Θ angles due to the decreased lattice constant of the *Pt-Ni* alloy. With the incorporation of Rh there is no significant shift in the peak position due to the very small amount of Rh. The theoretical 2Θ values matches nicely the measured values (see SI, Table S1.1) using the Vegard's law.

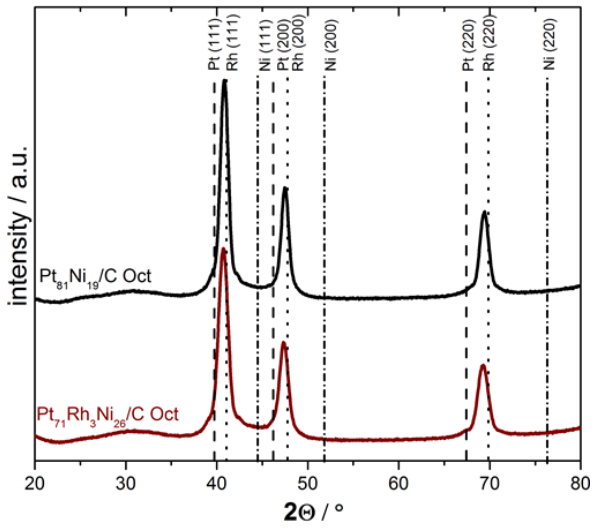

Figure 4.1 XRD profiles of $Pt_{71}Rh_3Ni_{26}$/C octahedra (red) and $Pt_{81}Ni_{19}$/C octahedra (black). Dashed, dotted and dashed-dotted lines denote pure Pt (PDF#0802), Rh (PDF#0685) and Ni (PDF#0850) face-centered cubic pattern.

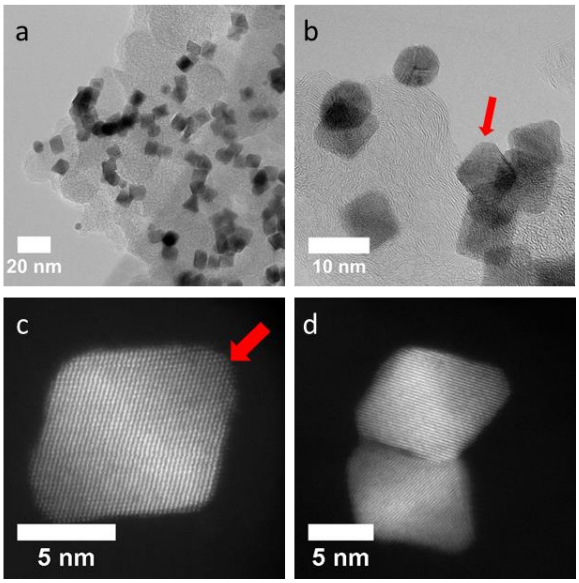

Figure 4.2 Transmission electron microscopy images of $Pt_{71}Rh_3Ni_{26}$/C after synthesis and acetic acid treatment. **a)** overview of the particles with a homogeneous distribution, **b)** most particles are octahedral with rounded corners or octahedral (red arrow) particles, **c,d)** HAADF STEM images of a truncated octahedron.

Transmission electron microscopy (TEM) and high-angle annular dark-field (HAADF) scanning transmission electron microscopy (STEM) were used to investigate the particle size and particle distribution on the carbon support. The *initial Pt-Rh-Ni* particles are well distributed on the carbon support (Figure 4.2a-d) with an average edge length of 7.4 ± 1.0 nm (see SI, Figure S1.1a,b). Most particles possess an octahedral shape with rounded corners or are truncated octahedra (red arrows) (Figure 4.2 b,c). Rounded corners likely present an energetically more stable shape than sharp edges and are therefore favored[128]. The *Pt-Ni*/C catalyst also shows homogeneously distributed octahedral shaped particles with similar edge length of 7.9 ± 1.1 nm (see SI, Figure S1.2). Due to the

fact that the particles have different crystallographic orientation with respect to the incident electron beam during TEM investigation, the true edge length will be slightly different from the one measured in projection.

The electrochemical characteristics of the *Pt-Rh-Ni/C* catalyst were determined in acidic media (0.1 M $HClO_4$) using a thin-film rotating disk electrode. Figure 4.3a shows the cyclic voltammograms of the *Pt-Rh-Ni/C* catalysts after different numbers of electrochemical cycles (cy). After activation (20 cy) the catalysts exhibit high current densities in the H_{upd} region as well as in the Pt-OH region, which are decreasing continuously with the number of cycles during electrochemical stability measurements, possibly due to the local changes on the surface of the *Pt-Rh-Ni* catalysts. These changes are most likely induced by Pt/Rh atomic migration and faceting on the surface[129]. The evaluation of the peak intensities shows a non-monotonic behavior. After *8k* (k=1000) *cycles* peaks at 0.25 and 0.4 V vs. RHE in the anodic scan exhibit the largest intensities.

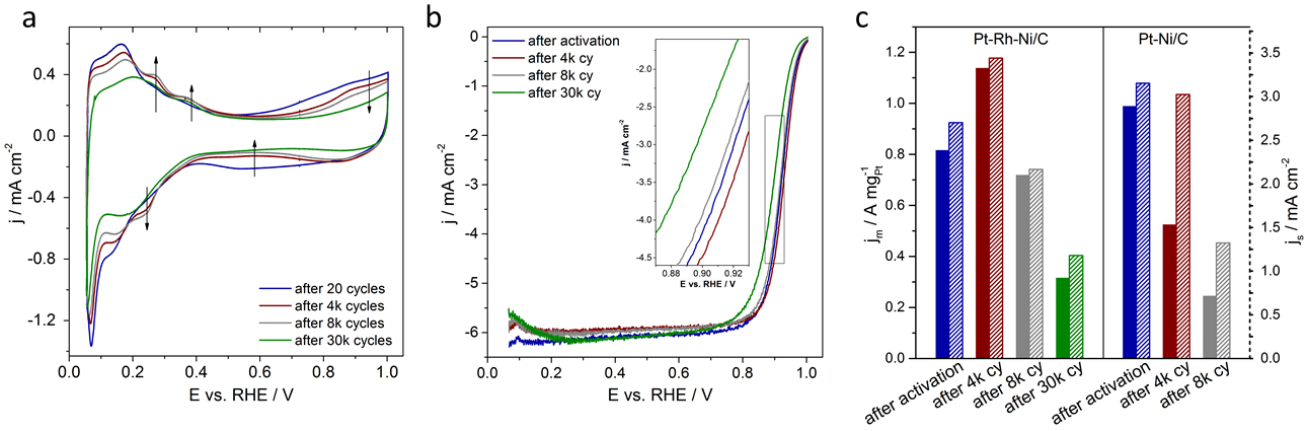

Figure 4.3 Electrochemical characterization of $Pt_{71}Rh_3Ni_{26}$/C (iR corrected): **a)** cyclovoltammograms after 20 *cycles* (cy) activation, after *4k*, *8k* and *30k cycles* (cy) stability test between 0.05 – 1.0 V vs. RHE with 100 mV s^{-1} in N_2 saturated 0.1 M $HClO_4$ electrolyte, 0 rpm (currents normalized on rotating disc electrode area 0.196 cm^2); **b)** linear sweep voltammetry after a particular number of *cycles* between 0.05 – 1.0 V vs. RHE with 10 mV s^{-1} in O_2 saturated 0.1 M $HClO_4$ electrolyte, 1600 rpm (currents normalized on rotating disc electrode area 0.196 cm^2); **c)** mass (solid bars) and specific activity (dashed bars) compared to the bimetallic $Pt_{81}Ni_{19}$/C oct (evaluated at 0.9 V).

For electrochemical activity measurements, linear sweep voltammetry was performed (Figure 4.3b). After a stability test involving a defined number of cycles the positive-going polarization curves for the ORR were recorded in O_2-saturated 0.1 M $HClO_4$ electrolyte and have been evaluated at 0.9 V vs. RHE. For *Pt-Rh-Ni/C*, the mass activity increases from 0.82 A mg_{Pt}^{-1} in activated state to an even higher value of 1.14 A mg_{Pt}^{-1} after *4k cycles* and decreases to 0.72 A mg_{Pt}^{-1} after *8k cycles*, which is a loss of only 12 % compared to the activated state, and to 0.32 A mg_{Pt}^{-1} after *30k cycles*. This behavior is surprising, as octahedral Pt-Ni based catalysts with improved mass-based and specific activity after *4k* stability cycles are not that common yet[28,47,65]. The Mo-doped Pt-Ni/C octahedral particles reported in literature indeed show significantly higher overall ORR activities after stability tests, but they exhibit a small loss in activity after 4k cycles[50]. Compared to the bimetallic *Pt-Ni/C* catalyst, the presence of Rh indeed reduces the mass-based activity after activation (0.82 vs. 0.99 A mg_{Pt}^{-1}) as mentioned before, but it exhibits a high mass-based activity after *4k cycles* (Figure 4.3c). But the *Pt-Ni/C* catalyst

shows a dramatic mass-based activity drop to 0.30 A mg_{Pt}^{-1} (70 %) after *4k cycles* and even further after *8k cycles* to 0.12 A mg_{Pt}^{-1} (88 %). The specific activity based on the electrochemical surface area (ECSA) determined by H_{upd} (see SI, Figure S1.3b,c) follows the same trend. For comparison, we synthesized particles with an even smaller Rh amount than 3 at.%, $Pt_{73}Rh_1Ni_{26}$ and $Pt_{72}Rh_2Ni_{26}$. Anyway, these amounts were too small to improve the electrochemical long-term stability, but the mass-based activities after activation were slightly higher than for the 3 at.% Rh modified catalyst (see SI, Figure S1.3a). This is in good accordance with the high activity of the bimetallic octahedral *Pt-Ni/C* after activation. Thus, we conclude that in the investigated range of Rh contents, Rh slightly reduces the ORR activity after activation, but dramatically enhances the electrochemical long-term stability. We hypothesize the existence of the optimum Rh content for high activity and stability values for Pt-Ni octahedral-shaped nanoparticles.

Comparing the cyclic voltammograms of the most active state of *Pt-Ni/C* (after 20 cycles activations) and *Pt-Rh-Ni/C* (after *4k cycles* stability test), both catalysts seem to exhibit a comparable surface structure in terms of hydrogen adsorption and desorption features in these states after electrochemical treatment (see SI, Figure S1.4). CO-oxidation experiments have been performed to get more detailed information on the surface characteristics of the *initial* and *activated Pt-Rh-Ni/C* (see SI, Figure S1.5). The early CO-oxidation peak at 0.45 V vs. RHE before and after activation indicates an oxygen donation species on the surface, which is even more pronounced after 20 cycles electrochemical activation. Hence, a Rh species on or directly below the surface can be proposed.

To understand these electrochemical observations we utilized a detailed TEM-investigation in combination with HAADF STEM and EDX to investigate the *Pt-Rh-Ni/C* catalyst after different stages of the electrochemical cycles stability test. Figure 4.4 shows the respective HAADF STEM images and EDX composition maps. The HAADF images of the *initial* catalyst, i.e. after synthesis and acid leaching, as well as the same catalyst *after 4k*, *after 8k* and *after 30k cycles* exhibit well distributed particles on the carbon support exhibiting mainly octahedral shape (Figure 4.4a, b, e, f, h, i, k,l). The retention of the octahedral shape after *8k cycles* and especially after *30k cycles* was unexpected, since the octahedral shape for the *Pt-Ni*/C catalyst disappears already after *4k* stability cycles. In fact, for Pt-rich octahedral *Pt-Ni* nanoparticles a loss in shape was reported[47,58]. Also in direct comparison with our bimetallic *Pt-Ni*/C catalyst a loss in shape, especially after *8k cycles* stability test (see SI, Figure S1.6 and Figure S1.7) could be observed, while the *Pt-Rh-Ni*/C catalyst still has an octahedral shape.

The corresponding EDX composition maps of the *Rh*-doped *Pt-Ni* particles are shown in Figure 4.4c, d, g, j, m. In the *initial* state, the EDX map of two octahedral nanoparticles oriented close to the ⟨110⟩ zone axis, indicates a Pt-rich frame, which is pointed out by a Pt-rich strip in the middle of the nanoparticles (Figure 4.4c) and an enrichment of Ni at the ⟨111⟩ facets. This elemental distribution is absolutely comparable with our previous work[47,58]. Furthermore Rh is accumulated at the surface of the particles (in Figure 4.4d highlighted by arrows and additionally shown in Figure S1.8), which is in good accordance with the results of the CO-stripping

experiment. EDX quantification yields a composition of Pt 69 at.%, Ni 25 at.%, and Rh 6 at.% of the nanoparticles imaged in Figure 4.4b and an average composition of Pt 69 at.%, Ni 26 at.%, and Rh 5 at.% of particles in the *initial* state. It should be mentioned at this point that our EDX composition analyses of the *initial* particles are corresponding very well with the results obtained by the ICP OES analysis ($Pt_{69}Rh_5Ni_{26}$ *versus* $Pt_{71}Rh_3Ni_{26}$). Thus it is reasonable to assume, that even if EDX is limited locally, the obtained compositions are right. After *4k cycles*, EDX quantification yields an average composition of Pt 74 at.%, Ni 24 at.%, and Rh 2 at.%. The composition of Pt 76 at.%, Ni 24 at.%, and Rh 0 at.% was found for the nanoparticles imaged in Figure 4.4f.

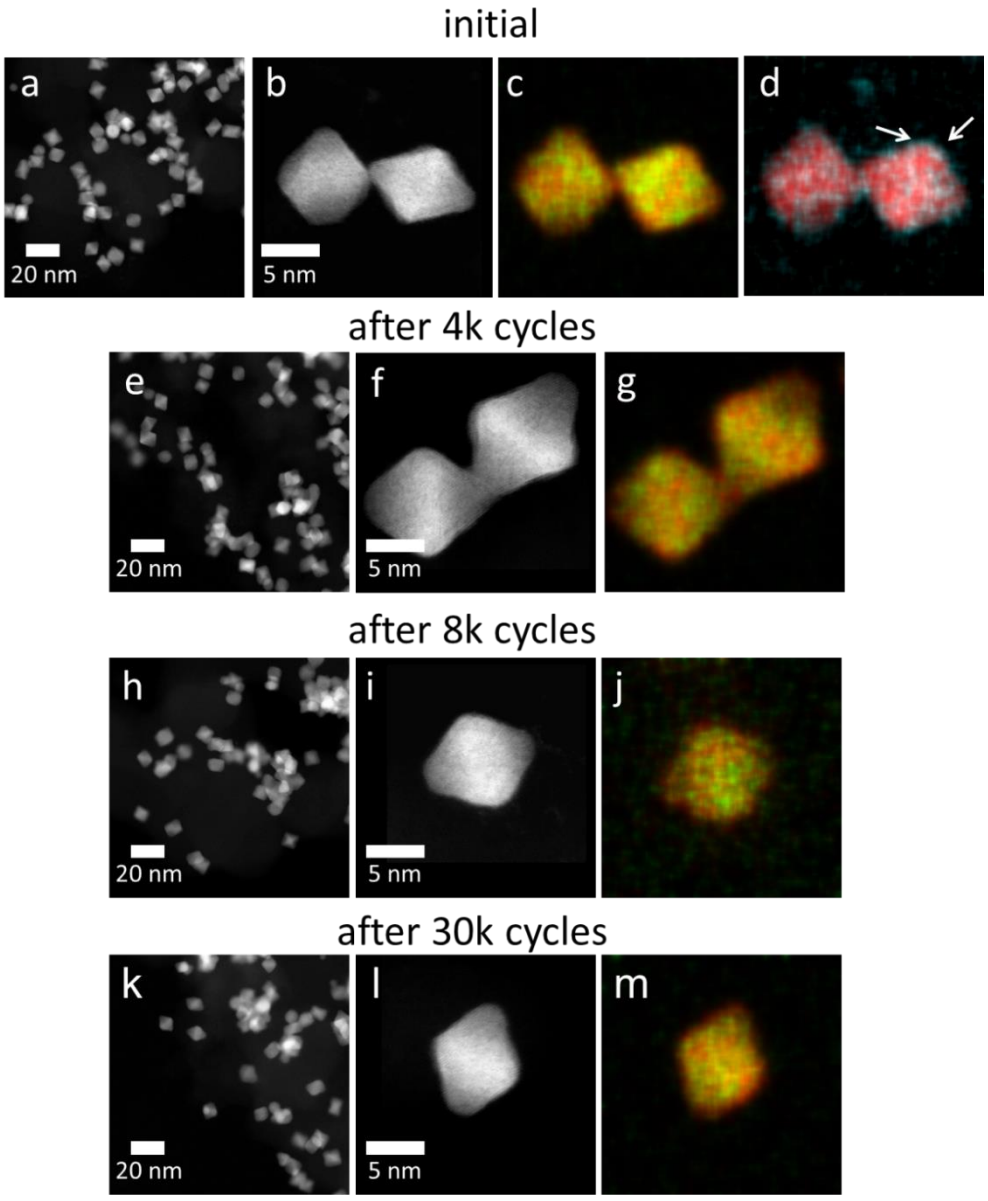

Figure 4.4 HAADF STEM images and EDX composition maps of *Pt-Rh-Ni* octahedral nanoparticles**. a), e), h), k)** Overview HAADF STEM images of the nanoparticles in the *initial* state **(a)**, after *4k cycles* **(e)**, after *8k cycles* **(h)** and after *30k cycles* **(k)**; **b), f), i), l)** High resolution HAADF STEM images of *Pt-Rh-Ni* octahedral nanoparticles oriented close to ⟨110⟩ in different states; **c), g), j), m)** Pt (red) and Ni (green) EDX composition maps and **d)** Pt (red) and Rh (blue) EDX composition map of the corresponding octahedral nanoparticles, respectively.

These results indicate that Rh is partially dissolved from the surface during the first *4k cycles*. The error of measurement of the EDX quantification was determined as +/- 2 at. %, hence the concentration of Rh is at the limit of detection by EDX. The EDX composition map in Figure 4.4g shows a similar distribution of Pt and Ni comparable to the *initial* sample, i.e. an enrichment of Ni at the facets and a Pt-rich frame. Furthermore, Pt is observed at the outermost parts of the octahedra, which, due to the projection along a <110> direction, likely caused by the presence of Pt-rich edges or the formation of a thin Pt-rich skin on the facets of the octahedra.

After 8k cycles the octahedral shape is still retained, however the typical Pt-rich strip is not visible, rather Ni seems to be distributed in the center of the octahedron as well (Figure 4.4j). This observation indicates that the segregated structure, showing a Pt frame and Ni at the facets observed in the *initial* and *4k cycled* particles, is dispersed towards a more homogeneously alloyed nanoparticle structure. The outermost parts of the octahedron are again Pt-rich. The same is true *after 30k cycles*: The particles retain an octahedral shape, the outermost parts are Pt-rich and the innermost parts are essentially homogeneously alloyed without showing significant segregation (Figure 4.4m). The average composition after *8k* and *30k cycles* is Pt 74 at.%, Ni 25 at.%, Rh 1 at.%, and Pt 74 at.%, Ni 25 at.%, Rh 1 at.%, respectively. No significant change of the composition, especially of the Ni-content, is observed after long-term cycling.

In addition to our standard electrochemical stability measurements between 0.5 and 1.0 V vs. RHE, following the DOE target[130], we also performed a series of durability measurements between 0.6 and 1.2 V vs. RHE. The EDX composition analyses are reported in the SI (see SI, Figure S1.9 and Figure S1.10) and show nanoparticles with octahedral shape even after 30 k under this condition.

In order to study the influence of Rh on the structural evolution during cycling, we investigated *Pt-Ni* octahedral nanoparticles in the *initial* state and *after 4k* and *8k cycles* (see SI, Figure S1.7). While the EDX composition map of the *initial* state as well as the *4k* state shows a similar distribution of Pt and Ni compared to the *Pt-Ni-Rh* catalyst (see SI, Figure S1.7 c, f), the octahedral shape is lost *after 8k cycles* and the particles become nearly spherical (see SI, Figure S1.7 g). The EDX map demonstrate that a Pt-rich shell is build up around the Pt-Ni alloy spherical particle (see SI, Figure S1.7 i). The average composition of the *Pt-Ni* particle in the *initial* state, after *4k*, and after *8k cycles* is Pt 79 at.%, Ni 21 at.%, Pt 78 at.%, Ni 22 at.%, and Pt 77 at.%, Ni 23 at.%, respectively.

4.2 Discussion

Hence, no significant compositional change is observed either for this catalyst. The stable Ni content during stability measurements seems contradictive to similar Pt-Ni alloy systems discussed previously[25,47]. The reason why Ni is not leached out is probably due to the fact, that the particles were treated in acetic acid after synthesis. Thereby a Pt-Rh shell was build which seems to be thick enough to protect Ni from further leaching. Rh, which

is mainly located near the surface, is rather leached out in the electrochemical treatment as its redox potential is at 0.600/0.758 V vs. RHE[131], which lies directly in the potential window of the electrochemical stability tests. It is undergoing a permanent oxidation-/reduction procedure and therefore stays close to the outermost layer of the Pt-Ni-Rh nanocatalyst. Therefore it is plausible to assume that Ni is protected by a Pt shell on the particle surface.

Based on the composition analyses, we also conclude that the loss in shape and activity of the *Pt-Ni/C* nanoparticles and the loss in activity of the *Pt-Rh-Ni/C* nanoparticles are not related to the dissolution of Ni, but rather to the segregation of Pt and Ni.

For *Pt-Ni/C* the loss in activity is obviously caused by the loss in shape, which is not true for *Pt-Rh-Ni/C*. In order to explain the decrease in activity for the *Pt-Rh-Ni/C*, we note the change in anisotropy with increasing cycles (Figure 4.4). In particular Ni segregation at the facets and Pt at the edges, have proved to be favorable for high catalytic ORR activities[47,58,66], but this distribution is not evident after 8k and especially after 30k cycles. Although high catalytic activities and durability are significantly influenced by the stability of the octahedral shape associated with the presence of active surface facets (compare to *Pt-Ni/C* after *8k cycles* in this study), the presence of a favorable surface composition (anisotropy of Ni and Pt, compare to *Pt-Rh-Ni/C* after *8k cycles*) is also necessary in order to achieve high catalytic activity. Therefore, we hypothesize that the catalytic activity loss during the durability test is mostly caused by the loss of favorable Ni segregation at the facets of octahedral shaped nanoparticles and not only by the octahedral-shaped entity.

The diffusion behavior of the Pt atoms during electrochemical potential cycling seems to be affected by the presence of Rh. Since Rh is mainly located at the surface of the particles, it seems to suppress diffusion of Pt at the edges and kinks resulting in a stable shape even after *30k* electrochemical *cycles*. Therefore a small amount of Rh on the surface seems to be sufficient to keep the octahedral shape, however, it is unable to stabilize anisotropy. A possible explanation for the ability of Rh to change the Pt segregation behavior was given by Zhang *et al.* who suggested, based on density functional theory calculations, that some transition metals M, doped on a Pt_3Ni/M (111) surface are able to promote or suppress Pt segregation to the surface[71]. Based on Pt surface segregation energies, Rh, in comparison to Ni, exhibits more positive values suggesting suppressing Pt segregation rather than Ni. More broadly, our study suggest, that Rh doped Pt alloy surfaces can be a general strategy to stabilize octahedral nanoparticle surfaces.

4.3 Conclusion

In conclusion, we design and present a synthetic pathway for near-surface *Rh*-doped *Pt-Ni* catalysts with well-defined shapes using a solvothermal method. The resulting *Pt-Rh-Ni* particles were tested for the electrochemical ORR and exhibit an exceptional and improved activity and stability behavior. Compared to a bimetallic *Pt-Ni/C* catalyst, the activity after *4k cycles* electrochemical stability test is improved and the octahedral shape remained nearly unaffected even after *30k cycles*. In contrary, the reference *Pt-Ni* octahedral particles lost around 70 % of their *initial* activity already after *4k cycles* and completely lose their shape after *8k cycles*. These observations are explained by detailed microstructural investigations of the atomic rearrangement processes on the surfaces of the two catalysts. It was found, that the shape losses occur mainly due to the Pt atom diffusion during dynamic potential cycling and Rh suppresses the diffusion of Pt atoms. Therefore small amounts of Rh prevent a loss in shape and maintain active surface structures and particles shape during and after the electrochemical treatment. In conclusion, these results could serve as a guideline for a new class of active and stable shaped electrocatalysts.

5. Tuning the Electrocatalytic Oxygen Reduction Reaction Activity and Stability of Shape-Controlled Pt-Ni Nanoparticles by Thermal Annealing - Elucidating the Surface Atomic Structural and Compositional Changes

Accepted manuscript reproduced with permission from J. Am. Chem. Soc., ***2017**, 139 (46), pp 16536–16547 (Reference* 132). *Copyright 2017 American Chemical Society.*

Vera Beermann, Martin Gocyla, Stefanie Kühl, Elliot Padgett, Henrike Schmies, Mikaela Goerlin, Nina Erini, Meital Shviro, Marc Heggen, Rafal E. Dunin-Borkowski, David A. Muller, and Peter Strasser, *JACS* **2017**, 139 (46), 16536–16547, DOI: 10.1021/jacs.7b06846 (https://pubs.acs.org/doi/10.1021/jacs.7b06846)

V.B. planned, designed and performed octahedral nanoparticle synthesis, electrochemical characterization, FTIR, XRD and *in situ* heating TEM measurements and analyzed the data. Mi.G. and H.S. planned and performed the synthesis of the mono-metallic reference materials. Ma.G., M.S. and M.H. planned, performed analyzed STEM-EDX measurements. N.E. designed the FTIR experiment and participated in analyzing the data. S.K. performed *ex situ* TEM measurements and Rietveld analysis. E.P. participated helped performing the *in situ* heating TEM measurements. All authors participated in analyzing the data, discussing the results, and writing the manuscript.

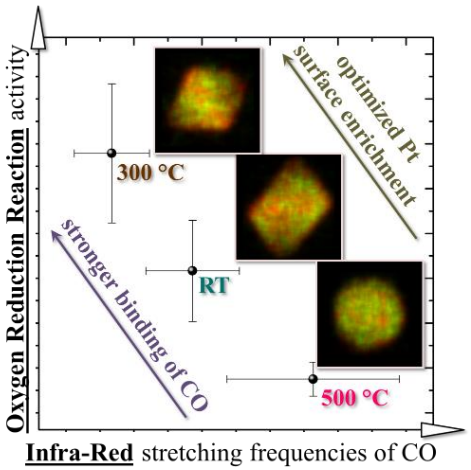

Shape-controlled octahedral Pt-Ni alloy nanoparticles exhibit remarkably high activities for the electroreduction of molecular oxygen (ORR), which makes them fuel cell cathode catalysts with exceptional potential. To unfold their full and optimized catalytic activity and stability, however, the nano-octahedra require post-synthesis thermal treatments, which alter the surface atomic structure and composition of the crystal facets. Here, we address and strive to elucidate the underlying surface chemical processes using a combination of ex situ analytical techniques with in situ transmission electron microscopy (TEM), in situ X-ray *diffraction (XRD),*

and in situ electrochemical Fourier transformed infra-red (FTIR) experiments. We present a robust fundamental correlation between annealing temperature and catalytic activity, where a ~25x higher ORR activity than commercial Pt/C (2.7 A mg_{Pt}^{-1} at 0.9 V_{RHE}) was reproducibly observed at annealing at 300 °C. The electrochemical stability, however, peaked without any and at the most severe heat treatments at 500 °C. Aberration-corrected scanning transmission electron microscopy (STEM) and energy dispersive spectroscopy (EDX) in combination with in situ electrochemical CO stripping/FTIR data revealed subtle, but important differences in the formation and chemical nature of Pt rich and Ni rich surface domains in the octahedral (111) facets. Estimating trends in surface chemisorption energies from in situ electrochemical CO/FTIR investigations suggested that balanced annealing generates an optimal degree of Pt surface enrichment, while the others exhibited mostly Ni rich facets. The insights from our study are quite generally valid and aid in developing suitable post synthesis thermal treatments for other alloy nanocatalysts as well.[132]

To get molecular insight how post-synthesis treatments affect the catalytic performance of octahedral PtNi nanocatalysts and help unfold unprecedented Pt mass based activities for the ORR, we investigate here the correlation of thermal annealing and their surface structure, composition and ORR activity and stability. What sets this study apart from previous such studies is our focus on shape-controlled PtNi nanoparticles and their unprecedented high catalytic activity and the combined use of a variety of *ex situ* and *in situ* techniques that allow conclusions as to the composition of the topmost layers of the octahedra.

First, we present studies on the particle behavior in terms of shape, distribution on the carbon support and alloy conditions during heat treatment both *ex situ* and *in situ* by utilizing X-ray diffraction (XRD) and transmission electron microscopy (TEM). Second, we present electrochemical characterization of the Pt-Ni nanoparticles tested for the ORR, paying attention not only to their initial activity but also to their stability. The resulting activities and stabilities are correlated to the nanoparticle shape and size evolution, elemental bulk distribution and detailed surface characteristics using CO oxidation, aberration-corrected scanning transmission electron microscopy (STEM) in combination with energy dispersive X-ray (EDX) analysis and *in situ* electrochemical Fourier transform infra-red (FTIR) spectroscopy. Together, we provide a consistent picture of the surface chemical modification and conditions that lead to a cathode catalyst Pt mass activity exceeding that of commercial Pt by a factor of ~25.

5.1 Results

Synthesis. Shape-controlled Pt-Ni nanoparticles were synthesized using a wet-chemical approach including oleic acid and oleylamine as surfactants and solvents, after which the supported nanoparticles were exposed to different post-synthesis treatments: washing with ethanol after synthesis (*PtNi_raw*), washing and annealing at an upper temperature of 300 °C (*PtNi_300*) and washing and annealing at an upper temperature of 500 °C

(*PtNi_500*) (Figure 5.1a). The particles were annealed at 180 °C in synthetic air in order to oxidize remaining organic surfactants from the synthesis and subsequently treated at elevated temperatures in reducing atmosphere for the purpose of ensuring a metallic surface. PtNi_raw should serve as an un-annealed reference and has experienced no thermal treatment. Details on that annealing procedure can be found in the experimental part and in Figure 5.1a. All three catalysts exhibit a composition between $Pt_{34}Ni_{66}$ and $Pt_{33}Ni_{67}$ and a Pt-based mass loading on Vulcan of around 15-16 $wt\%_{Pt}$, measured by ICP OES. The compositions are presented in Figure 5.1a.

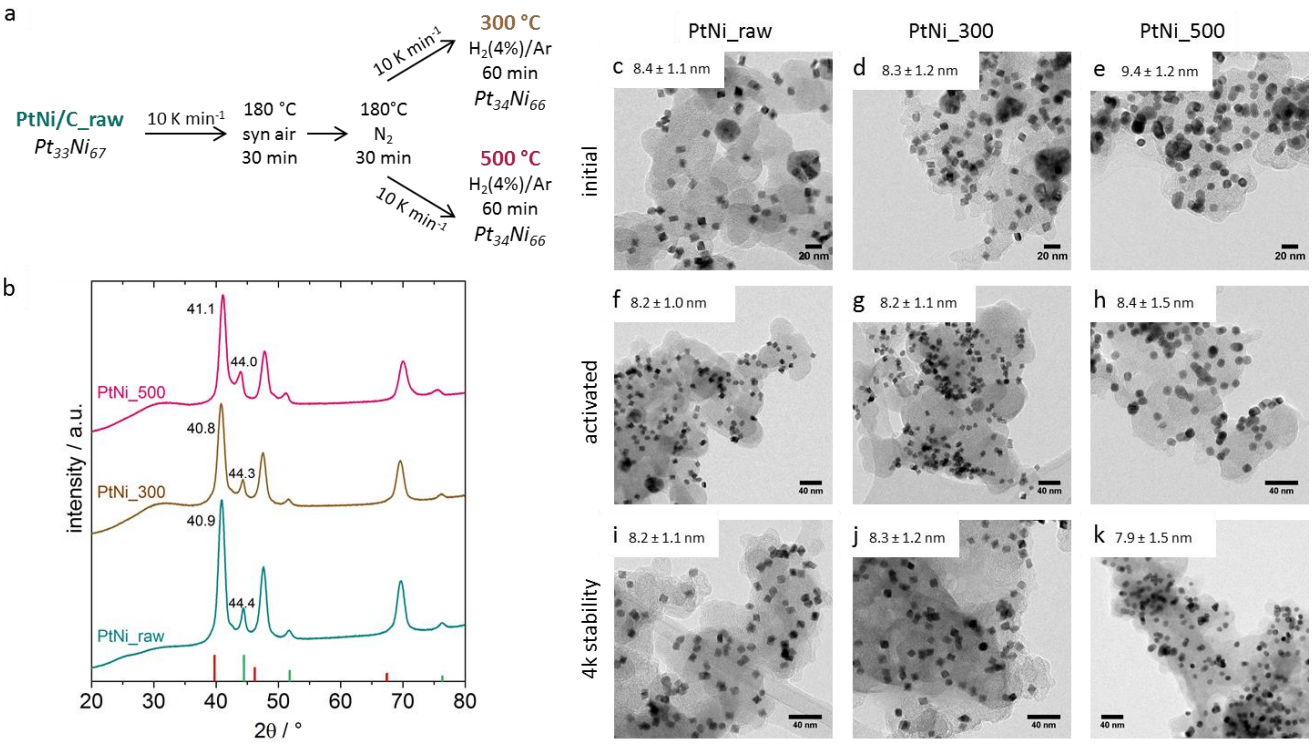

Figure 5.1 (a) Overview of samples including the schematic process of the annealing procedure performed in a tube furnace; The shown compositions are determined by ICP OES; Physicochemical characterization of octahedral Pt-Ni/C. **(b)** XRD pattern of *PtNi_raw*, *PtNi_300* and *PtNi_500*. Red columns correspond to pure P (PDF#00-004-0802) peaks and green columns to pure Ni (PDF#00-004-0850). TEM images of the samples **(c-e)** in the initial state, **(f-h)** after activation and **(i-k)** after 4k electrochemical stability treatment.

Ex situ XRD analysis. The XRD patterns (Figure 5.1b) of all three samples show peaks identifying a Pt-rich Pt-Ni alloy at 2θ values of around 41 ° (111), 47 ° (200) and 70 ° (220). Additional smaller peaks can be observed at around 44 °, 52 ° and 76 ° (Figure 5.1b) which indicate the presence of a Ni-rich phase. As suggested by EDX mappings discussed later on, these Ni-rich phases exhibit a small Pt rich core, which might cause a separate Pt peak, which probably is superimposed by the alloy peak. Comparison of the peak positions of the Pt-Ni (111) peaks for all materials (numbers in XRD pattern Figure 5.1b) reveal a shift to slightly larger Bragg angles with increasing annealing temperature above 300 °C, while the Ni-rich (111) peaks shift in the opposite direction. To support this assumption Rieveld analysis was performed in order to obtain information about the different alloy phases. Generally, all patterns are described by two PtNi phases and one Ni phase, all based on Pt fcc. The phase

compositions (Table S2.1), refinement patterns (Figure S2.1) and refinement details (Table S2.2) are shown in the supporting information. According to these results we achieve a main PtNi phase with a constant ratio (~65 %) at all three temperatures. With increasing temperatures the concentration of the Ni phase decreases, whereas the second PtNi phase increases. The Ni phase of PtNi_500 exhibit a larger lattice constant in comparison to the other samples which indicates an interdiffusion of the big particles with the observed small Pt-rich cores as seen in STEM EDX; forming a new alloy phase within the big particles. With that we conclude, that the main changes during annealing are happening on the big Ni-rich particles, which possibly alloy with their small Pt cores upon annealing. The main PtNi phase (~65 %), on the other hand, has a constant ratio during annealing up to 500 °C. But it has to be mentioned, that its lattice constant is slightly decreasing after annealing at 500 °C (Table S2.2). *In situ* TEM heating experiments discussed below provide further information for this suggestion.

Ex situ TEM analysis. TEM images of the three samples before electrochemical treatment (“initial”), are presented in Figure 5.1c-e. *PtNi_raw* and *PtNi_300* particles are mostly octahedrally shaped with a narrow size distribution (Figure S2.2a, b) and an average edge length of 8.4 ± 1.1 and 8.3 ± 1.2 nm, respectively. However, after 500 °C annealing temperature the previously octahedral particles became predominantly spherical in shape, with an average diameter of 9.4 ± 1.2 nm. In addition to the octahedral particles, large, roughly spherical particles are observed in the initial samples with a size around 20 nm in diameter. According to STEM EDX shown and discussed further below these particles are mostly consisting Ni. By counting the number of octahedral and big particles on different catalyst agglomerates the ratio of big Ni particles was estimated to be only ~4 %. These Ni-rich particles offer great opportunity to study not only effects of temperature and electrochemical characteristics on octahedral shaped nanoparticles but also on less precious components like Ni. For all three samples the nanoparticles are homogeneously distributed on the carbon support.

In situ TEM analysis during annealing. In order to study the morphological changes of the samples during annealing, *in situ* heating TEM experiments were performed (Figure 5.2). During the experiment, the specimen was heated in vacuum with the temperature increasing incrementally from 180 °C to 700 °C during approximately 2 hours. The octahedral particles maintain clear edges up to 450 °C, but at temperatures higher than 475 °C the corners start to round off and at 525 °C some closely neighboring particles start to coalesce. Figure S3 shows enlarged images of the marked particles from Figure 5.2 to facilitate traceability of nanoparticle changes. This observation confirms the *ex situ* observation that the octahedral particles had become spherical in *PtNi_500*. Above 600 °C the large Ni-rich particles appear to shrink rapidly, leaving behind a smaller particle that appears stable above 675 °C. This can most likely be explained by Ni atoms from the Ni-rich phase becoming mobile at high temperature and incorporating into the Pt-rich particles. This is consistent with the *ex situ* XRD observations in Figure 5.1b which indicated a convergence of the different phase compositions with increasing temperature.

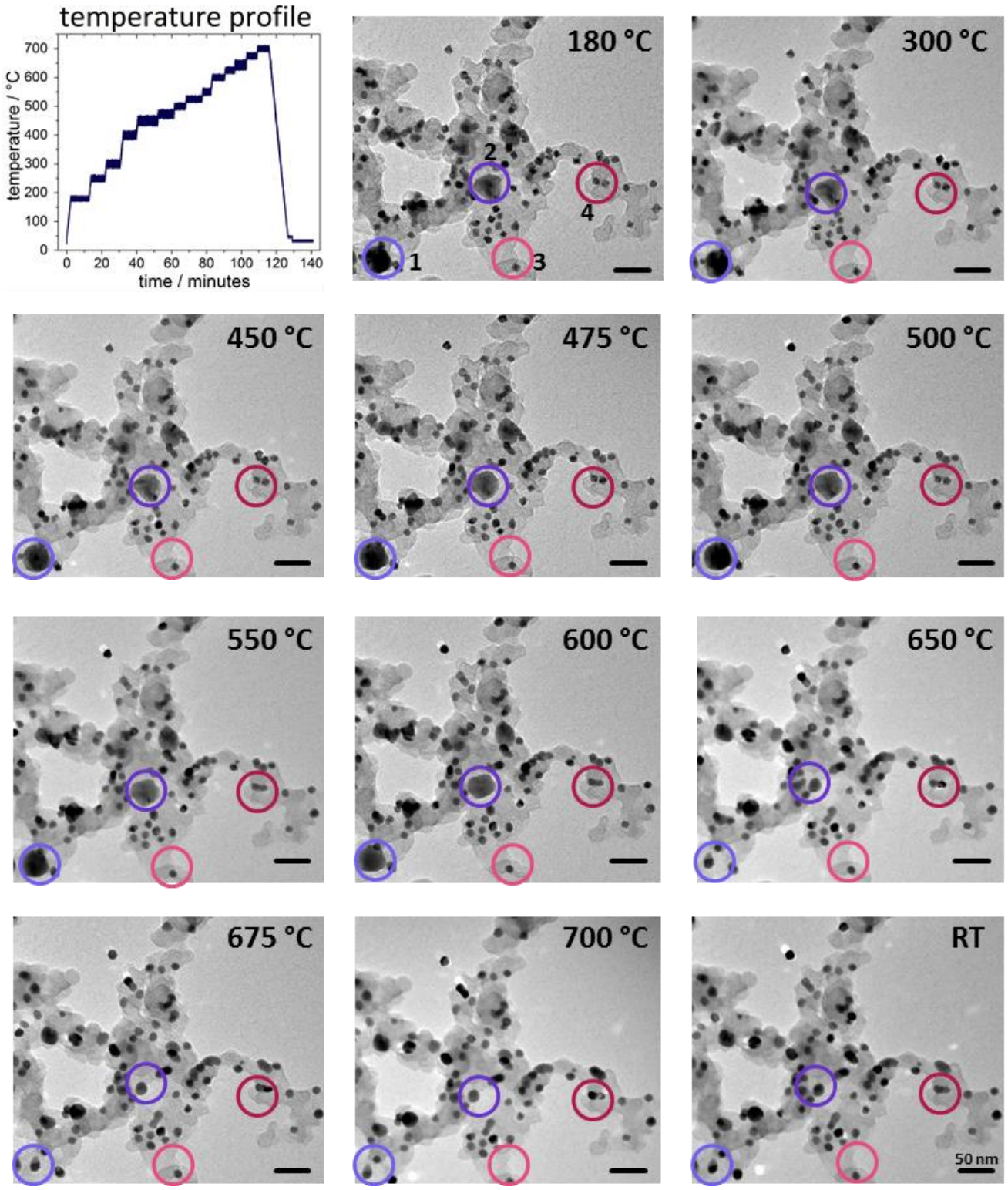

Figure 5.2 *In situ* heating TEM images of *PtNi_raw* in vacuum from room temperature (RT) up to 700 °C (temperature profile). Purple circles indicate the evolution of the bigger, Ni-rich particles during temperature treatment. Pink circles are emphasizing the change of the octahedral particle shape during heating. Numbers in the 180 °C image are referring to Figure S2.3.

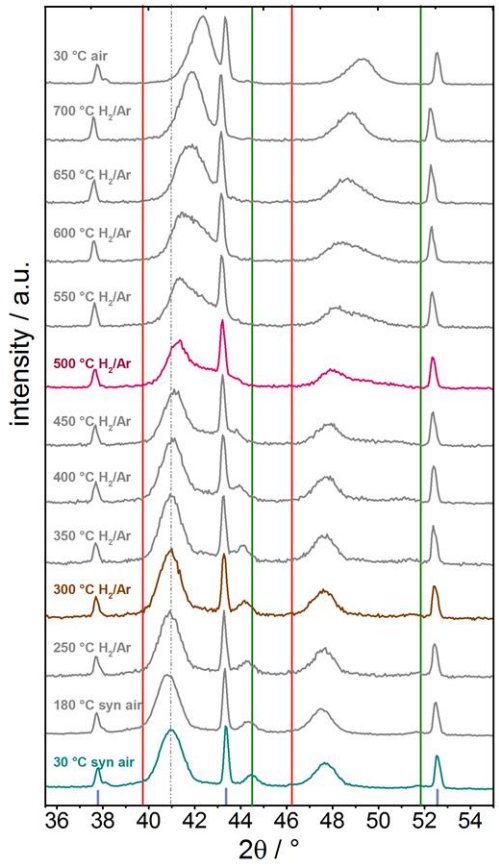

Figure 5.3 *In situ* heating X-ray diffractograms of the (111) and (200) signals of *PtNi_raw* in the temperature range between 30 °C and 700 °C. Gas atmospheres were chosen comparably to the *ex situ* annealing conditions in the tube furnace and temperature range was chosen according to the *in situ* heating TEM experiment. Red lines are assigned to pure Pt peaks, greens lines to pure Ni and blue columns to Al_2O_3 caused by the high temperature holder. The dashed line at around 2θ = 43 ° provides orientation of the shift of the main alloy peak.

In Situ XRD Analysis during annealing. To better understand our observations during the *in situ* heating TEM experiments, complementary *in situ* high temperature XRD (HT XRD) experiments were performed. In particular, the position of the (111) diffraction peak was monitored to follow our hypothesis about a gradual Ni incorporation into the prevalent Pt-Ni alloy phase. To ensure good comparability of the data, *in situ* XRD patterns were measured under identical conditions as *ex situ* data, where the cleaning step in synthetic air was followed by reduction in hydrogen/argon (see Figure 5.1). The temperatures were chosen in the same range to match the *in situ* TEM experiment (see temperature profile Figure S2.4c). The obtained XRD patterns are depicted in Figure 5.3 where the pattern of the initial sample (*PtNi_raw*) measured at 30 °C in synthetic air is shown in turquoise. The main (111)-alloy peak is tagged by the gray dotted line at 2θ = 40.94 °. With increasing temperature the maximum of the peak is shifting to higher 2θ values, showing a similar trend as observed for the *ex situ* patterns, and becomes slightly asymmetric. The Ni peak at 2θ = 44.48 ° however was slightly shifting to lower values during heating. After the heat treatment and cooling down to 30 °C the (111) peak shifted to 2θ = 42.38 ° and the previously present Ni peak at 2θ = 44.48 ° is no longer visible. The discrepancy between the absolute values of the *ex situ* and *in situ* XRD patterns could be caused mainly by the temperatures and the

gas atmospheres at which the patterns were recorded. To correct for the influence of the temperature itself on the peak shifts and lattice constant changes, identical control HT XRD experiments were performed using carbon-supported pure Pt and pure Ni metal nanoparticles of comparable size. Figure S2.4a,b show the diffraction pattern of Pt/C and Ni/C and the impact of temperature on the position of the (111) peak. Figure S2.4d is summarizing the changes of the maximum peak position as a function of the temperature. For the pure Pt and Ni metal nanoparticles, the Bragg angles are decreasing with increasing temperature due to an expansion of the metal lattice while the Bragg angles for the Pt-Ni alloy are showing the opposite trend. These findings confirm the assumption that Ni is incorporated in the main Pt-Ni alloy during annealing in hydrogen to form an alloy and therefore, the peak is shifting to higher 2θ values in contrary to the usual metal behavior. The slightly asymmetric shape of that peak suggests a non-uniform incorporation of Ni into Pt-Ni.

The combined results from the *in situ* and *ex situ* XRD and TEM experiments suggest that annealing in oxygen followed by hydrogen atmosphere leads to more Ni-rich alloys compared to the *PtNi_raw* particles which could be followed by the peak position in XRD. In more detail, two processes are taking place during annealing, as suggested and supported by the combination of Rietveld analysis, *in situ* heating TEM and *in situ* XRD; 1) the formation of a Ni-rich Pt-Ni alloy within the big Ni particles by alloying Pt from the core with surrounding Ni at temperature up to ~ 500 °C, and 2) incorporation of Ni-rich alloys into neighboring former octahedral particles at temperature above 600 °C.

Cyclic voltammetry. The particles were then subjected to cyclic voltammetry under oxygen-free conditions in a three electrode rotating disc electrode setup, and subsequently tested for the catalytic ORR. The oxygen-free cyclic voltammetric profiles of each catalyst are shown in Figure S2.5a-c. Evolution of characteristic waves inside the underpotential hydrogen deposition/desorption region (0.05 to 0.4 V_{RHE}) suggested the gradual faceting of the octahedral particles and, in correlation with the catalytic data, gave insight into the observed time evolution of the catalytic ORR behavior. Figure S2.5a-c display the "initial" state (the very first cycle), the "activated" state (the 20th cycle) and the state after 4000 potential cycles ("after 4k cycles"). The surface redox features during the 1st cycles were quite comparable for *PtNi_raw* and *PtNi_300* (Figure S2.5a,b), however, grew more pronounced during the 20th cycles. After 4k stability test *PtNi_300* displayed a new distinct redox feature at 0.4 V_{RHE}, possibly caused by the formation of an additional facet during the surface restructuring of the particles. The CVs of *PtNi_500* generally deviated from the ones of *PtNi_raw* and *PtNi_300*. Only one pronounced redox peak is visible in the H_{upd} region, with the strongest intensity in the activated state. Correlating the electrode potentials of these redox features with literature allows for insight in the presence and accessibility of specific surface: The Pt surface-adsorbate adsorption energy of H_{ad} and hence, their electrochemical redox potential, is increasing in the order (110) < (100) < (111)[129], and hence affect the resulting ORR activity in distinctly different ways.

Catalytic ORR activity and stability. The mass-based electrocatalytic ORR activities are reported in Figure 5.4a, obtained by linear sweep voltammetry (LSV) after electrochemical activation by surface conditioning during 20 cycles (denoted as "activated" in Figure 5.4) and after stability testing consisting of 4 000 electrochemical cycles (denoted as "4k stability") (LSVs are shown in Figure S2.5d). After activation the mass based activity of *PtNi_300* reached a *reproducible* high value of 2.7 A mg_{Pt}^{-1}, by far outperforming the activity of *PtNi_raw* (1.7 A mg_{Pt}^{-1}) and *PtNi_500* (0.7 A mg_{Pt}^{-1}). After the stability test the activity of *PtNi_300* dropped to 1.1 A mg_{Pt}^{-1} corresponding to a loss in activity of 60 %. In contrast, the activities for *PtNi_raw* and *PtNi_500* did not exhibit any statistically significant degradation.

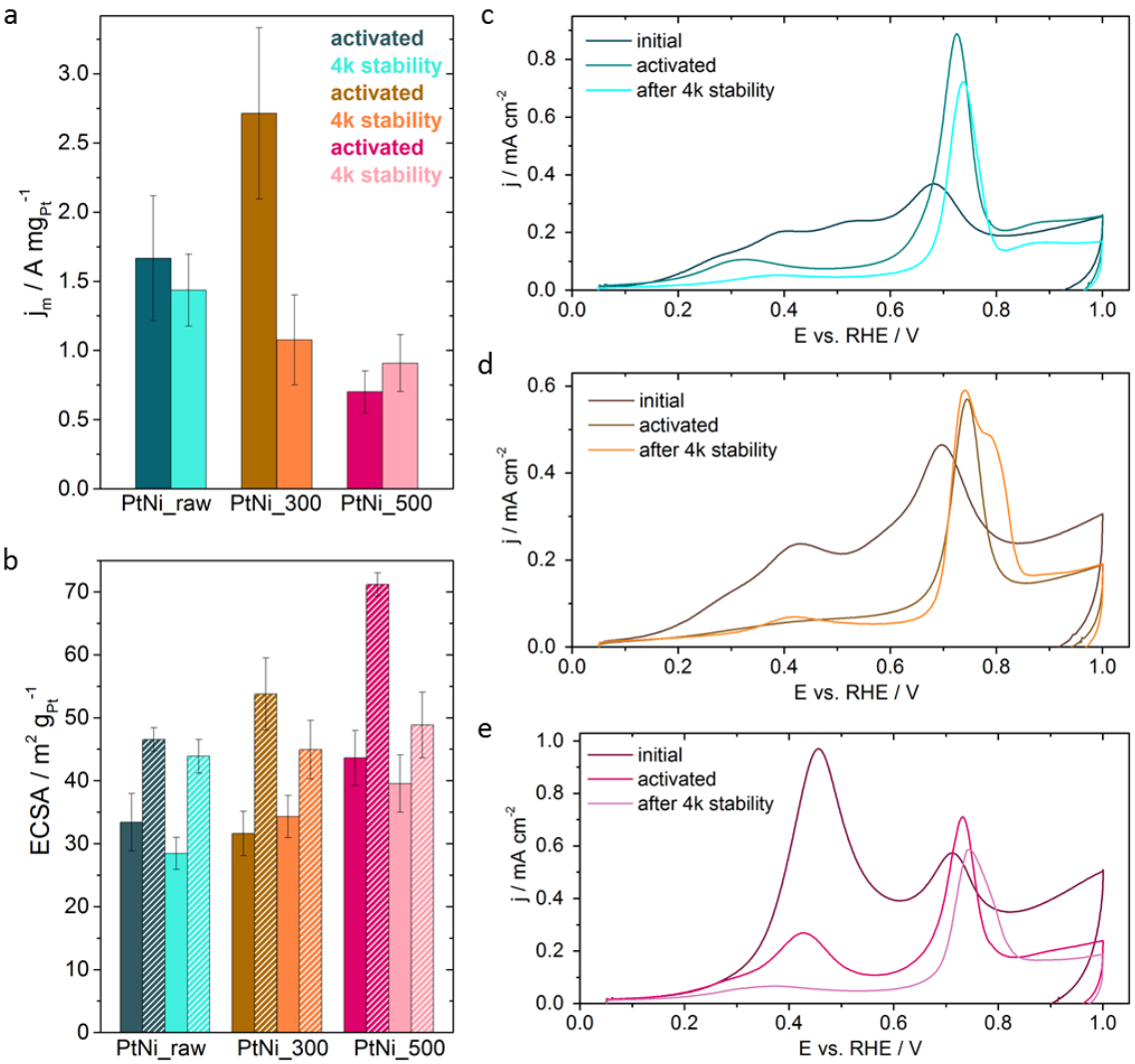

Figure 5.4 (a) Electrochemical ORR activity of the activated state (after 20 cyclic voltammograms (CV) activation) and after 4k stability test (4 000 CV stability measurement) evaluated at 0.9 V; ORR was measured in O_2 sat. 0.1 M $HClO_4$ between 0.05 and 1.0 V_{RHE} with 5 mV s^{-1}, 1600 rpm and were iR corrected **(b)** Electrochemical active surface area determined by integration of the hydrogen under potential deposition region (H_{upd}) (solid colors) and the CO oxidation peak (striped colors) after activation and 4k stability test. The error bars depicting the standard deviation between at least three different and independent measurements of freshly prepared catalyst films. **(c-e)** Positive CO oxidation profile of the initial samples, activated and after 4k stability test. H_{upd} values were evaluated from CVs measured in N_2 sat. 0.1 M $HClO_4$ between 0.05 and 1.0 V_{RHE} with 100 mV s^{-1} H_{upd}, CO oxidation was performed in N_2 sat. 0.1 M $HClO_4$ between 0.05 and 1.0 V_{RHE} with 50 mV s^{-1} and 0 rpm. 4k cycles stability test were measured in N_2 sat. 0.1 M $HClO_4$ between 0.5 and 1.0 V_{RHE} with 50 mV s^{-1}.

TEM morphology. In order to explain and understand the distinctly different time evolutions of the catalytic ORR activity and stability of the three catalysts, first, we considered the possible role of changes in octahedral particle morphology. TEM images were taken after each electrochemical treatment. Figure 5.1f-k present representative TEM images of *PtNi_raw*, *PtNi_300* und *PtNi_500* after activation and after 4k stability measurement. The octahedral shape of *PtNi_raw* and *PtNi_300* remained unchanged after the activation and after the 4k stability test. Thus, the morphology of the octahedral PtNi particles itself does not account for the observed changes in ORR activity. However, as expected for the acidic environment, the images evidence that large (Ni-rich) particles disappeared already after activation for *PtNi*_300 and after the 4k stability test for the *PtNi_raw* sample. TEM images of *PtNi_500* after electrochemical treatment did not show any significant variations. Particles rarely coalesced after the 4k stability test (Figure 5.1i-k) and the particle size was stable within the error (Figure S2.2), so changes in activity cannot be a result of that.

CO stripping. To learn more about the possible influence of the catalyst surface composition on the drastic activity/stability differences between the annealed and non-annealed octahedral Pt-Ni particles, electrochemical CO oxidation ("CO stripping") according to the reaction equation

$$CO_{ad} + H_2O \rightarrow CO_2\,(g) + 2H^+ + 2e^-$$

was used. Electrochemical CO stripping is known to be an extremely surface-sensitive characterization of the surface composition and defect density. Figure 5.4c-e present the CO oxidation curves of the three catalysts at the various testing stages. The broad faradic features of the anodic CO voltammograms, considering their early CO oxidation onset, suggest that the initial particles ("initial") are quite Ni-rich in and below their surfaces[133]. Such Ni-rich domains are capable to activate water molecules and form Ni(oxy)hydroxides on their surface which reactively remove CO adsorbed on neighboring Pt sites as early as 0.2 V_{RHE}. Ni dissolution and sub-surface dealloying is likely contributing to these observed broad voltammetric profiles as well, especially prominent for the *PtNi_raw* catalyst with Ni dissolution appearing between 0.4 V_{RHE} and 0.5 V_{RHE}[134]. In the activated state, the broad features between 0.2 and 0.7 V_{RHE} are generally weakened. Noteworthy is the basically flat, only gradually increasing voltammetric profile of the most active *PtNi_300* catalysts with its sharp CO oxidation wave between 0.7 and 0.8 V_{RHE}. Here, Ni appears to be distributed evenly in sub-surface regions suppressing any distinct redox wave around 0.4 V_{RHE}. This is in contrast to the behavior of the other activated catalysts with their characteristic Ni domain-assisted CO oxidation waves around 0.4 V_{RHE} (see especially for the *PtNi_500* catalyst) indicating Ni surface domains with activated oxygenates[47,55,74]. The *PtNi_300* continues to display an exceptional behavior, as after 4000 cycles a CO oxidation wave around 0.4 V_{RHE} is appearing, contrary to the other two catalysts whose features are continuously fading due to Ni electro-dissolution. Furthermore an additional CO stripping current shoulder appears at a more anodic potential of 0.8 V_{RHE}, which is also present for *PtNi_500*, but by far not that strongly pronounced

According to literature, an early CO oxidation onset is caused by the competing adsorption of CO and OH species due to the reduced binding energy of Pt alloyed with Ni, so the CO blocking effect is diminished[133,135]. It is also important to consider the presence of a separate Ni rich phase in terms of inter-particle oxidation for some of the materials (after 0 cycles: all catalysts, after activation: *PtNi_raw*). López-Cudero *et al.* discussed the effect on CO oxidation potentials of inter-particle oxidation on Pt nanoparticles[136]. As Ni sites are adsorbing OH species in favor of CO, they might have a large effect on the CO oxidation potential. Taking *PtNi_raw* after 0 CV as an example, three oxidation features can be observed in the anodic CO oxidation scan. CO can only be adsorbed on Pt sites of the particle, while OH species can also be adsorbed on Ni sites. Taking the additional Ni sites into consideration several OH adsorption sites are plausible: separate big Ni particle, Ni or Pt sites on the octahedral facets and Ni or Pt sites on the octahedral edges and corners[137]. Thus, the presence of the big Ni particle could have an influence on the CO oxidation peak position. Since the early CO oxidation peak is less pronounced after activation, the presence of a separate Ni phase seems to play an important role for the initial particle characteristics. The CO oxidation results indicate for *PtNi_300* a stronger CO binding than both *PtNi_raw* and *PtNi_500*. *PtNi_500* however binds CO comparably weak as most of it becomes oxidized at low potentials.

Electrochemical surface areas. From the discussed CVs and CO stripping voltammograms the electrochemical active surface areas (ECSA) were calculated. The values are reported in Figure 5.4b. The solid bars are representing the ECSAs obtained by integrating the H_{upd} area and the striped ones are showing the ECSA values obtained by integrating the CO oxidation area. For *PtNi_raw* and *PtNi_500* the H_{upd} based and the CO based ECSAs are decreasing after the 4k stability test. For *PtNi_300* this is only true for the CO based ECSA, the H_{upd} based ECSA is slightly increasing. The small differences are within the estimated error of the measurements. The CO based ECSAs for Pt-Ni alloy systems typically are larger than the H_{upd} based[133,135]. *HAADF-STEM and EDX analysis.* To further understand the differences in activity and stability the atomic scale elemental distribution of the particles was studied by STEM and EDX analysis.

Figure S2.6 shows high angle annular dark field (HAADF) STEM images of Pt-Ni octahedral nanoparticles in different states and Figure 5.5 the corresponding EDX elemental maps. The EDX map of the octahedral *PtNi_raw* nanoparticle, oriented close to a ⟨110⟩ zone axis, indicates an enrichment of Ni at the {111} facets and a Pt-rich frame, which is pointed out by a Pt-rich stripe across the middle of the nanoparticles (Figure 5.5a). Additionally, a Ni rich surface is visible. EDX quantification yields an average composition of Pt 60 at.% and Ni 40 at.% (shown particle Pt 59 at. %, Ni 41 at. %) of the particles in the initial state (Figure 5.5a). After activation, EDX quantification shows a decrease of Ni with an average composition of Pt 70 at.% and Ni 30 at.% (shown particle Pt 70 at. %, Ni 30 at. %). Furthermore, the EDX elemental map in Figure 5.5g shows a change in the distribution of Pt and Ni: Instead of a Ni rich surface a thin Pt layer is observed at the outermost parts of the representative octahedron which can be interpreted as a thin Pt-rich skin on the facets of the octahedra. As

already shown by TEM (Figure 5.1i) the octahedral shape is retained after the 4k stability. The surface of the octahedron is still Pt-rich but the Pt layer appears a bit thicker in comparison to the state after activation. The average composition after the 4k stability test was Pt 74 at.% and Ni 26 at.% (shown particle Pt 74 at. %, Ni 26 at. %), hence a slight change of the composition towards more Pt is observed after cycling in comparison to the state after activation.

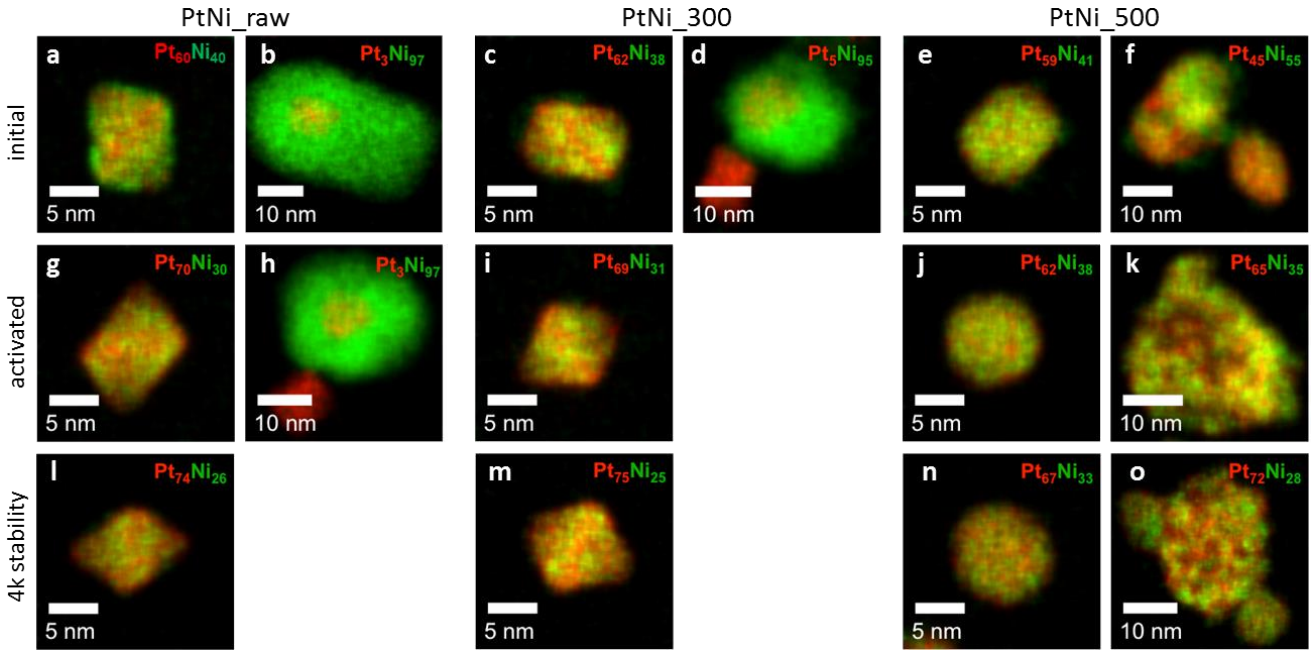

Figure 5.5 EDX elemental maps showing the composition of *PtNi_raw* **(a, b, g, h, l)**, *PtNi_300* **(c, d, i, m)** and *PtNi_500* (**e, f, j, k, n, o)** in the initial condition **(a-f)**, after activation **(g-k)** and after 4k stability test **(l-o)**. If present, also big irregular shaped mostly Ni-rich particles are depicted with their elemental distribution **(b and h, d, f and k and o)**; A minimum of 20 particles was investigated for each sample in order to determine an average particle composition. Pt: red and Ni: green.

In order to study the influence of annealing on the structural evolution during cycling, we investigated *PtNi_300* octahedral nanoparticles which were treated at 300 °C in 4 % hydrogen in the initial state, after activation and 4k stability test (Figure 5.5c, I, g and Figure S2.6c,i and m). While the EDX elemental map of the state after 300 °C as well as its activated state (Figure 5.5c, i) showed a comparable average Pt and Ni composition compared to the non-annealed *PtNi_raw* catalyst (Figure 5.5a and g) with Pt 62 at.%, Ni 38 at.% after 300 °C (shown particle Pt 65 at. %, Ni 35 at. %) and Pt 69 at.%, Ni 31 at.% after activation (shown particle Pt 68 at. %, Ni 32 at. %), the distribution of Pt and Ni is clearly changed comparing the *PtNi_raw* and *PtNi_300* sample. While Ni is mostly distributed at the surface of the *PtNi_raw* octahedra, it is located more on the inside in the *PtNi_300* octahedra. After activation, the elemental distribution was similar for *PtNi_raw* and *PtNi_300* with a thin Pt-rich layer which retains in the annealed sample after 4k stability compared to the thicker Pt layer which is observed in the non-annealed sample after the 4k stability. Due to the low signal to noise ratio, the thickness is hard to determine. A rough estimation for the Pt rich outer layer is 0.8 nm for PtNi_raw and 0.5 nm for PtNi_300 (see Figure S2.7). The average composition of the octahedral particles after 4k cycles was Pt 75 at.%,

Ni 25 at.% (shown particle Pt 75 at. %, Ni 25 at. %), respectively. Hence, again a dissolution of Ni is observed during the potential cycling procedure.

In order to explain the comparable composition and elemental distribution of *PtNi_raw* and *PtNi_300* after activation, even though the initial elemental distribution is different, it is reasonable to expect two different dissolution mechanisms: mainly Ni shell dissolution from the octahedral *PtNi_raw* nanoparticle surface (Figure 5.5a) resulting in the octahedron imaged in Figure 5.5g, losing around 10 at.% Ni, or, dissolution from the Ni-rich *PtNi_300* facets and Pt atom migration to the facets, losing around 7 at.% Ni. While that process is continued for *PtNi_300* during additional 4k cycles, resulting in a Pt-shell, Ni dissolution from *PtNi_raw* is less pronounced, however resulting in a thicker Pt-shell. A comparable fast formation of a relatively thick Pt-shell, protecting the particle from further Ni-dissolution, could be a possible explanation.

Finally we investigated the *PtNi_500* nanoparticles which were treated at 500 °C in 4 % hydrogen, in the initial state, after activation and 4k stability (Figure 5.5 and Figure S2.6e, j and n). As also shown by TEM (Figure 5.1c) the octahedral shape turns into a more spherical shape after annealing at 500 °C. This shape transformation is accompanied by a change in the elemental distribution (Figure 5.5e) in comparison to the raw material and the particles after 300 °C annealing. The edges and corners become round-off and the compositionally segregated structure inside the particles is lost towards a more homogeneously alloyed structure of the *PtNi_500* spherical particles (Figure 5.5e). After 500 °C annealing and activation (Figure 5.5j) as well as after the 4k stability test of *PtNi_500* the Pt-Ni distribution remains unchanged (Figure 5.5n). Hence, the hydrogen treatment at 500 °C has a destabilizing effect on the octahedral shape as well as on the elemental distribution. The average composition of the Pt-Ni particles in the state after 500 °C, after activation, and after 4k stability is Pt 59 at.%, Ni 41 at.% (shown particle Pt 62 at. %, Ni 38 at. %), Pt 62 at.%, Ni 38 at.% (shown particle Pt 63 at. %, Ni 37 at. %), and Pt 67 at.%, Ni 33 at.% (shown particle Pt 67 at. %, Ni 33 at. %), respectively. Hence, Ni dissolution is observed as well, but comparatively more Ni is retained in the alloyed structure even after 4k stability test.

Beside the presence of octahedral nanoparticles in *PtNi_raw*, additional larger irregular-shaped nanoparticles are observed (Figure S2.6b). Therein, Pt-rich cores are encased by Ni shells (Figure 5.5b). The overall composition of these very large nanoparticles is Pt 3 at.% and Ni 97 at.%. These nanoparticles are also found after activation (Figure S2.6h) but not after the 4k stability tests, which is due to the dissolution of their Ni shells after cycling in acidic media. The same is true for the 300 °C annealed sample (Figure S2.6d), but here the large nanoparticles are already dissolved after the activation treatment. In contrast, for the 500 °C annealed sample, the large nanoparticles are observed to exhibit a higher Pt (45 at.%) and a lower Ni content (55 at.%). The nanoparticle content changed to Pt 65 at.%, Ni 35 at.% after activation and Pt 72 at.%, Ni 28 at.% after 4k stability. Upon cycling, we observe a change of the structure as well as of the elemental distribution. After

the 500 °C treatment a more Pt-rich alloyed structure is observed (Figure S2.6f) which develops into a more sponge-like structure after activation and the 4k stability test (Figure S2.6k and o). This change is similar to the formation of porous structures already observed for big spherical Pt-Ni particles upon electrochemical dealloying[37,138].

In summary, our EDX elemental mapping results are in line with the XRD data and the CO stripping data. The origin of the dramatic activity difference between the activated *PtNi_raw* and *PtNi_300* was not immediately obvious, and will be clarified in the context of their stability.

In situ electrochemical FTIR spectroscopy studies. To further probe the chemical nature of the catalyst particle surfaces and to correlate it with the distinctly different ORR activities, *in situ* electrochemical FTIR spectroscopy of surface-adsorbed CO was employed to monitor changes in the vibrational characteristics as function of annealing at constant and varying electrode potentials (Figure 5.6 and Figure S2.8). The catalysts were compared in their activated state only. Figure 5.6a represents the wavenumbers of the stretching vibrations of linearly bonded CO, with *PtNi_500* exhibiting the highest wavenumbers (2063 cm^{-1}) followed by *PtNi_raw* (2054 cm^{-1}), and then *PtNi_300* (2048 cm^{-1}). All bands appear within the expected wavenumber range[139].

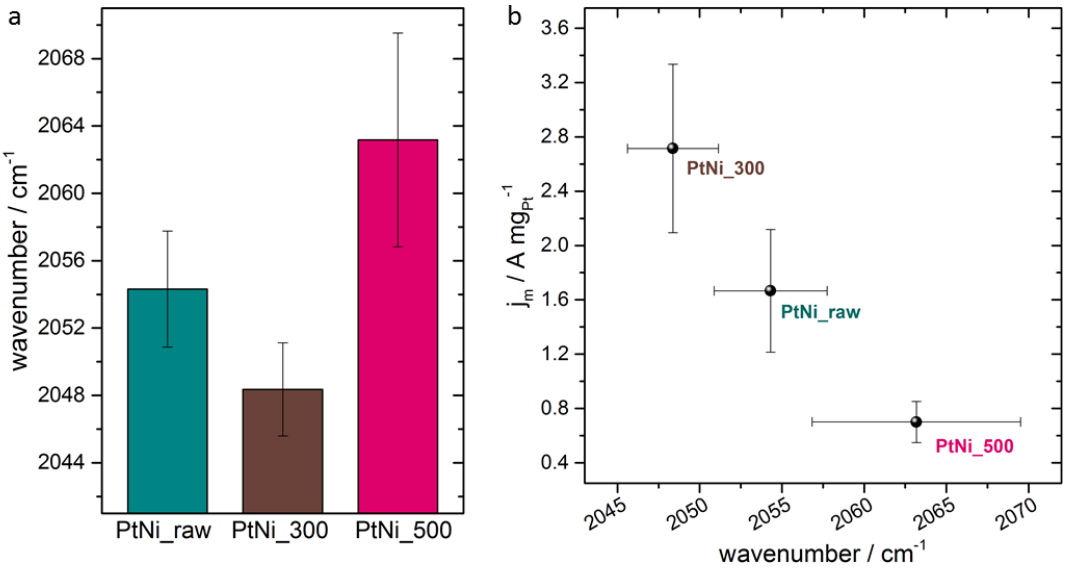

Figure 5.6 *In situ* FTIR spectroscopy measured in ATR mode. **(a)** Position of CO_{ad} band of the linear bounded CO collected at 50 mV_{RHE} in N_2 sat. 0.1 M $HClO_4$ for the different samples after electrochemical activation. **(b)** Correlation between ORR activity at 0.9 V_{RHE} and the CO_{ad} wavenumber obtained for the investigated set of particles. The error bars depicting the standard deviation between at least three different and independent measurements of freshly prepared catalyst films.

At this point it should be mentioned, that the presence of Ni particles should not have a major impact on the observed stretching vibrations, as Ni is a weak CO binding surface and if adsorbed they should appear at lower wavenumber regimes. In general, stronger CO surface chemisorption energies lower the C-O binding energy in the CO molecule and lower their C-O stretching frequency and wavenumber. Hence, *PtNi_300* exhibits a stronger CO chemisorption energy compared to *PtNi_raw* and *PtNi_500*.

Correlating these results with the corresponding ORR activities (Figure 5.6b) reveals that for shaped Pt-Ni alloys stronger chemisorption induces higher catalytic ORR activities. We conclude that *PtNi_raw* and *PtNi_500* bind surface species too weakly, resulting in overall lower ORR activities, while *PtNi_300* exhibits a stronger, more optimal binding strength. Translating these finding into a volcano plot behavior, one would expect *PtNi_raw* and *PtNi_500* on the weak-binding branch. *PtNi_300* must be shifted in closer absolute proximity to the top of the volcano while *PtNi_500* is farther away from the top on the weak binding branch. We need to mention that the observed wavenumber – ORR activity relation is likely to hold true for the family of shaped Pt-Ni particles with comparable size, and may not apply to other chemically distinct types of Pt-based materials. Nevertheless, as pure Pt is binding CO stronger than Pt-Ni alloys, the experimental trend in stretching frequencies on Pt-Ni octahedra confirms a fairly Pt-rich surface for *PtNi_300*, followed by a Ni-richer surface for *PtNi_raw* and the least Pt-rich surface for *PtNi_500*, which was exactly predicted by the *ex situ* CO stripping measurements (Figure 5.4c-e). This finding is important as it may allow evaluating ORR activity trends based on their CO stripping profiles.

Figure S2.8d,e,f show a representative set of *in situ* FTIR reflectivity spectra taken during CO stripping. Figure S2.8a,b,c show the voltammetry. After investigating the position of the linear CO stretching frequencies at a constant potential of 50 mV, the potential was slowly increased by 1 mV s^{-1} to follow the CO oxidation *in situ* and to track the changes in CO stretching frequencies while increasing the potential. The corresponding *in situ* electrochemical faradaic stripping voltammetry (Figure S2.8a-c) was essentially, though not perfectly, consistent with the equivalent *ex situ* voltammetry shown in Figure 5.4c-d, which was conducted in a three electrode RDE cell, not in the FTIR cell. This can be attributed to differences in FTIR cell geometry where the working electrode typically operates under diffusion limited conditions. Still, identical trends are found as in the *ex situ* CO stripping experiment. *PtNi_500* exhibited a pronounced early CO oxidation peak, while it was less pronounced for *PtNi_raw*, and emerged at more anodic potentials for *PtNi_300*. The reflectivity FTIR spectra were reported every 95 mV, and are referenced to the CO-free surface FTIR spectrum at 50 mV. All three materials are exhibiting the most intensive CO band at 50 mV, consistent with the chosen reference spectrum. With increasing potential all bands decline in intensity due to the oxidation of CO to CO_2. In comparison to *PtNi_raw* and *PtNi_500*, the highly active *PtNi_300* catalyst exhibited a bipolar band, possibly indicating a slightly thicker catalyst film on the electrode. We refrain from plotting the evolution of the CO band position against the potential, as too many factors such as the CO coverage, particle size, catalyst film thickness, and the 'Stark Effect' may influence the position of the CO band during the application of an electrode potential. The various effects of adsorbed CO on Pt nanoparticles in combination with *in situ* FTIR experiments have been extensively described and discussed in detail in the past[84,140-143]. However, effects on Pt-Ni alloy systems, especially octahedral shaped nanoparticles are very poorly assessed to date. For that reason, we used the measured positions of the measured CO stretching frequencies only to make a relative comparison of the binding and surface

energies among the catalysts investigated in this study, to avoid comparison of the absolute band positions with values reported in literature.

To prove that PtNi_raw is a suitable un-annealed reference for all the used methods, the impact of only a 180 °C synthetic air and a 180 °C H_2/Ar annealing step according to Scheme S1 was investigated as shown in the supporting information. These two newly added samples should illustrate the minor impact of possible remaining surfactants on the particle surface. We performed a similar set of electrochemical and spectroscopic characterization methods in order to avoid any uncertainties as can be seen in Figure S2.9-Figure S2.15.

5.2 Discussion

On the atomic origin of the ORR activity differences. Combining our findings from *ex situ* and *in situ* XRD, STEM-EDX, cyclic and scan voltammetry, *ex situ* RDE CO-Stripping as well as *in situ* FTIR CO stripping/CO stretching frequencies we are able to derive a more comprehensive molecular picture on the origin of the drastic variations in ORR activity and stability, which provides, in turn, a deeper understanding of the precise effect of annealing on the surface geometry and composition.

Moderate annealing at 300 °C followed by electrochemical activation by potential cycling resulted in an enhanced yet balanced chemisorption strength of adsorbed surface species compared to the unannealed *PtNi_raw* and the 500 °C annealed *PtNi_500* catalysts. *In situ* FTIR CO stretching frequencies, *ex situ* CO stripping and EDX spectroscopy suggest the presence of a Pt enriched surface, even though no differences in the EDX elemental mappings could be observed for the activated *PtNi_300* particles in comparison to *PtNi_raw*. This underscores the difficulties in unravelling the origin of electrocatalytic activity even using sophisticated STEM-EDX mapping due to a limited surface-compositional resolution. We show that CO adsorption is sensitive of extremely minute changes in the particle surface compositional structure, which even EDX spectroscopy is unable to resolve.

Although electrochemical activation of *PtNi_raw* and *PtNi_300* leads to a similar elemental distribution as seen in the EDX mapping, the initial state of the particles appears to have an equally great influence on the resulting surface characteristics and hence on the ORR activities, as indicated by the *in situ* FTIR/CO adsorption study. It has to be mentioned, that remaining ligands from the synthesis on the particle surface should play a minor role in terms of activity and stability, which has been also show by the comparison of different annealing treatments at 180 °C. The short-lived and evidently very active surface state after activation was no longer present after the 4k stability test of *PtNi_300*. This was because the stability-tested catalysts displayed a Pt-richer particle surface compared to its activated state, evidenced by the *ex situ* CO stripping profile and EDX mappings. Yet again, it was the CO stripping profiles that revealed subtle but highly important differences: The CO stripping profile of the *PtNi_300* catalyst after the 4k stability test in Figure 5.4d displayed the presence of a new faradaic CO

stripping wave at more anodic potentials attributable to a newly formed Pt-Ni phase with distinct atomic composition or surface structure. Closer inspection of the catalyst based voltammograms in Figure S2.5 revealed that the *PtNi_300* catalyst underwent more pronounced surface faceting after 4k cycling suggesting a stronger development of {110} and {100} facets in combination with the emergence of a platinum shell (Figure S2.5, dashed lines at around 0.15 and 0.25 V_{RHE}). Surface faceting is an ordering process where structurally and compositionally defined terraces and steps/kinks are formed under prolonged potential cycling. Additional evidence is given by HAADF images in Figure S2.6m, showing octahedral edges cut along the <100> direction, providing new reaction sites. *PtNi_raw*, in contrast, while exhibiting a similar CO stripping profile after activation as *PtNi_300*, showed no additional redox wave after the 4k stability test. Indeed, the characteristics of its main CO stripping peak, associated with the Pt-rich surface domains, remained essentially unchanged after the 4k stability test, and so did its EDX elemental mapping. Such Pt- or Pt-rich domains in the surface appear to help protect the particle from Ni corrosion/depletion and subsequent losses in ORR activity, as observed for *PtNi_raw*. The thinner Pt-shell of the *PtNi_300* catalysts, on the other hand, was affected more severely by the 4k stability cycles, presumably due to sub-surface Ni. Ni atoms in sub-surface regions dissolved from surface, which aided the partial surface faceting into Pt rich terraces and steps, whereas *PtNi_raw* with its Pt-richer surface remained in a slightly more stable state.

PtNi_500 showed a distinctly different behavior in terms of particle shape, CO stripping profile, elemental composition of individual particles and ORR activity and stability behavior. The catalytic ORR activity of octahedral PtNi nanoparticles is known to depend on shape or elemental atomic distribution[47,63]. For *PtNi_500* both phenomena apply. After the thermal annealing the octahedral shape was no longer well defined (Figure 5.5e), and consequently exposed a smaller ratio of {111} facets. In addition, the anisotropic elemental distribution inside the particles was lost in favor of a more homogeneously alloyed structure. This is why *PtNi_500* was less active as activated catalyst in comparison to *PtNi_raw* and *PtNi_300*. Furthermore, during the electrochemical 4k stability test the particles became Pt enriched in comparison to their initial state (Figure 5.5e, j, n), which would explain the gain in ORR activity. Additionally, the initially Ni-rich particles became also more Pt rich, resulting in additional reaction sites (Figure 5.5f, k, o). Those Ni-rich particles are no longer present for *PtNi_raw* and *PtNi_300* for which no significant changes in shape and anisotropy could be observed, either. The CO stripping profile after 4k cycles again displays a newly formed redox wave at higher anodic potentials, although less pronounced than for *PtNi_300*, suggesting the formation of more facetted reaction sites. A mixture of different facets is reasonable to assume, due to the shape of the spherical particles, resulting in lower intensities of each peak respectively. Furthermore, the former Ni rich particles exhibit a sponge like structure including more defects which could provide additional reaction sites Figure S2.6f, k, o)[144,145]. As suggested by the *in situ* FTIR-CO stripping, *PtNi_500* is binding reactive surface species too weakly to achieve ORR activities as high as for *PtNi_raw* and *PtNi_300*. Oxidized surface Ni does not bind CO strongly either. A

Pt-poor surface is evidenced by the *ex situ* CO stripping results as for both, the initial and activated state have very broad and early CO oxidation peaks.

Our analysis reveals that a successful tuning of the Pt-Ni octahedral particle surface toward high catalyst activity and stability requires a sensitive balance between Ni enrichment in the surface and sub-surface, shape stability and fine structure of the particle surface, which is hard to achieve by synthetic wet-chemical synthetic methods alone. Annealing in defined gas atmospheres, however, is a powerful and sensitive-enough tool to achieve such a careful fine-tuning of alloy nanoparticle surfaces to ensure optimal ORR activity.

5.3 Conclusion

We have shown that annealing of Pt-Ni based shaped particles is an effective way of post-synthesis treatment to clean and modify particle surfaces in order to obtain high ORR activities and improved stabilities. We studied different parameters to gain a deeper understanding in the material during heat treatment. Therefore, *in situ* heating transmission electron microscopy and X-ray diffraction experiments were performed to follow the morphological and structural changes. We have proven that annealing at elevated temperatures in reducing atmosphere has an impact on the alloy composition as well as on the particle shape. Especially, if one would desire to preserve a certain particle shape, a temperature treatment must be carried out very carefully. As presented, an annealing protocol has also an influence on the electro-catalytic ORR activity and stability. While it is possible to boost the initial activity, compromises in terms of stability have to be made. By using a combination of electrochemical surface characterization techniques like CO oxidation and EDX spectroscopy we were able to explain the observed activity and stability trends. Further and deeper understanding of the catalyst surface was received by *in situ* FTIR spectroscopy using CO as a probe molecule, showing a correlation between CO binding energies and ORR activity. Taking all used methods into consideration it became evident that annealing could be used to efficiently and carefully tailor the catalyst surface, where inducing small changes in the surface-reactant binding energies could drastically help to improve the catalytic ORR activities. Furthermore, we conclude that a compromise between a very active and stable surface is required.

6. Tuning the Catalytic Oxygen Reduction Reaction Performance of Pt-Ni Octahedral Nanoparticles by Acid Treatments and Thermal Annealing

Accepted manuscript reproduced from J. of The Electrochem. Soc. **2018**, *165(15), J3026-J3030 (Reference* 146*).* This paper is part if the JES Focus Issue on Electrocatalysis – In Honor of Radislav Adzic, *Open access article distributed under the terms of the Creative Commons Attribution 4.0 License (CC BY).*

Vera Beermann, Stefanie Kühl, and Peter Strasser, *JES* **2018**, 165(15), J3026-J3030, DOI: 10.1149/2.0051815jes (http://jes.ecsdl.org/content/165/15/J3026.full)

V.B. planned, designed and performed octahedral nanoparticle synthesis and electrochemical characterization. S.K. performed TEM measurements and Rietveld analysis. All authors participated in analyzing the data, discussing the results and writing the manuscript.

Shape controlled octahedral Pt-Ni alloy nanoparticles are promising oxygen reduction reaction (ORR) electrocatalysts for cathodes of low temperature Polymer Electrolyte Membrane fuel cells. Organic surfactants are used in order to control and tune particle composition, size, shape, and the distribution on the support material. Such methods request intense post-synthesis cleaning, or annealing procedures in order to remove the ligands, demanding for simpler cleaning and activation procedures. Here, we explore the effect of an acetic acid treatment of as-prepared Pt-Ni particles, applied prior to annealing. The resulting nanoparticles underwent an electrochemical surface characterization and were investigated in terms of their ORR activities and electrochemical long-term stability. After acid treatment the particles exhibit a Pt-rich surface, which changed slightly during annealing at 300 °C but drastically to a more homogeneous alloy after annealing at 500 °C due to Ni surface segregation. Besides changes in the (sub-)surface Pt and Ni composition, the octahedral shape did not survive the 500 °C treatment. An improved ORR activity was obtained after annealing at 300 °C. Our insights into effects and benefits of the described post-synthesis treatments aid our general understanding, but also in the practical design of suitable treatment protocols of this class of ORR catalyst.[146]

In a previous study, a series of thermally annealed Pt-Ni octahedral particles were prepared and characterized in terms of their shape evolution and changes in degree of alloying during heating[132]. In this chapter, we systematically investigate the impact of combined acid leaching/annealing treatments on the catalytic ORR activity and corresponding electrochemical stabilities of the alloy ORR catalysts. More specifically, the impact of acetic acid treatment coupled to an annealing protocol will be investigated in terms of ORR activity after activation and 4k cycles stability measurement. Electrochemical CO oxidation voltammetry is used as a probe in order to analyze the nanoparticle surface characteristics. We derive valuable information in terms of their catalytic behavior, surface and sub-surface condition and Pt *versus* Ni enrichment in the surface from that.

6.1 Results

The Pt-Ni/C catalysts were prepared using a wet chemical synthesis approach including OAm and OAc as surfactants and $W(CO)_6$ as reducing agent. The as-prepared Pt-Ni/C particles underwent different post-synthesis treatments: first, treatment in acetic acid (HAc) in order to i) remove organic surfactants and ii) leach and deplete the surface in Ni. After the acetic acid leaching, the particles were exposed to an annealing procedure reported previously[132]. The particles were first annealed in synthetic air for 30 minutes, followed by a reduction step for 1 h in a hydrogen atmosphere at two different temperatures, namely 300 °C (HAc_300) and 500 °C (HAc_500) (Figure 6.1A). The molar metal composition of the as-prepared Pt-Ni/C sample was $Pt_{33}Ni_{67}$, that of the HAc-treated catalyst $Pt_{70}Ni_{30}$ and $Pt_{72}Ni_{28}$ for HAc_300 and HAc_500, respectively.

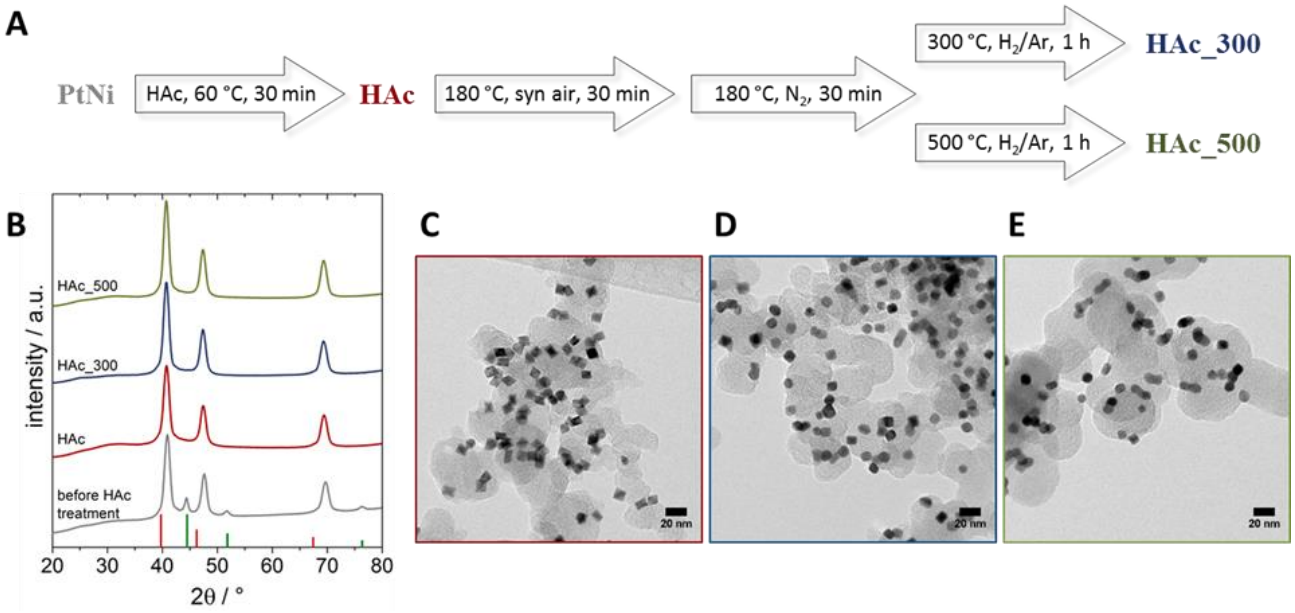

Figure 6.1 Introduction of samples; **A)** Scheme of post-synthesis samples treatment; **B)** X-Ray diffraction patterns of the Pt-Ni/C samples after post-synthesis treatment in comparison to the untreated sample, red columns indicate the reflection position of pure fcc Pt (#00-004-0802), green columns indicate the reflection position of pure fcc Ni (#00-004-0850); **C-D)** TEM images of the Pt-Ni/C samples after post-synthesis treatments, HAc **(C)**, HAc_300 **(D)**, HAc_500 **(E)**.

Acid leaching had a significant effect on the long-range crystal structure and the corresponding XRD patterns (Figure 6.1B). Prior to HAc leaching a separate Ni phase is clearly present at Bragg angles of around 44°, 52° and 76°, which disappeared completely after leaching (HAc). A Pt-enrichment of the Pt-Ni alloy phase after leaching is evidenced by the reflections at 2Θ values of around 41°, 47° and 69°, which are located between the fcc reflections of pure Pt and pure Ni, and slightly shifted to lower 2Θ values in comparison to the as-prepared samples. Detailed Rietveld refinement suggested two distinct Pt-Ni phases for the HAc treated samples, further supporting the removal of the Ni phase. In comparison to the previously reported series of samples[132], where we found a Ni-rich phase besides main Pt-Ni phase, no additional Ni-rich phase was present after the leaching procedure, and the experimental crystalline lattice constants were slightly larger, indicating some Ni leaching from the main Pt-rich Pt-Ni phases[132] (Table S3.1 Table S3.2, Figure S3.1). Interestingly, once the HAc treatment was applied, the annealing temperature itself had only a minor influence on the resulting crystallite size; it was only the alloy phase composition that changed after the combined HAc leaching/ 500 °C annealing (Table S3.1). TEM images revealed intact octahedral shape for the HAc sample with an average edge length of 8.2 ± 1.2 nm (Figure 6.1C and Figure S3.2), which is on the same order of magnitude as before HAc treatment (8.4 ± 1.1 nm)[132](Figure S3.2). For HAc_300 (Figure 6.1D and Figure S3.2), octahedral edges are mostly rounded off, which is in contrast to our previous study without the preceding HAc treatment; there, the octahedral shape was retained and stable after the 300 °C treatment[132].

After annealing at 500 °C, the octahedral particle shape was almost completely lost, and particles in close proximity coalesced (Figure 6.1E and Figure S3.2). It is important to note that the acetic acid treatment itself did not change the original octahedral shape (Figure S3.2), but did induce corrosive defects in the particle surface, which promoted a loss in shape during subsequent heat treatment.

To investigate the effect of the combined acetic acid/annealing treatment on the surface properties of the catalysts and their catalytic ORR performance, the three materials were investigated in a three-electrode rotating disc electrode setup. Figure 6.2A-C show the cyclic voltammetry in oxygen-free conditions normalized to the amount of Pt on the electrode. This analysis reveals the surface electrochemical faradaic and capacitive behavior of the catalyst surface in absence of catalytic reactants. Hydrogen under potential deposition (H_{upd}) regions are well-developed for HAc (Figure 6.2A) and HAc_300 (Figure 6.2B) in the initial as well as in the activated state; they indicate the presence of Pt atoms and domains at the particle surface. Characteristic redox waves at around 0.2, 0.3 and 0.4 V_{RHE} sharpen with progressing electrochemical cycling up to 4k cycles, suggesting the faceting of the Pt-rich surface[72,129]. For HAc_500, the H_{upd} region is only weakly developed in the initial state and after activation, indicating a rather Ni-rich surface (Figure 6.2C) due to a more homogeneous alloy surface (Pt and Ni distribution) after annealing at high temperature[132]. After 4k cycles, similar H_{upd} features like for HAc and HAc_300 can be observed, now suggesting a Pt-richer surface due to metal dissolution.

To learn more about the surface characteristics, electrochemical CO oxidation was used (Figure 6.2D-F). The CO stripping profiles of all three materials showed a main CO oxidation peak at around 0.7 V_{RHE}, whereas the development of the main peak position was different within the materials with prolonging cycle number. Generally, the position of the main CO stripping is influenced by the adsorption strength of CO to the particle surface. A shift to higher potentials was caused by stronger adsorption energies of CO and can be interpreted as a Pt enrichment of the nanoparticle surface. HAc exhibited a more anodic peak potential after activation, compared to the initial and the after 4k stability state (Figure 6.2D). HAc_300 showed a more anodic peak potential after activation, which remained constant after 4k potential cycles. Importantly, an additional shoulder at around 0.8 V_{RHE} appeared after 4k cycles, suggesting the emergence of a new surface site or facet with somewhat stronger CO binding. For HAc_500, the position of the main CO oxidation peak increasing in potential after 4k cycles, indicating again the formation of a Pt-enriched particle surface, probably due to Ni-leaching from the more homogeneous alloy surface.

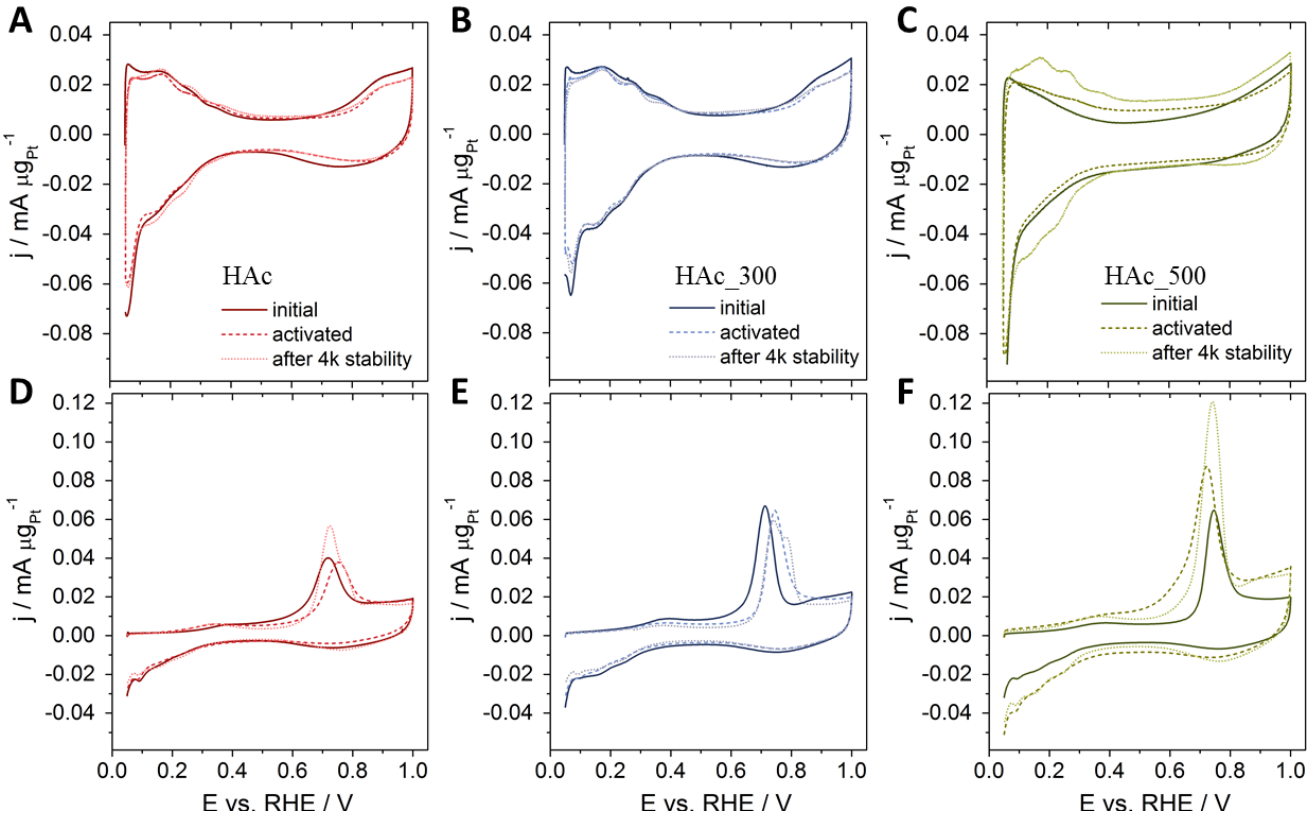

Figure 6.2 Electrochemical surface characterization of Pt-Ni/C after post-synthesis treatment. **A-C)** Cyclic voltammograms recorded in N_2 sat. $HClO_4$ with 100 mV s^{-1} between 0.05 and 1.0 V_{RHE} of the initial samples, after activation and after 4k cycles stability test; CO oxidation profiles recorded in N_2 sat. $HClO_4$ with 50 mV s^{-1} between 0.05 and 1.0 V_{RHE} after purging with CO. Red lines indicate the sample HAc **(A, D)**, blue line the samples HAc_300 **(B, E)** and green lines the sample HAc_500 **(C, F)**.

From the electrochemical surface voltammetries of hydrogen and CO, the electrochemical active surface areas (ECSAs) were determined. Figure 6.3A shows the numbers for the ECSA obtained by integrating the charges associated with hydrogen under potential deposition (H_{upd}) and CO oxidation normalized to the respective charge

densities. All three catalysts exhibited a similar H_{upd} ECSA in their initial state and after activation (Figure 6.3A, solid bars, dark and medium colored) while after 4k cycles (Figure 6.3A, solid bars, lighter colored) the one for HAc_300 stays constant in comparison to the ones of HAc and HAc_500 which slightly increase (see also Figure **6.3**B). In contrast, CO stripping revealed larger ECSA values, which was expected for Pt-alloy based systems, but they also showed a quite different trajectory after 4k cycles stability (Figure 6.3A, hatched bars). HAc and HAc_500 values decreased or stayed constant within the error compared to the activated state. HAc_300, however, which showed constant ECSA values based on H_{upd}, showed a drastic increase in ECSA value after 4k cycles (see also Figure 6.3B). This observation suggest the formation of an additional surface side, which do not adsorb hydrogen but CO and OH species.

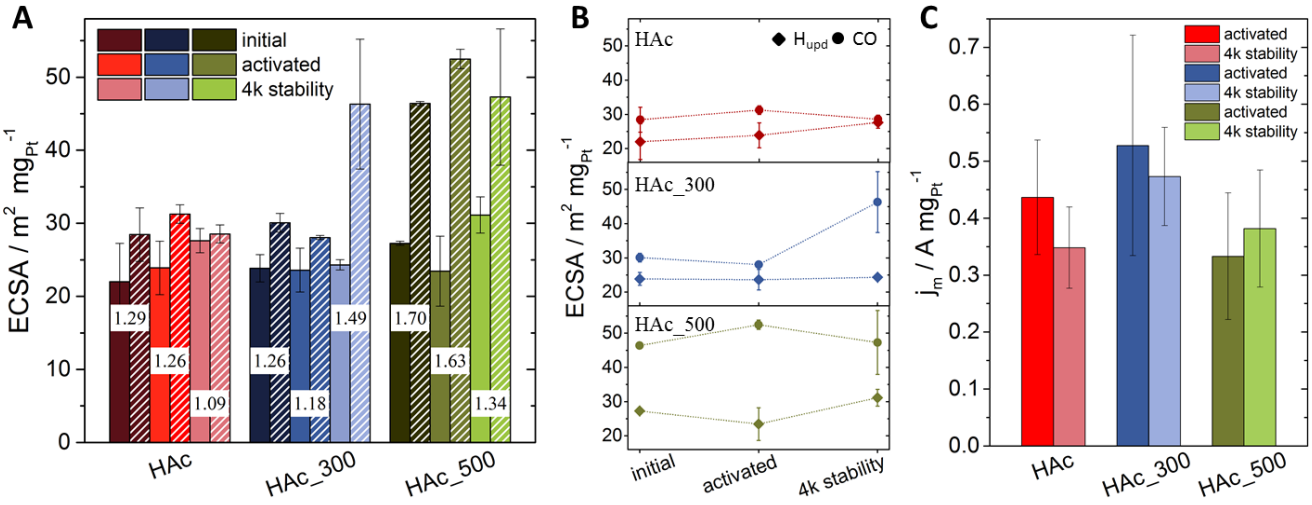

Figure 6.3 Electrochemical surface areas (ECSAs) and mass based ORR activity; **A)** ECSA based on hydrogen under potential deposition (solid bars) and on CO oxidation (striped bars) of initial materials, after electrochemical activation and 4k cycles stability test. The numbers between the bars indicate the respective $Q_{CO}/2Q_{Hupd}$ values; **B)** Evolution of ECSA values with progressive numbers of electrochemical cycles; round symbols CO ECSA, squared symbols H_{upd} ECSA, lines between the symbols should guide the eye; **C)** Mass based ORR activity after electrochemical activation and 4k cycles stability test evaluated at 0.9 V_{RHE} from LSVs measured between 0.05 and 1.0 V_{RHE} with 5 mV s^{-1} in 0.1 M $HClO_4$.

It has been reported, that the charge ratio of Hupd to CO, $Q_{CO}/2Q_{Hupd}$, may have some qualitative predictive power as to the surface / sub-surface Pt-to-Ni composition[135]. $Q_{CO}/2Q_{Hupd}$ values close to 1.0 were reported to suggest a pure Pt or Pt-rich surface, a thick Pt shell or a uniform distribution of Pt and Ni. Values closer to 1.5 suggest a Pt-skin type surface, where a Pt rich top layer is supported by a Ni-richer second atomic layer.

HAc exhibited a charge ratio value of 1.29 and likely represents a situation with a thin Pt surface shell-like structure, probably caused by the acetic acid treatment (Figure 6.3A, numbers between the bars). After activation and 4k cycles the charge ratio values decreased progressively, consistent with a thickening of the Pt shell or the formation of a more homogeneous surface alloy. The formation of a thicker Pt shell is rather likely, due to the peak developments discussed in the cyclic voltammograms obtained in N_2 protected atmosphere.

HAc_300 behaves quite differently, after activation the $Q_{CO}/2Q_{Hupd}$ value decreased from 1.26 to 1.18, but increased again after 4k cycles to 1.49. This is consistent with the notion of an initial thickening of the Pt shell, as it also have been observed for HAc. The subsequent increases, on the other hand, suggesting a more "Pt-skin" type particle surface composition, is likely caused by Ni atomic segregation into the sub-monolayer regions during annealing at 300 °C in H_2[46,73,132,147]. This advanced structure is also suggested by the additional peak occurrence in the CO stripping voltammograms and has been observed in a similar set of samples before[132].

HAc_500, finally, showed a large initial charge ratio value of 1.70 indicating a defect Ni-rich surface, in line with the weak H_{upd} features shown in Figure 6.2C. With subsequent electrochemical potential cycling, these charge ratio values decreased again due to strong Ni leaching, now creating a thick Pt-enriched surface, which also is supported by the cyclic voltammograms in N_2 atmospheres discussed above and the increase in the CO stripping peak potential.

6.2 Discussion

Figure 6.4 illustrates the experimentally observed surface and sub-surface conditions of the discussed materials based on our combined analyses of cyclic voltammograms, CO stripping voltammograms and $Q_{CO}/2Q_{Hupd}$ values.

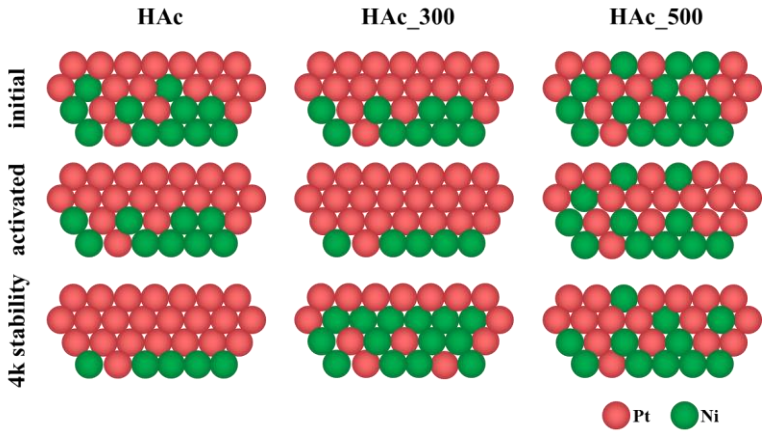

Figure 6.4 Schematic illustration of possible surface and sub-surface condition of HAc, HAc_300 and HAc_500 in their initial and activated state and after 4k stability test.

Comparing the values among the samples in the initial stages, HAc probably exhibited a pronounced Pt shell, while HAc_500 was Ni-rich in its surface. Thus, a temperature treatment significantly changes the surface composition, even of relatively Pt-rich surfaces, by creating more homogeneous surface alloys. This effect starts to emerge at temperature above 300 °C, because at the HAc_300 samples exhibits a mostly Pt enriched surface. Annealing at 300 °C under the chosen conditions seemed to have a comparable effect on the particle surface like the activated HAc as both exhibit the same $Q_{CO}/2Q_{Hupd}$ value. The initial conditions of the surfaces have a high influence on the surface changes during electrochemical cycling. HAc sample only showed a thickening of the

Pt shell with increasing number of electrochemical cycles, which was also happening to HAc_500 even though the initial state was much more Ni-rich. A thickening of the Pt shell was also happening to HAc_300 after activation, but after 4k cycles the particle surface was changing in a different way according to the additional shoulder in the CO stripping profile (Figure 6.2E) and the $Q_{CO}/2Q_{Hupd}$ values (Figure 6.3A). The presence of a Pt-skin like structure, supported by the $Q_{CO}/2Q_{Hupd}$ value of 1.49, also offers a reasonable explanation for the emergence of the additional CO profile shoulder, which was indeed reported for Pt-skin like surface in single crystals[135].

To correlate the detailed surface compositional changes with the resulting experimental oxygen reduction reaction (ORR) activities, linear sweep voltammetry in oxygen saturated electrolyte was used , and the Pt-mass based current densities were determined (Figure 6.3C). HAc_300 showed the highest ORR activity after activation and after 4k cycles stability test, with no activity drop after 4k cycles (drop is within the error). After activation HAc showed a slightly lower activity than HAc_300 and a small drop in activity after 4k stability. HAc_500, which overall showed the smallest ORR activity was stable after 4k cycles, which was likely due to the loss in octahedral shape. In general, all measured ORR activities are in the same order of magnitude. In comparison to ORR activities usually reported for octahedral Pt-Ni nanoparticles, our observed ones are rather low, possibly due to the formation of a more defect particle surface induced by leaching and annealing. Nevertheless, HAc_300 exhibits the highest ORR activity and a good electrochemical stability. Thus, annealing at 300 °C after an acetic acid treatment seems to lead to an improved surface and sub-surface condition, resulting in slightly higher ORR activities.

Other than in our previous study, annealing had a smaller impact on the resulting ORR activity and stability values when performed on acid leached samples[132]. Without a preceding acid treatment particles are much more sensitive in terms of heat treatments, but in principle the same trends were overserved.

6.3 Conclusion

To conclude, in this contribution we have investigated how an initial acid treatment preceding a thermal annealing affects the surface electrochemistry and catalytic ORR activity of shaped Pt-Ni nanoparticles. We conclude that the initial post-synthesis acid treatment generates a Pt-enriched surface on octahedral Pt-Ni nanoparticles. With subsequent annealing at 300 °C, first a more Pt enriched surface was generated before, at high temperatures of 500 °C, we observed a strong migration of Ni to the particles surface, generating a Ni-richer surface. The Pt enriched surface after annealing at 300 °C leads to improved ORR activity and a quite good time stability. Thus, it appears that the combination of acid leaching followed by annealing leads to surface compositional conditions of the shaped Pt-Ni nanoparticles beneficial for efficient and stable electrocatalytic oxygen reduction performance.

7. Real-time Imaging of Activation and Degradation of Octahedral Pt-Ni Fuel Cell Catalysts at the Nanoscale

Chapter 7 and Appendix A4 Supplementary Information to Chapter 7 are reproduce from a manuscript submitted to the Nature Publishing group.

Vera Beermann, Megan Holtz, Elliot Padgett, Jorge Ferreira de Araujo, David A. Muller, and Peter Strasser

V.B. carried out the chemical synthesis and the *ex situ* electrochemical experiments. M.E.H. performed the *ex situ* STEM experiments and *in situ* image and movie processing. M.E.H. and V.B. carried out the *in situ* STEM experiments. J.F.A. planned, performed and evaluated the DEMS experiments. All authors conceived and designed the experiments, discussed the results, drew conclusions and participated in writing the manuscript.

Octahedrally shaped Pt-Ni alloy nanoparticles have demonstrated unprecedented electrocatalytic activity for the oxygen reduction reaction (ORR), sparking interest as catalysts for low-temperature fuel cell cathodes. However, deterioration of the octahedral shape that gives the catalyst its superior activity currently prohibits the use of shaped catalysts in fuel cell devices, while the structural dynamics during degradation are largely unknown. We investigate the time-resolved degradation pathways of individual nanoparticles during cycling and start/stop conditions using an in situ STEM electrochemical liquid cell on timescale, which allows to track changes happening within seconds. Thereby dissolution and movement of the metal particles and the carbon support can be correlated precisely to the applied electrochemical potential and potential changes. We track morphological changes of the nanoparticles and their facets, monitor particle motion and coalescence at potentials that corrode carbon, and investigate the dissolution and redeposition processes of the nanocatalyst under working conditions. Carbon support motion, particle motion, and particle coalescence were observed as the main microstructural responses to potential cycling and holds in regimes where carbon corrosion happens. Catalyst surface area loss happened more severely during high potential holds and sudden potential changes than during cyclic potential sweeps, despite carbon corrosion happening during both, as suggested by ex situ DEMS results. During an extremely high potential excursion, the shaped nanoparticles became mobile on the carbon support and agglomerated facet-to-facet within 10 seconds. These experiments suggest that start/stop potential treatments may cause catalyst coarsening on a much shorter time scale than full collapse of the carbon support. Additionally, the varying degrees of attachment of particles on the carbon support indicates that there is a distribution of binding strengths. We further track the dissolution of Ni nanoparticles and determine the dissolution rate as a function of time for an individual nanoparticle – which occurs over the course of a few potential cycles for each particle. This study provides new visual understanding of the fundamental structural

dynamics of shaped nanocatalysts during fuel cell operation and highlights the need for better catalyst-support anchoring and morphology for allowing these highly active shaped catalysts become useful in PEM fuel cell applications.

In this study, we investigate the degradation of carbon-supported octahedral shaped Pt-Ni nanoparticle catalysts for advanced fuel cell cathodes. We use an *in situ* electrochemical liquid-cell and scanning transmission electron microscopy (STEM) to track individual particles under electrochemical conditions that arise or are applied at the cathode. We monitor the translational, structure-morphological, and – thanks to atomic number contrast in high angle annular dark field (HAADF) STEM – compositional dynamics and evolution of individual nanoparticles as well as ensembles of nanoparticles in real time and with nanometer-scale resolution and support findings regarding carbon corrosion with DEMS. This study gives new insight of how initially shape-controlled nano-octahedra transform into unshaped and partially agglomerated particle clusters, and provides visualization of how the degradation of the carbon support affects the catalyst material.

7.1 Results and Discussion

We investigated ~8 nm octahedral Pt-Ni nanoparticles that were supported on Vulcan carbon supports (Figure 7.1a). These supported Pt-Ni/C nanooctahedra showed electrochemical ORR activity that was about 25x greater than commercial Pt/C, and, from a more practical perspective, were large enough to be imaged in an *in situ* TEM liquid environment at low beam doses. They exhibit an average composition of $Pt_{69}Ni_{i31}$, a Pt enriched surface and were carefully washed with ethanol in order reduce remove remaining surfactants from the synthesis[132]. In addition to octahedral Pt-Ni nanoparticles, the catalyst also contained a minor alloy phase consisting of 20-30 nm Ni-rich particles, which enabled study of rapid electrochemical dissolution processes of undesired alloy phases during catalyst activation[132]. These Ni-rich particles consist of a Pt-rich core which is encased by a thick Ni shell resulting in an overall composition of Pt_5Ni_{95}. Figure 7.1a shows the catalyst particles *ex situ* as synthesized: the initial octahedral shape is evident from the faceting of the particles, which are homogeneously distributed on the carbon support. After *ex situ* voltammetric stability tests in perchloric acid, the octahedral particles lost their sharp faceting and showed agglomeration (shown in Figure 7.1b). The particles display slightly concave edges and facets suggesting that the facets are relatively Ni-rich and are therefore etched more quickly during acid and electrochemical treatment, leaving behind a Pt-rich skin. After treatment, we observe an average composition of $Pt_{69}Ni_{31}$, reflecting the relative loss of Ni[132]. To better understand this degradation, we perform an *in situ* study of the real time nanometer-scale evolution of the octahedral fuel cell catalysts.

The *in situ* TEM experiments were carried out in a Protochips Poseidon holder and a flow cell chip equipped with a silicon nitride window. The cross section and top view of the chip are illustrated in Figure 7.1c showing

the carbon working electrode and the Pt reference and counter electrode[83,94]. The platinum reference electrode was calibrated in 0.1 M perchloric acid using the well-known characteristics of the hydrogen underpotential deposition region of platinum-based materials, as shown in Figure 7.1d. With that, 0.0 V_{RHE} was correlated to -0.8 V_{Pt}. All further potentials are reported against the reversible hydrogen electrode (RHE) based on this calibration to allow better comparability to literature. The cell had a liquid thickness of 300 nm, estimated by electron energy loss spectroscopy[117].

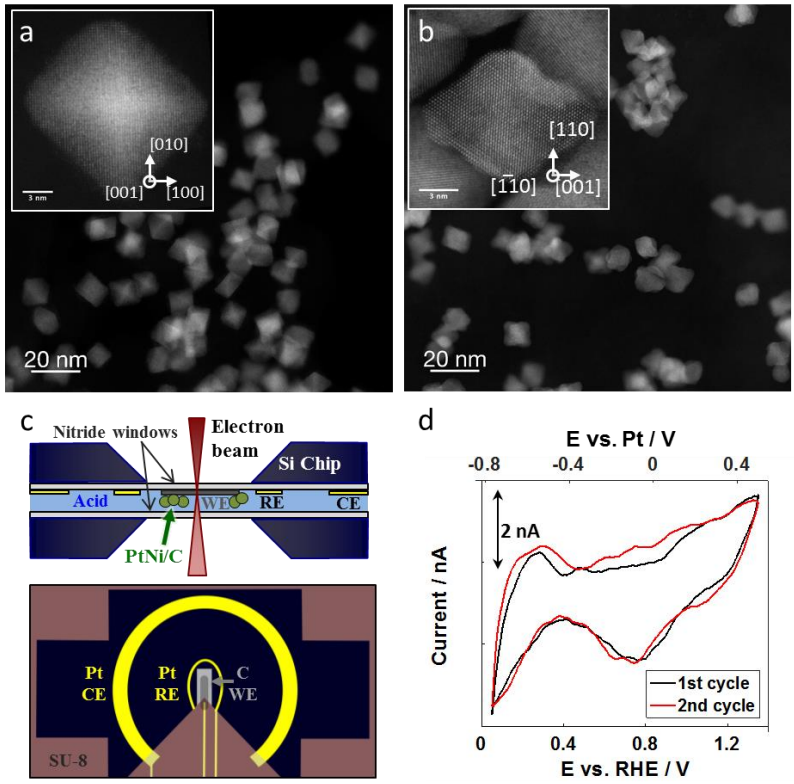

Figure 7.1 Preliminary characterization and *in situ* TEM chip design. a) Particles *ex situ* before cycling, showing octahedral shape with strong faceting in the {111} planes and **b)** *ex situ* after electrochemical treatment similar to the *in situ* experiment, where facets are curved and particles are agglomerated. **c)** Overview of electrochemical cell setup, with cross section of liquid cell holder on top and view of electrodes on the bottom. **d)** Cyclic voltammogram of Pt-Ni nanoparticles on the carbon working electrode inside the electrochemical cell in 0.1 M $HClO_4$ with a sweep rate of 100 mV s^{-1}.

Prior to the *in situ* TEM electrochemical investigations, we identified a suitable beam dose that did not visibly affect the octahedral particles in the electrolyte for the duration of the applied electrode potential. Even though the beam alone may not influence the particles, the combination of beam and electrochemical cycling may have an effect. To account for this, we compared the final state (after electrode potential cycling) of particles that were imaged during the *in situ* experiment to other particles that were not continuously imaged in the electrochemical cell, to crosscheck for similar transformations. We further compared particles that were on the electrode to those that were not on the electrode to ensure that the effects were electrochemical rather than chemical inside the liquid cell (Figure S4.1). As a final check, we qualitatively compared the data from *in situ* experiments to that of *ex situ* experiments. Overall, we found that the electrochemical effects observed were

neither artefacts from the electron beam, nor from the chemical environment in the cell. However, the *in situ* experiments appeared to be harsher on the particles due to the additional effects of the electron beam.

We performed *in situ* electrochemical STEM investigations using different electrochemical electrode potential cycling protocols, resembling those routinely applied to single fuel cells to electrochemically activate and stress-test their catalysts[148,149], cycle in standard operating ranges, and cycle under extreme potentials to simulate start/stop conditions.

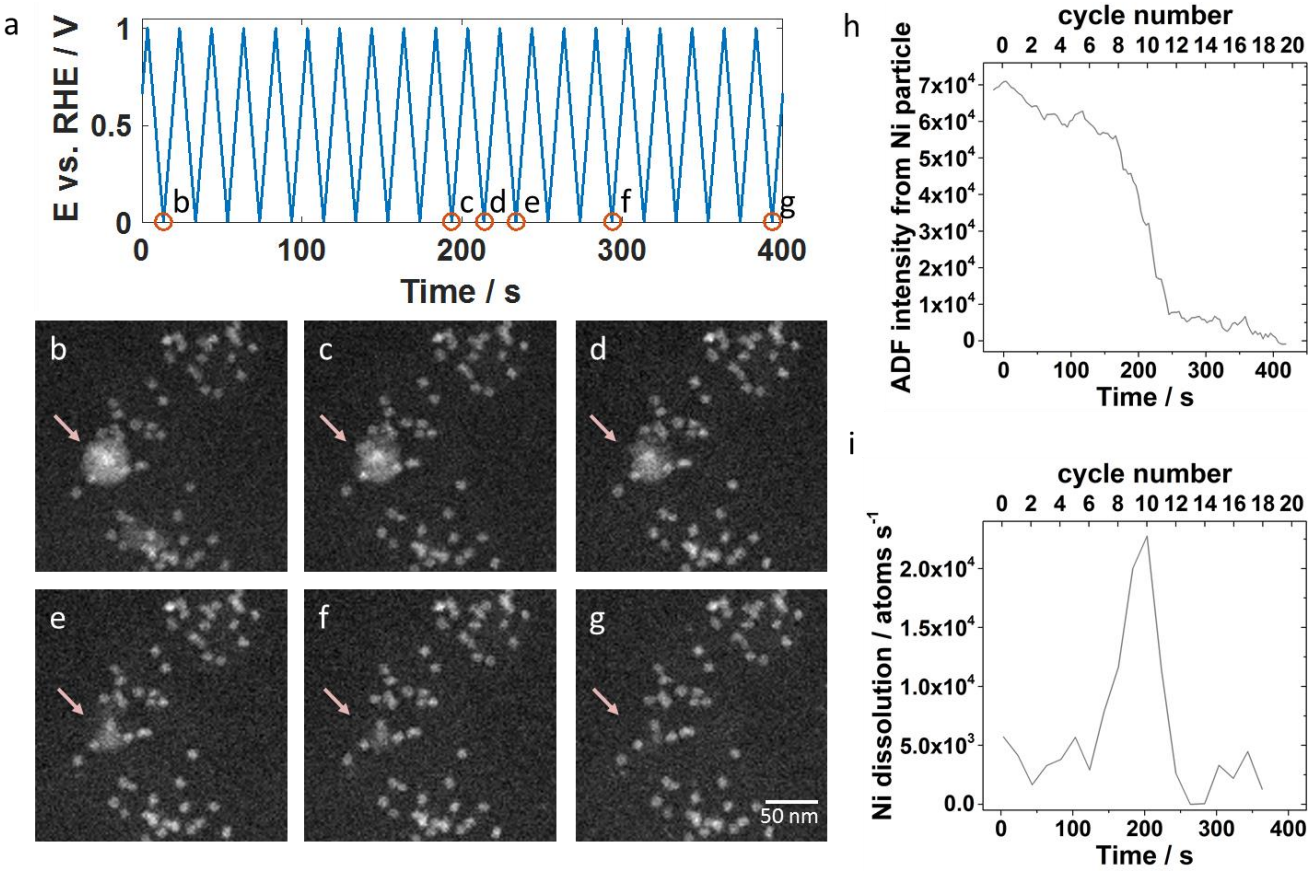

Figure 7.2 HAADF STEM *in situ* imaging of the catalyst structure during electrochemical potential cycling between 0.0 and +1.0 V_{RHE} in 0.1 M $HClO_4$ for 20 CV with 100 mV s^{-1} sweep rate. a) Potential profile over time with marked points corresponding to the images in **b-g)**. A Ni-rich particle marked by the arrow disappears during cycling, first becoming less dense, then spongy, finally dissolving completely. **h)** ADF intensities of the Ni-rich particles over time during potential cycling and **i** the resulting Ni dissolution rate.

First, the octahedral nanoparticles were cycled 20 times inside a potential range between 0.0 and +1.0 V_{RHE} with 100 mV s^{-1} to mimic an activation procedure. Figure 7.2a shows the applied potential profile with selected marked time points corresponding to the STEM images shown in Figure 7.2b-g. The selected field of view displays a collection of octahedral nanoparticles surrounding a larger Ni rich particle. During the electrochemical treatment, there were no discernible changes in the octahedral particle structure. However, the large Ni-rich particle marked by the arrow in Figure 7.2b-g gradually dissolved according to $Ni^0 \rightarrow Ni^{2+} + 2e^-$ (E^0=-0.26 V[131])

during the applied potential cycling. After 10 cycles (Figure 7.2c) the particle started to lose mass (observed by a change in diameter and in the overall HAADF intensity) and after 15 cycles (Figure 7.2f) only a small fraction remained. The dissolution process took place over several potential cycles: first it became less dense, then appeared sponge-like and porous, and finally it disappeared completely. The dissolved Ni-rich particle left behind an octahedral particle, which may have been contained inside the Ni-rich phase, evidenced by the bright contrast in the center (see Figure 7.2b). The dissolution of another Ni-rich particle was observed between Figure 7.2b (where it is a fractional particle already) and Figure 7.2c in the central lower part of the frame. After the first 20 cycles, there were still Ni-rich particles remaining in areas outside of the region imaged in Figure 7.2, and after an additional 20 cycles (total of 40 cycles), the remaining Ni-rich particles elsewhere on the electrode also disappeared. The real-time imaging of the catalyst during electrochemical cycling with the animated potential profile corresponding to the data in Figure 7.2b-g is shown in Movie S1 of the supplementary material.

The opportunity to image the Ni dissolution process in real time allows us to estimate an average dissolution rate. Annular dark field (ADF) intensities of the Ni particle were obtained by integrating over a region containing the Ni particle, subtracting off the background intensity from a neighboring region to account for liquid thickness variation, and subtracting off the average intensity of the last 5 frames, when the Ni particle had fully disappeared. In Figure 7.2h, we first see a gradual decrease in ADF intensity, which corresponds in the image to the particle becoming less dense, then spongy. Then, the particle dissolves rapidly, decreasing in size drastically between cycle 9 and 13. From the background subtracted ADF intensity of the Ni-rich particle, we can calculate its dissolution rate because the ADF intensity is proportional to the mass present. We assume that the initial ADF intensity corresponds to the number of nickel atoms in a solid, spherical shell of nickel that has the inner and outer diameters as measured in the ADF image. The derivative of the ADF intensity which is scaled to number of Ni atoms present then gives the dissolution rate in atoms/s. This dissolution rate, plotted in Figure 7.2i, reaches values of around 10,000 to 30,000 atoms per second during cycles 9 through 13. Assuming a perfectly round Ni particle with a diameter of 10 nm, the number of initial particle surface atoms would be around 4500 Ni atoms. Thus, a dissolution rate of 1000 atoms/s corresponds to one monolayer every 4.5 seconds (for this 10 nm diameter particle). Assuming it is etching along the 111 direction of Ni which has a 2 Å spacing, that corresponds to an etching rate of about 27 nm/min – whereas typical etch rates for bulk Ni-materials are on the order of 10 nm/min[150]. So, for a nanoparticle system where the geometry, chemistry and local potential can be quite different, we believe this is a reasonable etch rate for Ni.

After the peak in dissolution, the remaining amount of Ni-rich particle that remains slowly dissolves away – perhaps due to low surface area or Pt enrichment as Ni is selectively removed. This is the first quantitative observation of the nanometer-scale reaction dynamics of a selective Ni dissolution process during the disappearance of Ni-rich alloy particle.

To compare the activation processes during the *in situ* experiments and corresponding *ex situ* treatments, *ex situ* experiments in a conventional three-electrode cell set up were carried out using identical protocols (Figure S4.2). The observed cyclic voltammetry current in the *in situ* cell may differ from an *ex situ* experiment for several reasons, including the small area of the working electrode, the electrolyte that has not been degassed, and the different diffusion geometry in the thin encapsulated cell. Nevertheless, some trends in the *in situ* cyclic voltammograms are noteworthy as they are showing the same processes as observed in the STEM images (Figure S4.2b). With increasing cycle number, the current at higher potentials due to Ni dissolution trails off, and the redox waves inside the H_{upd} region become sharper, which is consistent with generating a cleaner, Pt-richer, and more facetted surface due to Ni dissolution and Pt diffusion[28,63,129,132]. Unlike *in situ*, we noticed several residual large Ni-rich nanoparticles after 40 *ex situ* cycles (Figure S4.2d,e). Thus, we conclude that the *in situ* conditions were more corrosive than the *ex situ* conditions, possibly due to the confined liquid cell environment and electron beam effects, as well as the lower geometric Pt loading.

Our observations show that the typical electrochemical activation comprised of cyclic voltammetry in liquid does not harm the shape or distribution of the Pt-Ni octahedra, validating the suitability of these commonly used activation procedures. Dissolution of nickel in the Pt-Ni octahedra was not possible to determine at the dose-limited resolution, because the particles are small and the ADF intensity is largely dominated by the large Pt signal, so would not pick up the small change due to Ni dissolution. While the Pt-Ni octahedra are stable, the undesired Ni-rich clusters dissolve within minutes of the activation protocol. In all, this is the first time that the activation dynamics of a shaped Pt alloy fuel cell catalyst by electrochemical dealloying and selective corrosion has been imaged in real time.

Next, we studied the impact of sequential sets of potential cycles separated by periods with constant applied electrode potential, a frequently used test cycle motif for automotive or stationary PEM fuel cells. The potential *versus* time profile is given in Figure 7.3a, again with marked time points for the snapshots shown in Figure 7.3b-h. An initial potential hold at +0.8 V_{RHE} is followed by cyclic voltammetry with an upper potential of +1.2 V_{RHE} with 100 mV s^{-1} sweep rate. Then, there is a subsequent fixed potential hold at +1.2 V_{RHE}, followed by cyclic voltammetry to an upper potential of +1.4 V_{RHE} at 100 mV s^{-1}. This is finished with another fixed potential hold at +1.4 V_{RHE}. For this experiment, we imaged a region of the octahedral Pt-Ni nanoparticles that was previously not immersed in electrolyte, and did not show evidence of previous cycling. This was possible because the liquid cell was only partly full, and as we flowed in liquid over the course of the experiment, the liquid front gradually moved from one side to the other to cover the entire electrode region.

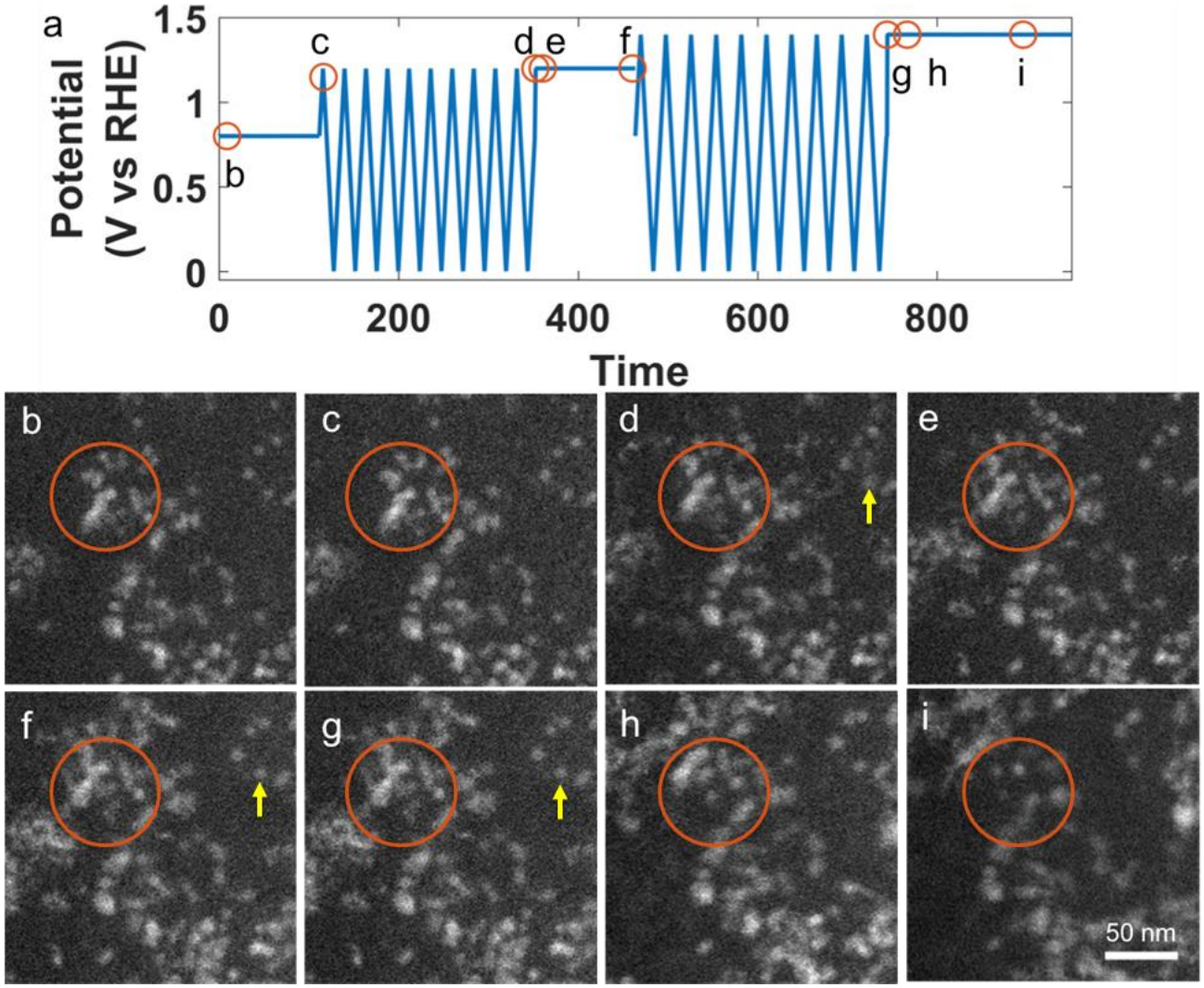

Figure 7.3 HAADF STEM *in situ* imaging of the impact on the catalyst structure of an electrochemical sequence consisting of electrochemical potential cycling between 0.0 to +1.2 V_{RHE} and 0.0 to +1.4 V_{RHE} for 10 CV with 100 mV s^{-1} and holding on different upper potentials in 0.1 M $HClO_4$. a) Potential profile over time with marked points for shown images. **b-i)** Images taken at the marked potential and cycle number.

Still images in Figure 7.3b-h are taken from the *in situ* STEM data that is presented in Movie S2, which also incorporates the animated potential profile. During the hold at +0.8 V_{RHE} carbon remained stable and we saw no changes in catalyst structure (Figure 7.3c). When cycling to +1.2 V_{RHE}, a slight movement of the carbon support was observed, visible by the motion of whole particle agglomerates. We also observed the nucleation and growth of stringy, new Pt-rich deposits, which is likely due to chemical metal redeposition as we will discuss in the following paragraph (Figure 7.3d,f,g, yellow arrow). During the hold at +1.2 V_{RHE} the redeposited Pt/Ni abruptly moves, as if it was not firmly attached and became dislodged when held at elevated potential (Figure 7.3e, orange circle). When the Pt-rich redeposits appear to collide with other parts of the sample or working electrode, their motion slows or stops. At the same time, the former octahedral Pt-Ni nanoparticles started to grow slowly in size (Figure 7.3f, orange cycle), as expected from both electrochemical and beam-induced redeposition. Upon

cycling to +1.4 V_{RHE}, the redeposited Pt/Ni again becomes mobile and swings about, while carbon-supported Pt-Ni particles also move notably. Additional stringy Pt-rich deposits form. Finally, holding the potential at +1.4 V_{RHE} again causes abrupt motion of the redeposited Pt (Figure 7.3h, orange cycle), while carbon corrosion ($C + 4H_2O \rightarrow CO_2 + 4H^+ + 4e^-$ (E^0=0.21 V)[131]) appears to occur rapidly enough to cause sustained motions of the carbon-supported Pt-Ni particles (Figure 7.3i) and Pt-Ni particle growth continues.

Several phenomena were observed in Movie S2 – including growth and motion of stringy Pt-rich deposits, Pt-Ni nanoparticle growth, and Pt catalyst structure changes which are likely due to carbon corrosion –which we will discuss in the following paragraphs.

There are two potential causes of the observed stringy Pt/Ni redeposition: (1) chemical redeposition, which is driven by a reducing chemical environment in the cell such as one generated by the electron beam[151], or (2) electrochemical reduction, which occurs at low, reducing potentials only at locations which have electrical contact with the working electrode. Compared to Ni, Pt gets reduced preferentially due to its higher standard potential, and the in the STEM images is consistent with a Pt or Pt-rich composite. Ni dissolves to a larger extent than Pt, because of its lower standard potential. Pt deposits are more reasonable, because Ni is probably already dissolved at these relatively high potentials. From literature we know, that Ni is unlikely to become reduced again on the particle surface[28]. We observe that these Pt-rich deposits form faster during cyclic voltammetry than during potential holds. There may be two reasonable explanations for this: 1) electrochemically assisted deposition might occur during the sweep to low potentials, or 2) the Pt is chemically deposited, and happens faster during the cyclic voltammetry because of increased Pt and Ni dissolution during the cyclic voltammetry, so there is more Pt and Ni in solution to be chemically deposited ($Pt^0 \leftrightarrow Pt^{2+} + 2e^-$ (E^0=1.18 V) and $Ni^0 \leftrightarrow Ni^{2+} + 2e^-$)[131]. Because the deposition appears to be faster at the cyclic voltammetry with upper potentials of 1.4 V_{RHE} compared to 1.2 V_{RHE}, it is more likely that redeposition is chemically driven. This is because the time spent at lower potential is the same, meaning the electrochemical deposition would be expected to be similar, but there is more time spent at higher potentials, and accordingly more Pt will be dissolved. We thus conclude that we observe chemical Pt and Ni redeposition that is driven by the reducing effects of the electron beam, which is similar to the formation of so-called pure Pt deposits (referred to as “Pt bands”) reduced by dissolved hydrogen inside fuel cell membranes[152]. Unlike in a fuel cell, however, the chemically redeposited metal in this experiment is not embedded in a polymer matrix and has a different reduction process, and is therefore highly mobile and morphologically different from fuel cell Pt bands.

We observed the most severe and sudden changes to the catalyst structure precisely at the transitions from the voltammetric cycling to the potentiostatic holds with chronoamperometric monitoring of the current density. The lightly attached, stringy Pt-rich deposits become loose, very mobile and detached from the catalyst support when carbon corrosion at high potentials starts to occur. They appear to move until they collide with another feature in the catalyst structure. Furthermore, the particle motion and coalescence was correlated with the applied

electrode potential during both cyclings and holds, corroborating the detrimental effect of the anodic upper potentials. Thus, our *in situ* STEM studies evidenced how strongly platinum and nickel oxidation and dissolution accelerated at the atomic scale with increasing upper turning potentials as predicted by the mean-field Butler-Volmer relation[153-155].

In addition to the stringy Pt/Ni formation, we also observe the initial Pt-Ni octahedral particles grow over the course of the treatment. During the potential holds at high electrode potentials, catalyst particles continued to grow and lose their shape. This may be due to the formation of Pt-rich deposition by the electron beam.

Carbon corrosion is expected to become significant at potentials of +1.1 V_{RHE} and higher ($C + 4H_2O \rightarrow CO_2 + 4H^+ + 4e^-$ (E^0=0.21 V)[131])[156-158]. At these high potentials (around 1.2 V_{RHE}), we observe two types of PtNi nanoparticle motion (Movie S2). One is that we see carbon support motion and crumpling, which may be an effect of carbon corrosion, where the catalyst nanoparticles in one region of the carbon support appear to move together as the carbon bends. The second effect is that the corrosion appears to weaken the attachment of particles on the carbon support, causing additional particle migration, coalescence and agglomeration. Both of these effects were more severe at higher potentials. We found that holding at higher potentials as opposed to potential cycling intensified and accelerated particle catalyst degradation. With the help of DEMS, we note that carbon corrosion should happen both during the cyclic sweeps to high potential, as well as during the potential holds (see Figure S4.5 with corresponding text). Even though corrosion is happening throughout, the high potential hold is more detrimental to the overall catalyst morphology.

Upon comparison of *ex situ* and *in situ* conditions, the *ex situ* conditions again were less harmful to the catalyst structure than the *in situ* ones (see Figure S4.3). After *ex situ* cycling up to +1.2 V_{RHE} the octahedral particle shape was still clearly discernible, while edges and the corners were degraded after cycling to +1.4 V_{RHE}. While the general trends were consistent, the impact of the applied electrode potential on the shape, particle distribution and carbon corrosion was evidently less pronounced under the *ex situ* conditions, which is reasonable due to the absence of electron beam driven processes.

Finally, we imaged the structural evolution of octahedral Pt-Ni fuel cell catalysts under conditions simulating startup/shutdown and air or fuel starvation, which often cause uncontrolled potential steps in cathodic or anodic directions[159,160]. To achieve that, we first applied 10 potential cycles to an elevated upper potential of +1.2 V_{RHE} after which the electrode potential experienced a potential step to above +1.4 V_{RHE}. The Pt-Ni nanoparticles in this experiment had only undergone the activation profile corresponding to Figure 7.2. During the 10 potential cycles to +1.2 V_{RHE} the octahedral shape of most particles appears largely unaffected, but a few experienced

coalescence with close neighboring particles (Figure 7.4b-d, pink arrow) or small motions on the support (Figure 7.4b-d, yellow arrow). Considering that the upper potential lies outside the window where carbon is kinetically stable, the motion and coalescence may be due to carbon support corrosion.

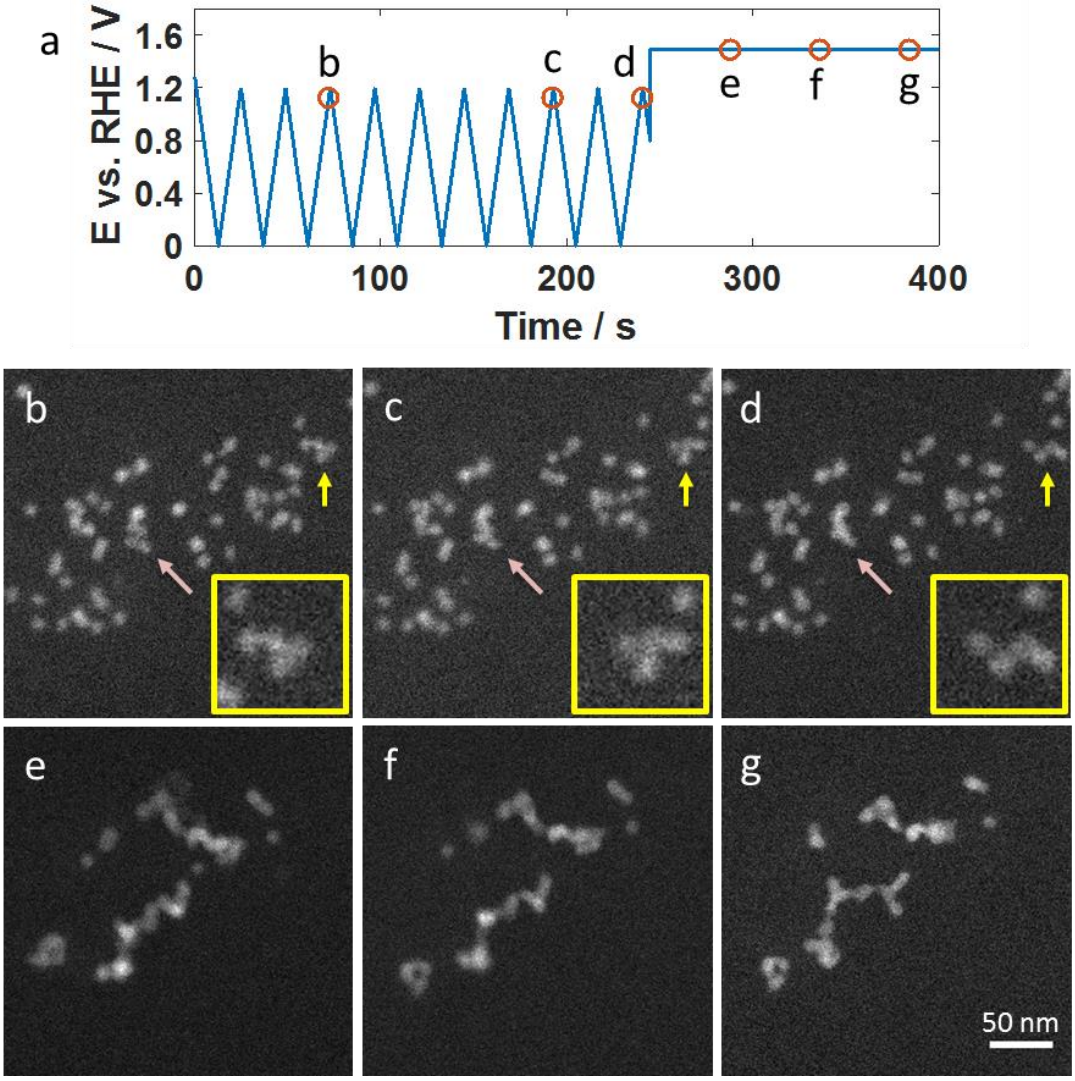

Figure 7.4 HAADF STEM *in situ* imaging of the catalyst structure during electrochemical potential cycling between 0.0 and +1.2 V_{RHE} for 20 CV with 100 mV s^{-1} sweep rate, followed by a step into a high potential. a) Potential profile over time with marked points corresponding to the images in **b-g**. Some changes to catalyst particles are noted during cycling in **b-d)** – for example, coalescence as indicated by the pink arrow and particle motion as indicated by the yellow arrow **e-g)**. After cycling, going to a high potential, we see dramatic coalescence, where the Pt-Ni nanoparticles agglomerate into wires. Inset in **a-c** shows enlarged fraction of particles aligning on their facets.

The final anodic potential step dramatically affected the global catalyst structure (Figure 7.4e-g) and would have catastrophic consequences for the fuel cell performance. The particles became highly mobile on the carbon support, as shown in the images in Figure 7.4 and Movie S3, with the majority of particles colliding on the timescale of seconds into an agglomerate with a long, branching geometry. Often, the particles appear to line up in preferred orientations – often with their edges flush – forming in straight lines or with regular angles. This suggests that they are aligning along their {111} crystal facets before fusing together (see inset Figure 7.4a-c).

We observe similar agglomeration in neighboring regions on the electrode outside the field of view, as shown in Figure S4.3, showing this occurred independent of beam effects. After a catastrophic, abrupt agglomeration, the catalyst particles continued to move on the carbon surface as carbon corrosion continues.

The corresponding *ex situ* images acquired after the same electrochemical treatment confirm the observed trends (see Figure S4.4). Although individual particles still appeared to be octahedrally shaped they agglomerated at their crystal facets. From the *in situ* magnification in Figure 7.4, it is difficult to unambiguously identify the remaining particles as octahedral or unshaped, due to the low beam dose which is required to avoid radiation damage. All data of Figure 7.4 can be inspected in Movie S3.

We should additionally note that the octahedral Pt-Ni particles were dispersed onto the carbon support as entire particle ensembles, that is, after their synthesis, rather than grown directly onto it, which likely resulted in weaker interactions between particles and support compared Pt/carbon catalysts synthesized with impregnation methods, where a Pt molecular precursor is reduced on the carbon in a dispersed state. Further studies will investigate the particle mobility as a function of different particle attachment methods. Previous *in situ* TEM investigations of Pt-Co nanoparticles grown onto the support by impregnation methods found less particle migration despite extreme carbon corrosion at high potentials[161]. Additionally, this experiment was done in liquid (without the presence of ionomer or membrane) and the presence of ionomer may alter the effects of carbon corrosion. This experiment demonstrates the importance of designing a catalyst materials with (1) particles strongly anchored to the support matrix and (2) a support material which is stable at potential above 1.4 V_{RHE}.

Our findings provide a first-of-its-kind real-time visual demonstration of the catastrophic effects of uncontrolled fuel cell cathode potential excursions to values of startup/shutdown. Our results further underline the critical importance of a strict continuous upper electrode potential control. Two distinct mechanisms could contribute to the rapid coalescence at high potential: first, the instantaneous formation of Pt and Ni surface oxides induced by the abrupt anodic potential step may have lowered the particle attachment and caused enhanced mobility; more likely, however, supported by DEMS experiments, is the mechanism involving sudden corrosion and removal of the carbon support leaving Pt-Ni particles unanchored and causing strongly enhanced particle movement by surface and bulk diffusion until the detached particles have found neighboring particles to agglomerate with (Figure S4.5).

7.2 Conclusion

We have presented STEM imaging of fuel cell catalyst activation and degradation processes in an *in situ* electrochemical cell supported by DEMS measurements. We investigated high activity octahedral Pt-Ni nanoparticle fuel cell catalysts[132]. Our *in situ* studies have revealed new insights into remaining key issues of low temperature fuel cell catalysts including a more detailed understanding of the degradation of octahedral PtNi alloy catalysts such as as carbon support corrosion, selective dissolution of non-noble metals, catalyst particle shape degradation, and particle coarsening by coalescence and Pt redeposition. The following issues were addressed: (1) Degradation processes were imaged on a time scale which allowed us to track changes happening within a few seconds (e.g. rapid and sudden changes when stepping into the constant potential and subsequent stationary agglomerated state of the particles). (2) Agglomeration along octahedral {111} facets during anodic potential steps as a result of lined up particles during potential cycling. (3) Major corrosion of the carbon support was happening during anodic stepping, not during potential cycling. It is not possible to resolve these differences in *ex situ* experiments. (4) By tracking the dissolution of individual Ni nanoparticles we were able to determine atomic dissolution rates as a function of time and potential cycle numbers which could provide guidelines for an optimized voltammetric activation protocol of fuel cell catalysts. To the best of our knowledge this is the first such *in situ* electrochemical liquid cell TEM experiment for shaped fuel cell cathode materials.

In more detail: during catalyst activation, we observed the nanometer-scale reaction dynamics of a selective Ni dissolution process, observing the Ni-rich particles become spongy before fully dissolving. The Ni dissolution process does not take place constantly but rather promptly after some electrochemical cycles. We observe that octahedral Pt-Ni alloy catalyst remained morphologically stable during moderate potential cycling up to +1.0 V_{RHE}, while cycling to and holding at 1.2 V_{RHE} and 1.4 V_{RHE} caused increasingly severe coarsening. During cyclic voltammetry to high potentials, we observed the electron beam reduction of stringy deposits similar to Pt bands caused by hydrogen cross-over in membrane electrode assemblies. At high potential holds, Pt redeposition quickly obscures the octahedral shape. Changes between potential cycling and holds cause most severe changes in the catalyst structure. Additionally, carbon corrosion was observed to increase particle migration and coalescence, with Pt-Ni nanoparticles appearing to typically coalesce on their {111} facets.

This study dramatically visualizes the dynamics of fuel cell catalyst activation and degradation at the nanometer scale. From these results we develop a better understanding of detrimental nanoscale effects which occur under different fuel cell conditions.

8. Summary and Perspective

Platinum-based octahedral shaped nanoparticles have attracted increasing attention in the last years due to their remarkably high ORR activity, which makes them promising cathode fuel cell catalysts with great potential for future fuel cell applications. However, some issues such as shape-/performance stability and detailed understanding of structure-activity relationships need to be addressed in order to establish new and innovative roadmaps for the design of stable and reliable future fuel cell catalysts. This work presented novel and valuable approaches to overcome some of these remaining challenges for Pt-Ni based catalysts, which are summarized in Figure 8.1.

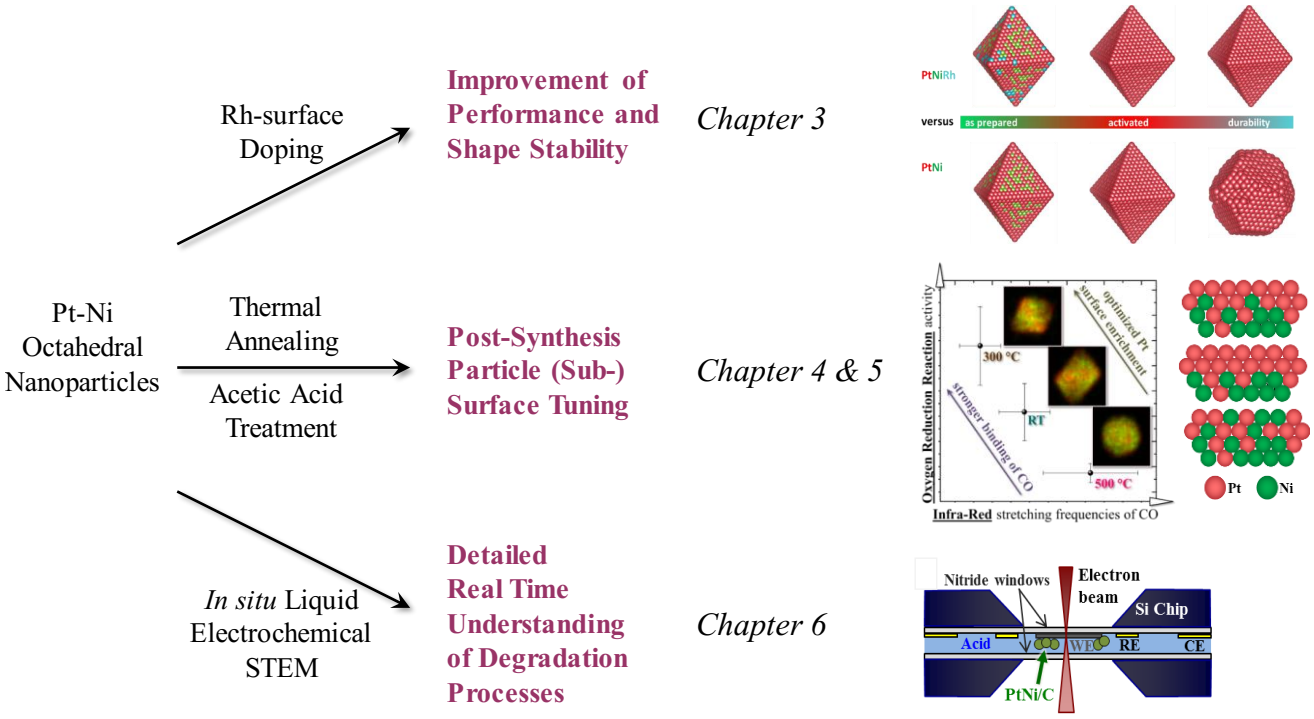

Figure 8.1 Graphical summary of topics and issues discussed and investigated in this work, including improvement in stability, post-synthesis treatments, and sophisticated *in situ* liquid electrochemical STEM to gain detailed real time insights into degradation processes[63,132,146]. (Reprinted with permission from The American Chemical Society and The Electrochemical Society)

Synthesis of the Investigated Pt-Ni Octahedral Nanopartilces

A wet chemical synthesis approach using OAm and OAc as organic surfactants to control nanoparticle size and $W(CO)_6$ as reducing and capping agent allowed the dedicated and reliable preparation of monodisperse Pt-Ni octahedral nanoparticles and the flexible addition of a third metal. All materials discussed in this work show reasonable ORR activities, which outperform the commercial Pt/C catalysts.

Improvement of Performance and Shape Stability

The issue of limited long-term stability of these particles was carefully investigated in detail in Chapter 4. Rh-surface-doped octahedral Pt-Ni nanoparticles were prepared comprising different Rh-contents. At about 3 at.%

Rh the particles exhibit high ORR activities of up to 1.14 A mg_{Pt}^{-1} combined with an improved performance and shape stability after 30,000 potential cycles in a stability test. In comparison, the un-doped reference material showed a loss in octahedral shape and performance already after 8,000 potential cycles. STEM and EDX analysis were used in order to obtain detailed atomic insights into these phenomena. From that it was concluded, that not only the dissolving Ni is responsible for shape and performance losses, but more likely the migration of Pt atoms within the particles cause the loss of anisotropy and, therefore, the most active structure. This study has shown, that surface doping with a third metal, e.g. Rh, is an effective way to suppress Pt migration during dynamic potential cycling, which highly enhances ORR long term performances.

Post-synthesis Particle (Sub-)Surface Tuning

A systematic study of the influence of annealing as a post synthesis treatment was presented in Chapter 5, dealing with the effect of temperature treatment on the nanoparticle surface and sub-surface. A systematic and detailed investigation of resulting surface properties and ORR activities was presented. Annealing causes Pt migration within the particle and simultaneously generates a clean particle surface by removing organic molecules remaining from the synthesis. Using *in situ* heating TEM and XRD morphological and structural changes were analyzed as a function of temperature. Higher temperatures harm the octahedral shape of the nanoparticles and result in more homogeneous alloy structures as could shown by STEM EDX analysis. *In situ* electrochemical FTIR experiments, using CO as a probe molecule suggested an optimized degree of Pt surface enrichment for the sample annealed at 300 °C, showing an ORR activity ~25 times higher than the one of commercial Pt/C and ~1.5 time higher than the un-annealed Pt-Ni/C. A similar effect for particles with a Pt rich shell, generated by an acetic acid treatment as presented in Chapter 6 was observed. After acid leaching and annealing, the resulting ORR activity trends were comparable to the only annealed ones. Accordingly, surface–doping and –tuning both influence the Pt migration behavior within the Pt-Ni octahedral particles during electrochemical cycling or during post synthesis treatments and set new guidelines for efficient nanoparticle design. The studies from Chapter 5 and 6 aid the general understanding of effects and benefits of post-synthesis treatments, establish structure-activity relationships, and suggest suitable strategies to design improved Pt-Ni octahedral ORR catalysts.

Detailed Real Time Understanding of Degradation Processes

Pt-Ni/C octahedral nanoparticles were studied using *in situ* liquid STEM, revealing new insights into remaining key issues in understanding catalyst degradation. Chapter 7 presented an imaging technique that allows the observation of nanoparticles on a second based time scale. For the first time Ni-dissolution was imaged and quantitatively determined which is fundamental for all Pt-transition metal alloys. Besides morphological changes, particle motion and coalescence were detected as a function of applied potential, which was promoted by carbon support motion and corrosion at potentials higher than 1.0 V_{RHE}. Using DEMS experiments, carbon support corrosion was additionally verified by following the potential dependent CO_2 signal. Most severe

changes were observed within the transition from cyclic voltammetry to constant potential hold, mimicking start-/stop phenomena of a fuel cell device. After holding at extreme high potential nanoparticles agglomerated along their facets. This part of the present work provides new visual insights into fundamental understanding of structural dynamics and highlights the importance of suitable support-catalyst anchoring.

Perspective

The new insights from this work lead to a better understanding of Pt-Ni/C octahedral catalysts for ORR and offer new guidelines for active and stable electrocatalysts, which will help to design future materials. However, further investigations and deeper understanding of the system is still necessary.

Besides atomic-scale structural and compositional analysis, the durability of these materials needs to be further improved. Detailed correlations between catalyst microstructures and its performances are of fundamental importance to design new materials. Therefore, understanding of nanoparticle growth is essential in order to fine-tune the particle characteristics in terms of their size, shape, surface, and bulk compositions properties. State of the art *ex situ* and *in situ* (S)TEM microscopy are powerful tools for such investigations. Based on the work of the group of Huang[50], various doping metals, along with their location within the octahedral particles, surface-, near-surface, or bulk-doping, should be tested. Therein, the effect of the doping metal and its position on ORR performance and durability should be investigated in detail. Advanced (*in situ*) electron microscopic investigations of the growth mechanism and the degradation mechanism would provide further insights into the particle characteristics, offering great potential to prepare sophisticated materials for future ORR catalysts and efficient, cost effective and reliable fuel cell technologies. As a final step these materials should be investigated in MEAs to explore their performance and durability in a real application, as especially Pt-alloy nanoparticles often show different characteristic in MEA devices in comparison to RDE experiments[162].

9. References

1 https://www.ogj.com/articles/2017/01/bp-energy-outlook-global-energy-demand-to-grow-30-to-2035.html. (August 15, 2018).
2 Pellow, M. A., Emmott, C. J. M., Barnhart, C. J. & Benson, S. M. Hydrogen or batteries for grid storage? A net energy analysis. *Energy & Environmental Science* **8**, 1938-1952 (2015).
3 https://www.energy-charts.de/power_de.htm?source=all-sources&year=2018&week=28. (August 15, 2018).
4 Beaudin, M., Zareipour, H., Schellenberglabe, A. & Rosehart, W. Energy storage for mitigating the variability of renewable electricity sources: An updated review. *Energy for Sustainable Development* **14**, 302-314 (2010).
5 Niaz, S., Manzoor, T. & Pandith, A. H. Hydrogen storage: Materials, methods and perspectives. *Renewable and Sustainable Energy Reviews* **50**, 457-469 (2015).
6 Barton, J. P. & Infield, D. G. Energy Storage and its Use with Intermittent Renewable Energy. *IEEE transactions on energy conversion* (2004).
7 http://energystorage.org/energy-storage/technologies/hydrogen-energy-storage. (August 14, 2018).
8 Smith, W. The role of fuel cells in energy storage. *Journal of Power Sources* **86**, 74-83 (2000).
9 Offer, G. J., Howey, D., Contestabile, M., Clague, R. & Brandon, N. P. Comparative analysis of battery electric, hydrogen fuel cell and hybrid vehicles in a future sustainable road transport system. *Energy Policy* **38**, 24-29 (2010).
10 Edwards, P. P., Kuznetsov, V. L., David, W. I. F. & Brandon, N. P. Hydrogen and fuel cells: Towards a sustainable energy future. *Energy Policy* **36**, 4356-4362 (2008).
11 https://www.energy.gov/eere/fuelcells/fuel-cells. (August 15, 2018).
12 https://www.energy.gov/sites/prod/files/2017/05/f34/fcto_myrdd_fuel_cells.pdf. (September 25, 2018).
13 https://www.nasa.gov/centers/glenn/technology/fuel_cells.html. (August 20, 2018).
14 Zhang, Y., Lundblad, A., Campana, P. E. & Yan, J. Comparative Study of Battery Storage and Hydrogen Storage to Increase Photovoltaic Self-sufficiency in a Residential Building of Sweden. *Energy Procedia* **103**, 268-273 (2016).
15 Yoshida, T. & Kojima, K. Toyota MIRAI Fuel Cell Vehicle and Progress Toward a Future Hydrogen Society. *The Electrochemical Society Interface* (2015).
16 http://ec.europa.eu/regional_policy/en/projects/germany/hydrogen-fuel-cells-drive-clean-quiet-buses-in-cologne-and-amsterdam. (August 15, 2018).
17 https://www.fueleconomy.gov/feg/fcv_sbs.shtml. (August 15, 2018).
18 http://www.greencarcongress.com/2015/12/20151202-navigant.html. (August 15, 2018).
19 Thomas, S., Zalbowitz, M. & Cruz, J. Fuel Cells. *Los Alamos National Laboratory*.
20 Cook, B. An introduction to fuel cells and hydrogen technology. *Engineering Science and Education Journal* **11** (2001).
21 Rossmeisl, J., Karlberg, G. S., Jaramillo, T. & Nørskov, J. K. Steady state oxygen reduction and cyclic voltammetry. *Faraday Discuss.* **140**, 9-10 (2008).
22 Abild-Pedersen, F. *et al.* Scaling properties of adsorption energies for hydrogen-containing molecules on transition-metal surfaces. *Phys Rev Lett* **99**, 016105 (2007).
23 Duan, Z. & Wang, G. A first principles study of oxygen reduction reaction on a Pt(111) surface modified by a subsurface transition metal M (M = Ni, Co, or Fe). *Physical Chemistry Chemical Physics* **13**, 20178-20187 (2011).
24 Stamenkovic, V. *et al.* Changing the Activity of Electrocatalysts for Oxygen Reduction by Tuning the Surface Electronic Structure. *Angewandte Chemie* **118**, 2963-2967 (2006).
25 Gasteiger, H. A., Kocha, S. S., Sompalli, B. & Wagner, F. T. Activity benchmarks and requirements for Pt, Pt-alloy, and non-Pt oxygen reduction catalysts for PEMFCs. *Applied Catalysis B* **56**, 9-35 (2005).
26 Oezaslan, M. & Strasser, P. Activity of dealloyed PtCo3 and PtCu3 nanoparticle electrocatalyst for oxygen reduction reaction in polymer electrolyte membrane fuel cell. *Journal of Power Sources* **196**, 5240-5249 (2011).
27 Hasche, F., Oezaslan, M. & Strasser, P. Activity, Stability, and Degradation Mechanisms of Dealloyed PtCu3 and PtCo3 Nanoparticle Fuel Cell Catalysts. *Chemcatchem* **3**, 1805-1813 (2011).
28 Rudi, S., Tuaev, X. & Strasser, P. Electrocatalytic Oxygen Reduction on Dealloyed Pt1-xNix Alloy Nanoparticle Electrocatalysts. *Electrocatalysis* **3**, 265-273 (2012).
29 Oezaslan, M., Hasche, F. & Strasser, P. PtCu(3), PtCu and Pt(3)Cu Alloy Nanoparticle Electrocatalysts for Oxygen Reduction Reaction in Alkaline and Acidic Media. *Journal of the Electrochemical Society* **159**, B444-B454 (2012).
30 Asset, T. C., Raphael; Nelayah, Jaysen; Job, Nathalie; Dubau, Laetitia; Maillard, Frederic. Structure-Activity Relationships for the Oxygen Reduction Reaction in Porous Hollow PtNi/C Nanoparticles. *ChemElectroChem* **3**, 1591-1600 (2016).
31 Kongkanand, A. *et al.* Achieving High-Power PEM Fuel Cell Performance with an Ultralow-Pt-Content Core–Shell Catalyst. *ACS Catalysis* **6**, 1578-1583 (2016).

32 Wang, C. *et al.* Correlation Between Surface Chemistry and Electrocatalytic Properties of Monodisperse PtxNi1-x Nanoparticles. *Advanced Functional Materials* **21**, 147-152 (2011).
33 Paulus, U. A. *et al.* Oxygen Reduction on Carbon-Supported Pt−Ni and Pt−Co Alloy Catalysts. *The Journal of Physical Chemistry B* **106**, 4181-4191 (2002).
34 Stamenkovic, V. R. *et al.* Trends in electrocatalysis on extended and nanoscale Pt-bimetallic alloy surfaces. *Nat. Mater.* **6**, 241-247 (2007).
35 Tuaev, X., Rudi, S., Petkov, V., Hoell, A. & Strasser, P. In Situ Study of Atomic Structure Transformations of Pt-Ni Nanoparticle Catalysts during Electrochemical Potential Cycling. *ACS Nano* **7**, 5666 – 5674 (2013).
36 Gan, L., Cui, C., Rudi, S. & Strasser, P. Core-Shell and Nanoporous Particle Architectures and Their Effect on the Activity and Stability of Pt ORR Electrocatalysts. *Topics in Catalysis* **57**, 236-244 (2014).
37 Gan, L., Cui, C., Rudi, S. & Strasser, P. Core–Shell and Nanoporous Particle Architectures and Their Effect on the Activity and Stability of Pt ORR Electrocatalysts. *Topics in Catalysis* **57**, 236-244 (2013).
38 Dubau, L. *et al.* Tuning the Performance and the Stability of Porous Hollow PtNi/C Nanostructures for the Oxygen Reduction Reaction. *ACS Catalysis* **5**, 5333-5341 (2015).
39 Asset, T. *et al.* Structure–Activity Relationships for the Oxygen Reduction Reaction in Porous Hollow PtNiC Nanoparticles.pdf>. *ChemElectroChem* **3**, 1591-1600 (2016).
40 Bligaard, T. & Nørskov, J. K. Ligand effects in heterogeneous catalysis and electrochemistry. *Electrochimica Acta* **52**, 5512-5516 (2007).
41 Stamenkovic, V. *et al.* Changing the activity of electrocatalysts for oxygen reduction by tuning the surface electronic structure. *Angewandte Chemie-International Edition* **45**, 2897-2901 (2006).
42 Christensen, A. *et al.* Phase diagrams for surface alloys. *Physical Review B* **56**, 5822 (1997).
43 Hammer, B. & Norskov, J. K. Electronic factors determining the reactivity of metal surfaces. *Surface Science* **343**, 211-220 (1995).
44 Quaino, P., Santos, E., Soldano, G. & Schmickler, W. Recent Progress in Hydrogen Electrocatalysis. *Advances in Physical Chemistry* **2011**, 1-14 (2011).
45 Stamenkovic, V. R. *et al.* Improved oxygen reduction activity on Pt3Ni(111) via increased surface site availability. *Science* **315**, 493-497 (2007).
46 Han, B. *et al.* Record activity and stability of dealloyed bimetallic catalysts for proton exchange membrane fuel cells. *Energy & Environmental Science* **8**, 258-266 (2015).
47 Cui, C., Gan, L., Heggen, M., Rudi, S. & Strasser, P. Compositional segregation in shaped Pt alloy nanoparticles and their structural behaviour during electrocatalysis. *Nat Mater* **12**, 765-771 (2013).
48 Choi, S.-I. *et al.* Synthesis and Characterization of 9 nm Pt–Ni Octahedra with a Record High Activity of 3.3 A/mgPt for the Oxygen Reduction Reaction. *Nano Letters* **13**, 3420-3425 (2013).
49 Chen, C. *et al.* Highly Crystalline Multimetallic Nanoframes with Three-Dimensional Electrocatalytic Surfaces. *Science* **343**, 1339-1343 (2014).
50 Huang, X. *et al.* High-performance transition metal–doped Pt3Ni octahedra for oxygen reduction reaction. *Science* **348**, 1230-1234 (2015).
51 Li, M. *et al.* Ultrafine jagged platinum nanowires enable ultrahigh mass activity for the oxygen reduction reaction. *Science* **354**, 1414-1419 (2016).
52 Zhang, J., Yang, H., Fang, J. & Zou, S. Synthesis and Oxygen Reduction Activity of Shape-Controlled Pt3Ni Nanopolyhedra. *Nano Letters* **10**, 638 (2010).
53 Wu, J., Gross, A. & Yang, H. Shape and composition-controlled platinum alloy nanocrystals using carbon monoxide as reducing agent. *Nano Lett* **11**, 798-802 (2011).
54 Wu, J. *et al.* Icosahedral platinum alloy nanocrystals with enhanced electrocatalytic activities. *J Am Chem Soc* **134**, 11880-11883 (2012).
55 Cui, C. *et al.* Octahedral PtNi Nanoparticle Catalysts: Exceptional Oxygen Reduction Activity by Tuning the Alloy Particle Surface Composition. *Nano Letters* **12**, 5885-5889 (2012).
56 Li, M. *et al.* Ultrafine jagged platinum nanowires enable ultrahigh mass activity for the oxygen reduction reaction. *Science* **354**, 1414-1419 (2016).
57 Choi, S.-I. *et al.* Controlling the Size and Composition of Nanosized Pt–Ni Octahedra to Optimize Their Catalytic Activities toward the Oxygen Reduction Reaction. *ChemSusChem* **7**, 1476-1483 (2014).
58 Gan, L. *et al.* Element-specific anisotropic growth of shaped platinum alloy nanocrystals. *Science* **346**, 1502-1506 (2014).
59 Carpenter, M. K., Moylan, T. E., Kukreja, R. S., Atwan, M. H. & Tessema, M. M. Solvothermal Synthesis of Platinum Alloy Nanoparticles for Oxygen Reduction Electrocatalysis. *Journal of the American Chemical Society* **134**, 8535-8542 (2012).
60 Banham, D. & Ye, S. Current Status and Future Development of Catalyst Materials and Catalyst Layers for Proton Exchange Membrane Fuel Cells: An Industrial Perspective. *ACS Energy Letters* **2**, 629-638 (2017).

61 Konno, N., Mizuno, S., Nakaji, H. & Ishikawa, Y. Development of Compact and High-Performance Fuel Cell Stack. *SAE International Journal of Alternative Powertrains* **4** (2015).

62 Kongkanand, A. & Mathias, M. F. The Priority and Challenge of High-Power Performance of Low-Platinum Proton-Exchange Membrane Fuel Cells. *J Phys Chem Lett* **7**, 1127-1137 (2016).

63 Beermann, V. *et al.* Rh-Doped Pt–Ni Octahedral Nanoparticles: Understanding the Correlation between Elemental Distribution, Oxygen Reduction Reaction, and Shape Stability. *Nano Letters* **16**, 1719-1725 (2016).

64 Choi, S.-I. *et al.* Synthesis and Characterization of Pd@Pt–Ni Core–Shell Octahedra with High Activity toward Oxygen Reduction. *ACS Nano* **8**, 10363-10371 (2014).

65 Zhang, C., Sandorf, W. & Peng, Z. Octahedral Pt2CuNi Uniform Alloy Nanoparticle Catalyst with High Activity and Promising Stability for Oxygen Reduction Reaction. *ACS Catalysis* **5**, 2296-2300 (2015).

66 Arán-Ais, R. M. *et al.* Elemental Anisotropic Growth and Atomic-Scale Structure of Shape-Controlled Octahedral Pt–Ni–Co Alloy Nanocatalysts. *Nano Letters* 10.1021/acs.nanolett.5b03057 (2015).

67 Zhao, Z. *et al.* Composition tunable ternary Pt-Ni-Co octahedra for optimized oxygen reduction activity. *Chem Commun (Camb)* **52**, 11215-11218 (2016).

68 Jia, Q. *et al.* Roles of Mo Surface Dopants in Enhancing the ORR Performance of Octahedral PtNi Nanoparticles. *Nano Lett* **18**, 798-804 (2018).

69 Choi, J., Lee, Y., Kim, J. & Lee, H. Enhancing stability of octahedral PtNi nanoparticles for oxygen reduction reaction by halide treatment. *Journal of Power Sources* **307**, 883-890 (2016).

70 Lim, J. *et al.* Ga-Doped Pt-Ni Octahedral Nanoparticles as a Highly Active and Durable Electrocatalyst for Oxygen Reduction Reaction. *Nano Lett* **18**, 2450-2458 (2018).

71 Zhang, Y., Duan, Z., Xiao, C. & Wang, G. Density functional theory calculation of platinum surface segregation energy in Pt3Ni (111) surface doped with a third transition metal. *Surface Science* **605**, 1577-1582 (2011).

72 Rosa M. Arán-Ais, Francisco J. Vidal-Iglesias, Jose Solla-Gullón, Enrique Herrero & Feliu, J. M. Electrochemical Characterization of Clean Shape-Controlled Pt Nanoparticles Prepared in Presence of Oleylamine/Oleic Acid. *Electroanalysis* **27**, 945-956 (2015).

73 Ahmadi, M., Cui, C., Mistry, H., Strasser, P. & Roldan Cuenya, B. Carbon Monoxide-Induced Stability and Atomic Segregation Phenomena in Shape-Selected Octahedral PtNi Nanoparticles. *ACS Nano* **9**, 10686-10694 (2015).

74 Cui, C. *et al.* Shape-selected bimetallic nanoparticle electrocatalysts: evolution of their atomic-scale structure, chemical composition, and electrochemical reactivity under various chemical environments. *Faraday Discussions* **162**, 91-112 (2013).

75 Arán-Ais, R. M. *et al.* The effect of interfacial pH on the surface atomic elemental distribution and on the catalytic reactivity of shape-selected bimetallic nanoparticles towards oxygen reduction. *Nano Energy* **27**, 390-401 (2016).

76 Gan, L., Heggen, M., Cui, C. & Strasser, P. Thermal Facet Healing of Concave Octahedral Pt–Ni Nanoparticles Imaged in Situ at the Atomic Scale: Implications for the Rational Synthesis of Durable High-Performance ORR Electrocatalysts. *ACS Catalysis* **6**, 692-695 (2016).

77 Zana, A. *et al.* Probing Degradation by ILTEM: The Influence of Stress Test Conditions on the Degradation Mechanism. *Journal of The Electrochemical Society* **160**, F608-F615 (2013).

78 Meier, J. C. *et al.* Stability investigations of electrocatalysts on the nanoscale. *Energy & Environmental Science* **5**, 9319 (2012).

79 Nikkuni, F. R. *et al.* The role of water in the degradation of Pt3Co/C nanoparticles: An Identical Location Transmission Electron Microscopy study in polymer electrolyte environment. *Applied Catalysis B: Environmental* **156-157**, 301-306 (2014).

80 Zadick, A., Dubau, L., Zalineeva, A., Coutanceau, C. & Chatenet, M. When cubic nanoparticles get spherical: An Identical Location Transmission Electron Microscopy case study with Pd in alkaline media. *Electrochemistry Communications* **48**, 1-4 (2014).

81 Yu, Y. *et al.* Three-dimensional tracking and visualization of hundreds of Pt-Co fuel cell nanocatalysts during electrochemical aging. *Nano Lett* **12**, 4417-4423 (2012).

82 Bergmann, A. *et al.* Reversible amorphization and the catalytically active state of crystalline Co3O4 during oxygen evolution. *Nat Commun* **6**, 8625 (2015).

83 Holtz, M. E. *et al.* Nanoscale Imaging of Lithium Ion Distribution During In Situ Operation of Battery Electrode and Electrolyte. *Nano Letters* **14**, 1453-1459 (2014).

84 Maillard, F., Savinova, E. R., Simonov, P. A., Zaikovskii, V. I. & Stimming, U. Infrared Spectroscopic Study of CO Adsorption and Electro-oxidation on Carbon-Supported Pt Nanoparticles: Interparticle versus Intraparticle Heterogeneity. *The Journal of Physical Chemistry B* **108**, 17893-17904 (2004).

85 Park, S., Tong, Y. T., Wieckowski, A. & Weaver, M. J. Infrared spectral comparison of electrochemical carbon monoxide adlayers formed by direct chemisorption and methanol dissociation on carbon-supported platinum nanoparticles. *Langmuir* **18**, 3233-3240 (2002).

86 Rizo, R., Lazaro, M. J., Pastor, E. & Garcia, G. Spectroelectrochemical Study of Carbon Monoxide and Ethanol Oxidation on Pt/C, PtSn(3:1)/C and PtSn(1:1)/C Catalysts. *Molecules* **21** (2016).

87 Wang, Q. *et al.* Adsorption and oxidation of ethanol on colloid-based Pt/C, PtRu/C and Pt3Sn/C catalysts: In situ FTIR spectroscopy and on-line DEMS studies. *Physical Chemistry Chemical Physics* **9**, 2686-2696 (2007).

88 Abécassis, B., Testard, F., Spalla, O. & Barboux, P. Probing in situ the Nucleation and Growth of Gold Nanoparticles by Small-Angle X-ray Scattering. *Nano Letters* **7**, 1723-1727 (2007).

89 Zheng, F. *et al.* In-situ X-ray Absorption Study of Evolution of Oxidation States and Structure of Cobalt in Co and CoPt Bimetallic Nanoparticles (4 nm) under Reducing (H(2)) and Oxidizing (O(2)) Environments. *Nano Letters* **11**, 847-853 (2011).

90 de Jonge, N. & Ross, F. M. Electron microscopy of specimens in liquid. *Nat Nanotechnol* **6**, 695-704 (2011).

91 Williamson, M. J., Tromp, R. M., Vereecken, P. M., Hull, R. & Ross, F. M. Dynamic microscopy of nanoscale cluster growth at the solid-liquid interface. *Nat Mater* **2**, 532-536 (2003).

92 Ross, N. d. K. a. F. M. Liquid Cell Electron Microscopy; Chapter 1 *Past, Present, and Future Electron Microscopy of Liquid Specimens* (2017).

93 Zheng, H. M. *et al.* Observation of Single Colloidal Platinum Nanocrystal Growth Trajectories. *Science* **324**, 1309-1312 (2009).

94 Unocic, R. R. *et al.* Quantitative Electrochemical Measurements Using In Situ ec-S/TEM Devices. *Microsc Microanal* **20**, 452-461 (2014).

95 Zhu, G.-Z. *et al.* In Situ Liquid Cell TEM Study of Morphological Evolution and Degradation of Pt–Fe Nanocatalysts During Potential Cycling. *The Journal of Physical Chemistry C* **118**, 22111-22119 (2014).

96 Hodnik, N., Dehm, G. & Mayrhofer, K. J. Importance and Challenges of Electrochemical in Situ Liquid Cell Electron Microscopy for Energy Conversion Research. *Acc Chem Res* **49**, 2015-2022 (2016).

97 Nagashima, S. *et al.* In situ Liquid TEM Study for Degradation Mechanisms of Fuel Cell Catalysts during Potential Cycling Test. *Microscopy and Microanalysis* **21**, 1295-1296 (2015).

98 Holtz, M. E., Yu, Y., Rivera, J., Abruña, H. D. & Muller, D. A. In Situ TEM for Quantitative Electrochemistry of Energy Systems. *Microscopy and Microanalysis* **21**, 1509-1510 (2015).

99 Kato, H. In-Situ Liquid TEM Study on the Degradation Mechanism of Fuel Cell Catalysts. *SAE International Journal of Alternative Powertrains* **5** (2016).

100 Zeng, Z., Liang, W. I., Chu, Y. H. & Zheng, H. In situ TEM study of the Li-Au reaction in an electrochemical liquid cell. *Faraday Discuss* **176**, 95-107 (2014).

101 Khan, S., Gupta, A., Verma, N. C. & Nandi, C. K. Time-Resolved Emission Reveals Ensemble of Emissive States as the Origin of Multicolor Fluorescence in Carbon Dots. *Nano Lett* **15**, 8300-8305 (2015).

102 Gu, M. *et al.* Demonstration of an electrochemical liquid cell for operando transmission electron microscopy observation of the lithiation/delithiation behavior of Si nanowire battery anodes. *Nano Lett* **13**, 6106-6112 (2013).

103 Unocic, R. R. *et al.* Direct visualization of solid electrolyte interphase formation in lithium-ion batteries with in situ electrochemical transmission electron microscopy. *Microsc Microanal* **20**, 1029-1037 (2014).

104 Riley, B. T. *et al.* Direct and indirect mechanisms of KLK4 inhibition revealed by structure and dynamics. *Sci Rep* **6**, 35385 (2016).

105 LaMer, V. K. & Dinegar, R. H. Theory, Production and Mechanism of Foramtion of Monidisperse Hydrosols. *Journal of the American Chemical Society* **72**, 4847-4854 (1950).

106 Xiong, Y. & Xia, Y. Shape-Controlled Synthesis of Metal Nanostructures: The Case of Palladium. *Advanced Materials* **19**, 3385-3391 (2007).

107 Xia, Y., Xiong, Y. J., Lim, B. & Skrabalak, S. E. Shape-Controlled Synthesis of Metal Nanocrystals: Simple Chemistry Meets Complex Physics? *Angewandte Chemie-International Edition* **48**, 60-103 (2009).

108 Peng, Z. & Yang, H. Designer platinum nanoparticles: Control of shape, composition in alloy, nanostructure and electrocatalytic property. *Nano Today* **4**, 143-164 (2009).

109 Roldan Cuenya, B. & Behafarid, F. Nanocatalysis: size- and shape-dependent chemisorption and catalytic reactivity. *Surface Science Reports* **70**, 135-187 (2015).

110 Solla-Gullón, J. *et al.* Shape-dependent electrocatalysis: methanol and formic acid electrooxidation on preferentially oriented Pt nanoparticles. *Phys Chem Chem Phys* **10**, 3689-3698 (2008).

111 Williams, D. B. & Carter, C. B. Transmission Electron Microscopy; p7ff, p122, p135, p158 (2009).

112 Saka, H., Kamino, T., Arai, S. & Sasaki, K. In Situ Heating Transmission Electron Microscopy. *MRS Bulletin* **33** (2008).

113 Ross, N. d. J. a. F. M. Vol. Chapter 1*Liquid Cell Electron Microscopy* (2017).

114 Grogan, J. M., Schneider, N. M., Ross, F. M. & Bau, H. H. Bubble and pattern formation in liquid induced by an electron beam. *Nano Lett* **14**, 359-364 (2014).
115 András Kovács, R. S., Karsten Tillmann. FEI Titan G2 80-200 CREWLEY. *Journal of large-scale research facilities JLSRF* **2**, 1-4 (2016).
116 Protochips. http://www.protochips.com/products/fusion/fusion-media/ (July 20, 2018).
117 Holtz, M. E., Yu, Y. C., Gao, J., Abruna, H. D. & Muller, D. A. In Situ Electron Energy-Loss Spectroscopy in Liquids. *Microscopy and Microanalysis* **19**, 1027-1035 (2013).
118 Klein, K. L., Anderson, I. M. & de Jonge, N. Transmission electron microscopy with a liquid flow cell. *J Microsc* **242**, 117-123 (2011).
119 Luisier, F., Vonesch, C., Blu, T. & Unser, M. Fast interscale wavelet denoising of Poisson-corrupted images. *Signal Processing* **90**, 415-427 (2010).
120 Luisier, F. The SURE-LET Approach to Image Denoising. *Swiss Federal Institute of Technology Lausanne - EPFL Thesis* **4566** (2010).
121 Luisier, F., Vonesch, C., Blu, T. & Unser, M. in *Biomedical Imaging: From Nano to Macro, 2009. ISBI'09. IEEE International Symposium on.* 310-313 (IEEE).
122 Niemantsverdriet, J. W. Spectroscopy in Catalysis; *Vibrational Spectroscopy* p218, p224, p233 (WILEY-VCH Verlag GmbH & Co. KGaA, Weinheim, 2007).
123 Schuttlefield, J. D. & Grassian, V. H. ATR–FTIR Spectroscopy in the Undergraduate Chemistry Laboratory. *J. Chem. Educ.* **85**, 279-281 (2008).
124 Mojet, B. L., Ebbesen, S. D. & Lefferts, L. Light at the interface: the potential of attenuated total reflection infrared spectroscopy for understanding heterogeneous catalysis in water. *Chem Soc Rev* **39**, 4643-4655 (2010).
125 Erini, N. *et al.* The Effect of Surface Site Ensembles on the Activity and Selectivity of Ethanol Electrooxidation by Octahedral PtNiRh Nanoparticles. *Angew Chem Int Ed Engl* **56**, 6533-6538 (2017).
126 Jusys, Z., Massong, H. & Baltruschat, H. A new approach for simultaneous DEMS and EQCM: Electro-oxidation of adsorbed CO on Pt and Pt-Ru. *Journal of the Electrochemical Society* **146**, 1093-1098 (1999).
127 Kang, Y. *et al.* Shape-Controlled Synthesis of Pt Nanocrystals: The Role of Metal Carbonyls. *ACS Nano* **7**, 645-653 (2013).
128 Alpay, D., Peng, L. & Marks, L. D. Are Nanoparticle Corners Round? *The Journal of Physical Chemistry C* **119**, 21018-21023 (2015).
129 Grozovski, V., Solla-Gullon, J., Climent, V., Herrero, E. & Feliu, J. M. Formic Acid Oxidation on Shape-Controlled Pt Nanoparticles Studied by Pulsed Voltammetry. *Journal of Physical Chemistry C* **114**, 13802-13812 (2010).
130 Energy, U. S. D. o. Technical Plan - Fuel Cells. *Multi-Year Research, Developement and Demonstration Plan* (2012).
131 Vanysek, P. Electrochemical Series. *CRC PRESS LLC* (2000).
132 Beermann, V. *et al.* Tuning the Electrocatalytic Oxygen Reduction Reaction Activity and Stability of Shape-controlled Pt-Ni Nanoparticles by Thermal Annealing – Elucidating the Surface Atomic Structural and Compositional Changes. *Journal of the American Chemical Society* **139**, 16536–16547 (2017).
133 Rudi, S. C., Chunhua; Gan, Lin; Strasser, Peter. Comparative Study of the Electrocatalytically Active Surface Areas (ECSAs) of Pt Alloy Nanoparticles Evaluated by Hupd and CO-stripping voltammetry. *Electrocatalysis* **5**, 408-418 (2014).
134 Strasser, P., Koha, S. & Greeley, J. Voltammetric surface dealloying of Pt bimetallic nanoparticles: an experimental and DFT computational analysis. *Physical Chemistry Chemical Physics* **10**, 3670-3683 (2008).
135 van der Vliet, D. F. *et al.* Unique Electrochemical Adsorption Properties of Pt-Skin Surfaces. *Angewandte Chemie, International Edition* **51**, 3139 (2012).
136 Lopez-Cudero, A., Solla-Gullon, J., Herrero, E., Aldaz, A. & Feliu, J. M. CO electrooxidation on carbon supported platinum nanoparticles: Effect of aggregation. *Journal of Electroanalytical Chemistry* **644**, 117-126 (2010).
137 Clavilier, J., Actii, K. E., Petit, M., Rodes, A. & Zamakhchari, M. A. Electrochemical monitoring of the thermal reordering of platinum single-crystal surfaces after metallographic polishing from the early stage to the equlilibrium surface. *Journal of Electroanalytical Chemistry and Interfacial Electrochemistry* **295**, 333-356 (1990).
138 Gan, L., Heggen, M., O'Malley, R., Theobald, B. & Strasser, P. Understanding and controlling nanoporosity formation for improving the stability of bimetallic fuel cell catalysts. *Nano Lett* **13**, 1131-1138 (2013).
139 Li, L. Z., Lu; Ould-Chikh, Samy; Anjum, Dalaver H.; Kanoun, Mohammed B.; Scaranto, Jessica; Hedhili, Mohamed N.; Khalid, Syed; Laveille, Paco V.; D'Souza, Lawrence; Clo, Alain; Basset, Jean-Marie Controlled Surface Segregation Leads to Efficient Coke-Resistant Nickel/Platinum Bimetallic Catalysts for the Dry Reforming of Methane. *ChemCatChem* **7**, 819-829 (2015).

140 Pecharromán, C., Cuesta, A. & Gutiérrez, C. Comments on the paper by M.-S. Zheng and S.-G. Sun entitled 'In situ FTIR spectroscopic studies of CO adsorption on electrodes with nanometer-scale thin films of ruthenium in sulfuric acid solutions' [J. Electroanal. Chem. 500 (2001) 223]. *Journal of Electroanalytical Chemistry* **529**, 145-154 (2002).

141 Park, S., Tong, Wieckowski, A. & Weaver, M. J. Infrared Spectral Comparison of Electrochemical Carbon Monoxide Adlayers Formed by Direct Chemisorption and Methanol Dissociation on Carbon-Supported Platinum Nanoparticles. *Langmuir* **18**, 3233-3240 (2002).

142 Cuesta, A. *et al.* Potential dependence of the saturation CO coverage of Pt electrodes: The origin of the pre-peak in CO-stripping voltammograms. Part 3: Pt(poly). *Journal of Electroanalytical Chemistry* **586**, 184-195 (2006).

143 López-Cudero, A., Cuesta, Á. & Gutiérrez, C. Potential dependence of the saturation CO coverage of Pt electrodes: The origin of the pre-peak in CO-stripping voltammograms. Part 2: Pt(100). *Journal of Electroanalytical Chemistry* **586**, 204-216 (2006).

144 Dubau, L. *et al.* Defects do Catalysis: CO Monolayer Oxidation and Oxygen Reduction Reaction on Hollow PtNi/C Nanoparticles. *ACS Catalysis* **6**, 4673-4684 (2016).

145 Chattot, R. *et al.* Beyond Strain and Ligand Effects: Microstrain-Induced Enhancement of the Oxygen Reduction Reaction Kinetics on Various PtNi/C Nanostructures. *ACS Catalysis* **7**, 398-408 (2017).

146 Beermann, V., Kühl, S. & Strasser, P. Tuning the Catalytic Oxygen Reduction Reaction Performance of Pt-Ni Octahedral Nanoparticles by Acid Treatments and Thermal Annealing. *Journal of The Electrochemical Society* **165**, J3026-J3030 (2018).

147 Zhang, B.-W. *et al.* Tuning Pt-skin to Ni-rich surface of Pt 3 Ni catalysts supported on porous carbon for enhanced oxygen reduction reaction and formic electro-oxidation. *Nano Energy* **19**, 198-209 (2016).

148 Zheng, L. *et al.* Improving the Performance of Platinum Nanocrystal Catalysts by Square-wave Potential Electrochemical Pretreatment. *Fuel Cells* **10**, 384-389 (2010).

149 Rudi, S., Gan, L., Cui, C., Gliech, M. & Strasser, P. Electrochemical Dealloying of Bimetallic ORR Nanoparticle Catalysts at Constant Electrode Potentials. *Journal of The Electrochemical Society* **162**, F403-F409 (2015).

150 Filmer, A. O. The non-oxidative dissolution of nickel mattes in aqueous acidic solutions. *Journal of the South African Institute of Mining and Metallurgy*, 74-84 (1981).

151 Schneider, N. M. *et al.* Electron–Water Interactions and Implications for Liquid Cell Electron Microscopy. *The Journal of Physical Chemistry C* **118**, 22373-22382 (2014).

152 Shao-Horn, Y., Holby, E. F., Sheng, W. C. & Morgan, D. Pt nanoparticle stability in PEM fuel cells: influence of particle size distribution and crossover hydrogen. *Energy & Environmental Science* **2**, 865-871 (2009).

153 Cherevko, S., Zeradjanin, A. R., Keeley, G. P. & Mayrhofer, K. J. J. A Comparative Study on Gold and Platinum Dissolution in Acidic and Alkaline Media. *Journal of the Electrochemical Society* **161**, H822-H830 (2014).

154 Cherevko, S. *et al.* Dissolution of Platinum in the Operational Range of Fuel Cells. *Chemelectrochem* **2**, 1471-1478 (2015).

155 Topalov, A. A. *et al.* Dissolution of Platinum: Limits for the Deployment of Electrochemical Energy Conversion? *Angewandte Chemie-International Edition* **51**, 12613-12615 (2012).

156 Stevens, D. A., Hicks, M. T., Haugen, G. M. & Dahn, J. R. Ex Situ and In Situ Stability Studies of PEMFC Catalysts Effect of Carbon Type and Humidification on Degradation of the Carbon. *Journal of Electrochemical Society* **152**, A2309 - A2315 (2005).

157 Makharia, R. *et al.* Durable PEM Fuel Cell Electrode Materials: Requirements and Benchmarking Methodologies. *ECS Transactions* **1**, 3-18 (2006).

158 Willsau, J. & Heitbaum, J. The Influence of Pt-Activation on the Corrosion of Carbon in Gas-Diffusion Electrodes - a Dems Study. *Journal of Electroanalytical Chemistry* **161**, 93-101 (1984).

159 Zamel, N., Hanke-Rauschenbach, R., Kirsch, S., Bhattarai, A. & Gerteisen, D. Relating the N-shaped polarization curve of a PEM fuel cell to local oxygen starvation and hydrogen evolution. *International Journal of Hydrogen Energy* **38**, 15318-15327 (2013).

160 Rabis, A., Rodriguez, P. & Schmidt, T. J. Electrocatalysis for Polymer Electrolyte Fuel Cells: Recent Achievements and Future Challenges. *Acs Catalysis* **2**, 864-890 (2012).

161 Yu, Y. *et al.* Understanding Pt-Co Catalyst Degradation Mechanism: from Ex-situ to In-situ. *Microscopy and Microanalysis* **19**, 1666-1667 (2013).

162 Huang, Y. *et al.* Transient Platinum Oxide Formation and Oxygen Reduction on Carbon-Supported Platinum and Platinum-Cobalt Alloy Elect. *Journal of The Electrochemical Society* **161**, F10-F15 (2014).

Appendix

A1 Supplementary Information to Chapter 4

Rh-doped Pt-Ni Octahedral Nanoparticles: Understanding the Correlation Between Elemental Distribution, ORR and Shape Stability

Table S1.1 Evaluation of XRD data as well as the calculated 2Θ values calculated from the ideal Vegard's law, using a bimetallic alloy of *Pt-Rh-Ni*.

$Pt_{81}Ni_{19}$/C oct			
hkl	**d**	**$2\Theta_{theo}$**	**$2\Theta_{real}$**
111	2.22	40.57	40.83
200	1.92	47.23	47.23
220	1.36	69.02	69.43
$Pt_{71}Rh_3Ni_{26}$/C oct ($Pt_{73}Ni_{27}$ assumption)			
hkl	**d**	**$2\Theta_{theo}$**	**$2\Theta_{real}$**
111	2.20	40.94	40.74
200	1.91	47.63	47.32
220	1.35	69.65	69.29

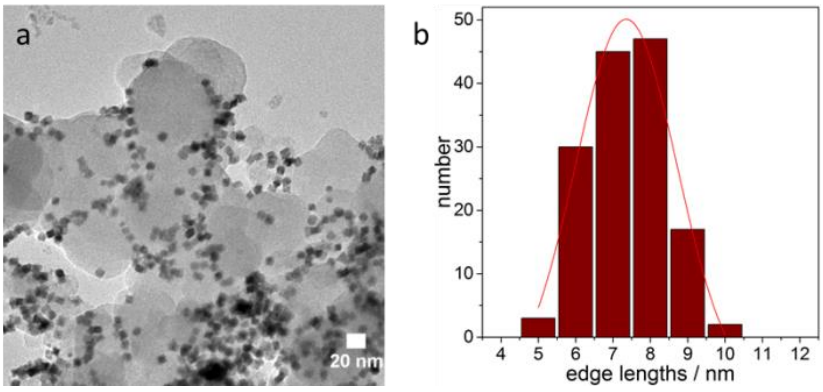

Figure S1.1 a) Overview of *Pt-Rh-Ni* octahedral nanoparticles distribution on carbon and **b)** particle size distribution of *Pt-Rh-Ni/C* particles (based on 144 particles) with average edge length of 7.4 ± 1.0 nm, obtained from the fitted profile (Gaussian distribution).

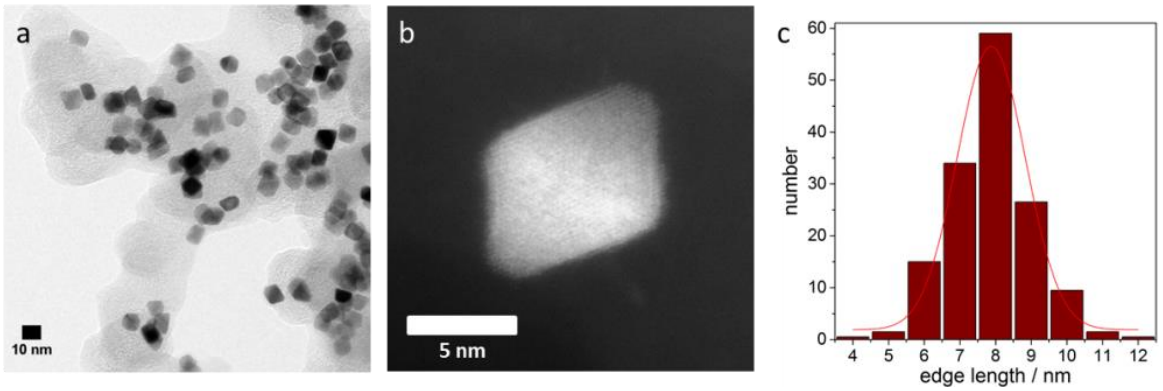

Figure S1.2 Transmission electron microscopy images of *Pt-Ni/C* after synthesis and acetic acid treatment. **a)** overview of the particles with a homogeneous distribution and mainly octahedral shaped nanoparticles, **b)** STEM image of *Pt-Ni/C*, **c)** Particle size distribution of *Pt-Ni/C* octahedral nanoparticles (based on 296 particles) with average edge length of 7.9 ± 1.1 nm, obtained from the fitted profile (Gaussian distribution).

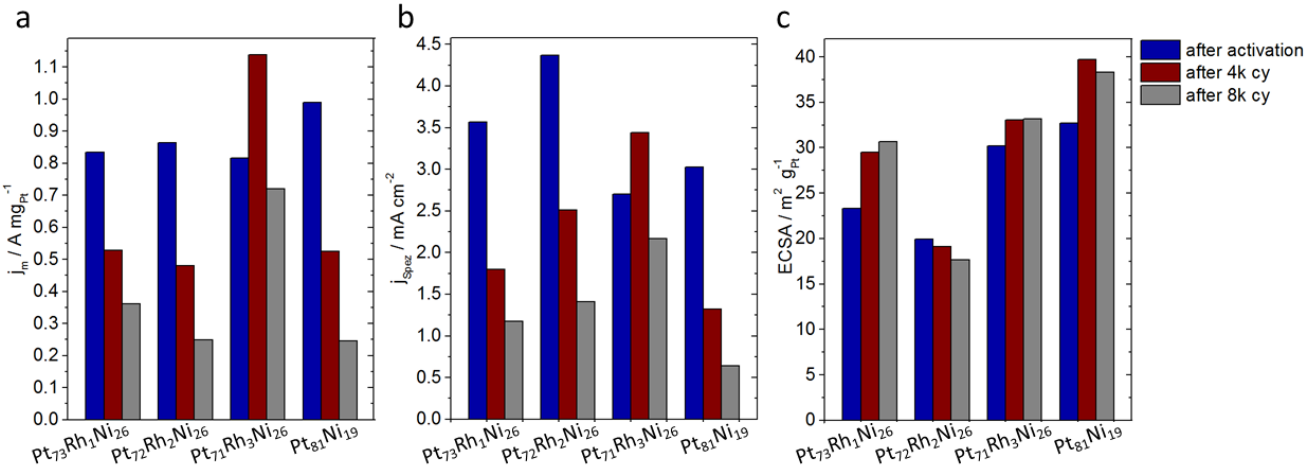

Figure S1.3 Electrochemical characterization and effect of the amount Rh on the: **a)** mass based activities, **b)** specific activities based on H_{upd}-ECSA and **c)** H_{upd} ECSA after 20 cycles (cy) activation, 4k and 8k cycles (cy) stability test (LSV: 0.05 – 1.0 V vs. RHE with 10 mV s^{-1} in O_2 saturated 0.1 M $HClO_4$ electrolyte, 1600 rpm, evaluated at 0.9 V; CV: 0.05 – 1.0 V vs. RHE with 100 mV s^{-1} in N_2 saturated 0.1 M $HClO_4$ electrolyte, 0 rpm).

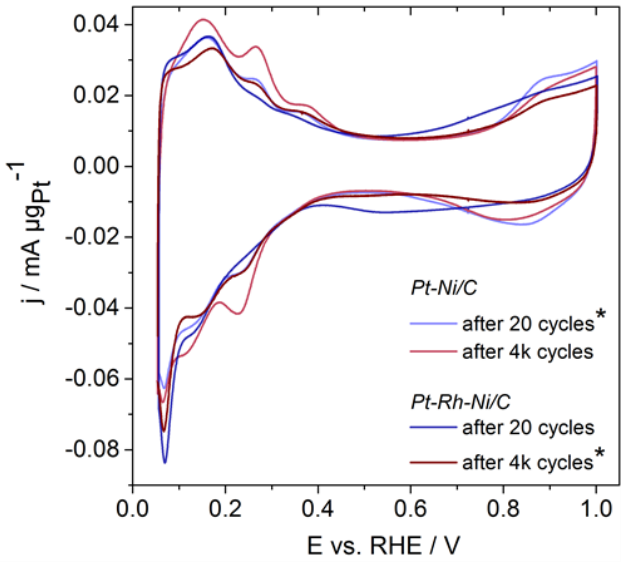

Figure S1.4 Comparison of CVs of the *Pt-Ni/C* and the *Pt-Rh-Ni/C* catalyst after activation and after 4k cycles stability, * is indicating the most active states, respectively, where shape of the CVs looks quite similar in the H_{upd} region.

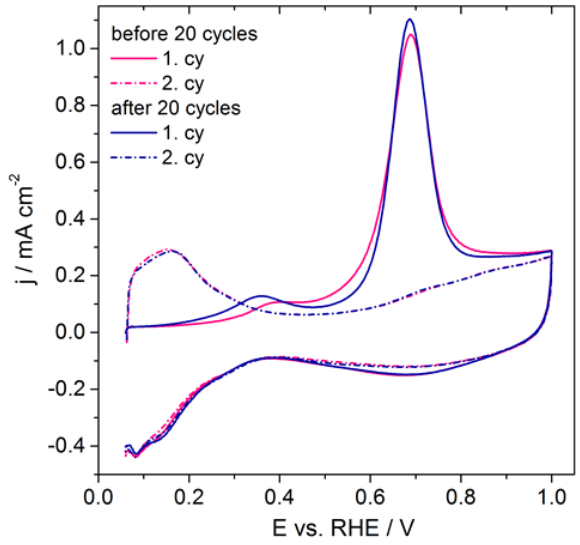

Figure S1.5 CO-Oxidation experiment of the *Pt-Rh-Ni/C* catalyst before and after 20 cycles activation; 0.05-1.0 V vs. RHE with 50 mV s^{-1} in N_2 saturated 0.1 M $HClO_4$.

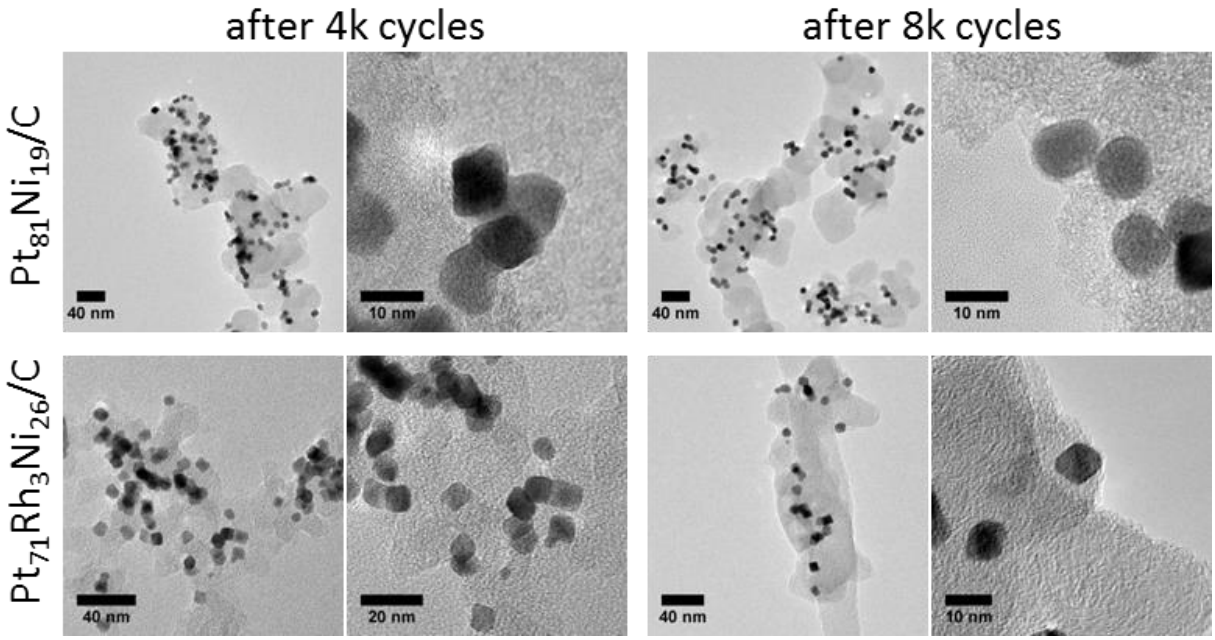

Figure S1.6 TEM images for the comparison of shape stability of the pure *Pt-Ni/C* catalyst and the *Pt-Rh-Ni/C* catalyst after 4k and after 8k cycles stability test.

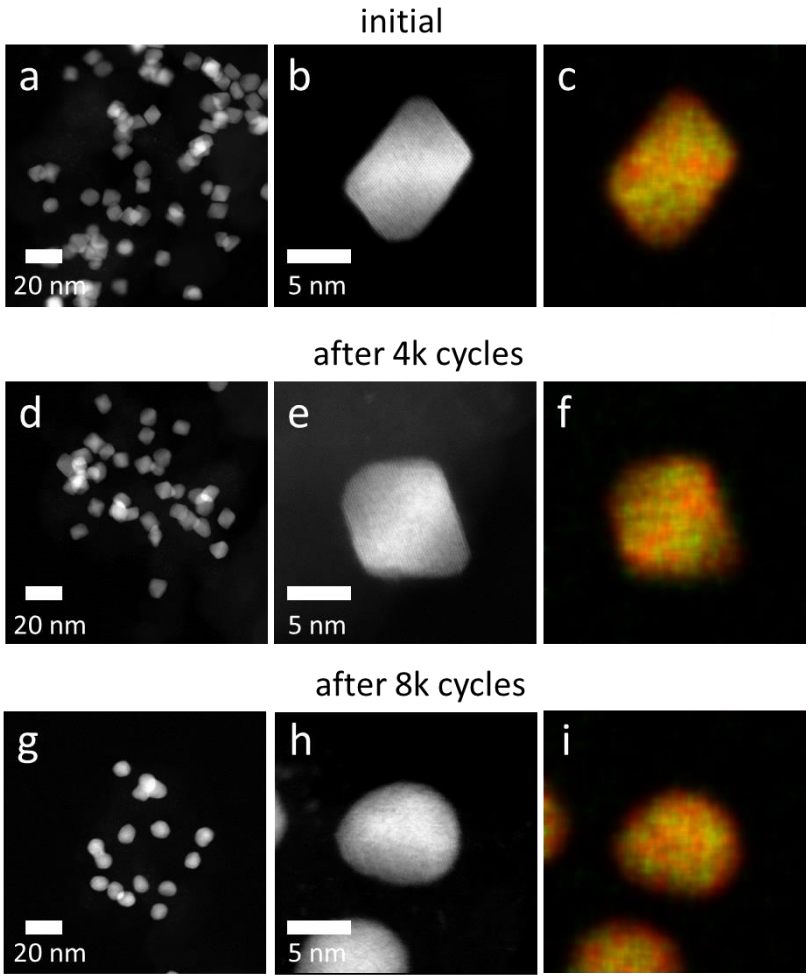

Figure S1.7 HAADF STEM images and EDX composition maps of *Pt-Ni* nanoparticles. **a, d, g** HAADF STEM overview images of the nanoparticles in the initial state **(a)**, after 4 k cycles **(d)**, and after 8 k cycles **(g)**. **b, e, h,** High resolution HAADF STEM images of *Pt-Ni* octahedral nanoparticles in different states. **c, f, i** Pt (red) and Ni (green) EDX composition map of the corresponding nanoparticles.

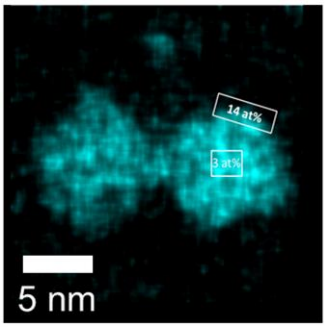

Figure S1.8 Rh distribution in an EDX composition map of initial *Pt-Rh-Ni* nanoparticles. The amount of Rh in atomic percent is indicated in the corresponding area (white boxes).

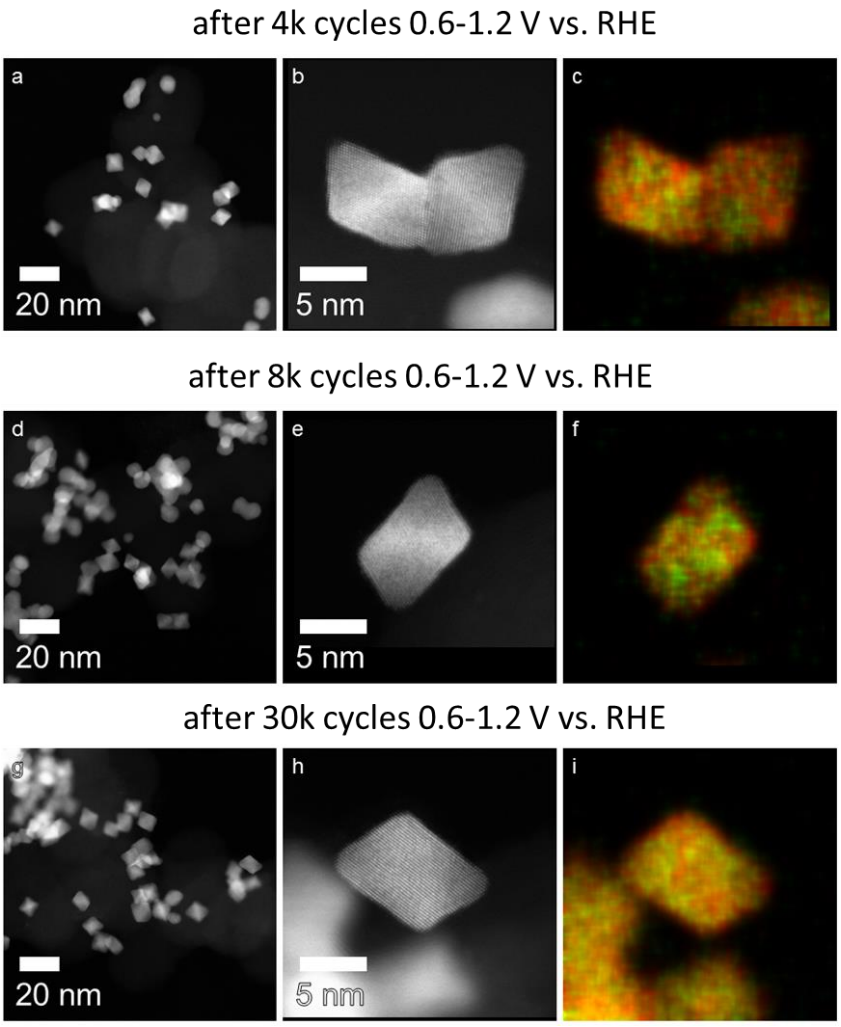

Figure S1.9 HAADF STEM images and EDX composition maps of *Pt-Rh-Ni* octahedral nanoparticles after 4 k cycles **(a,b,c)**, after 8 k cycles **(d,e,f)** and after 30 k cycles **(g,h,i)** between 0.6 and 1.2 V vs. RHE. Overview HAADF STEM images **(a,d,g)** and high resolution HAADF STEM images of PtNiRh octahedral nanoparticles oriented close to ⟨110⟩ **(b,e,h)**. Pt (red) and Ni (green) EDX composition maps of the corresponding octahedral nanoparticles **(c,f,i)**.

Figure S1.9 and Figure S1.10 show HAADF STEM images and EDX composition maps of the respective *Pt-Rh-Ni* nanoparticles. Figure S1.9 indicates that octahedral nanoparticles with a similar Pt and Ni distribution and composition are present as for the nanoparticles cycled between 0.05 and 1.0 V vs. RHE. With an increasing number of cycles, the segregated structure is lost and a more homogeneously alloyed nanoparticle structure is observed. However, after applying potential cycles between 0.6 and 1.2 V vs. RHE additional spherical-shaped particles are found with a Ni-rich core and a Pt-rich shell (Figure S1.10). The core-shell structure is clearly visible in the EDX maps (especially in Figure S1.10 f and i) as well as by the contrast difference in the HAADF STEM images (Figure S1.10 e and h). In the spherical-shaped nanoparticles most of the Ni is leached out due to the higher potential over 1.1 V and only a small Ni content between 7 and 16 at.% remains. In contrast to the application of cycles between 0.5 and 1.0 V vs. RHE, it is obvious that after the cycles between 0.6 and 1.2 V vs. RHE, a mixture of octahedral and spherical-shape particles is observed. Interestingly, only the

octahedral nanoparticles retain a high Ni content. Possible reasons for the formation of these heavy degraded particles could be (i) less Rh accumulation in the outer novel metal shell in the initial particle and therefore a change in the Pt diffusion rate behavior during electrochemical cycling or (ii) a slightly thinner Pt-Rh shell in the initial particles. Applying a potential higher than 1.0 V on these "defect" particles changes the diffusion rate behavior of Pt and therefore might inducing the dissolution of Ni. As soon as only small amounts of Ni are able to reach the surface and thereby to dissolve from the particle, pin-holes are built and a strong degradation process is taking place. In comparison, the particles which are still octahedral after stability measurements up to 1.2 V vs. RHE, seems to exhibit a Pt-Rh shell still thick enough to protect Ni from leaching. As a result, they are not undergoing a structural degradation process, and are showing a similar behavior, i.e. structural rearrangement of Pt and Ni atoms, losing of favorable Ni segregation directly beneath of Pt-Rh shell, like the particles only cycled up to 1.0 V.

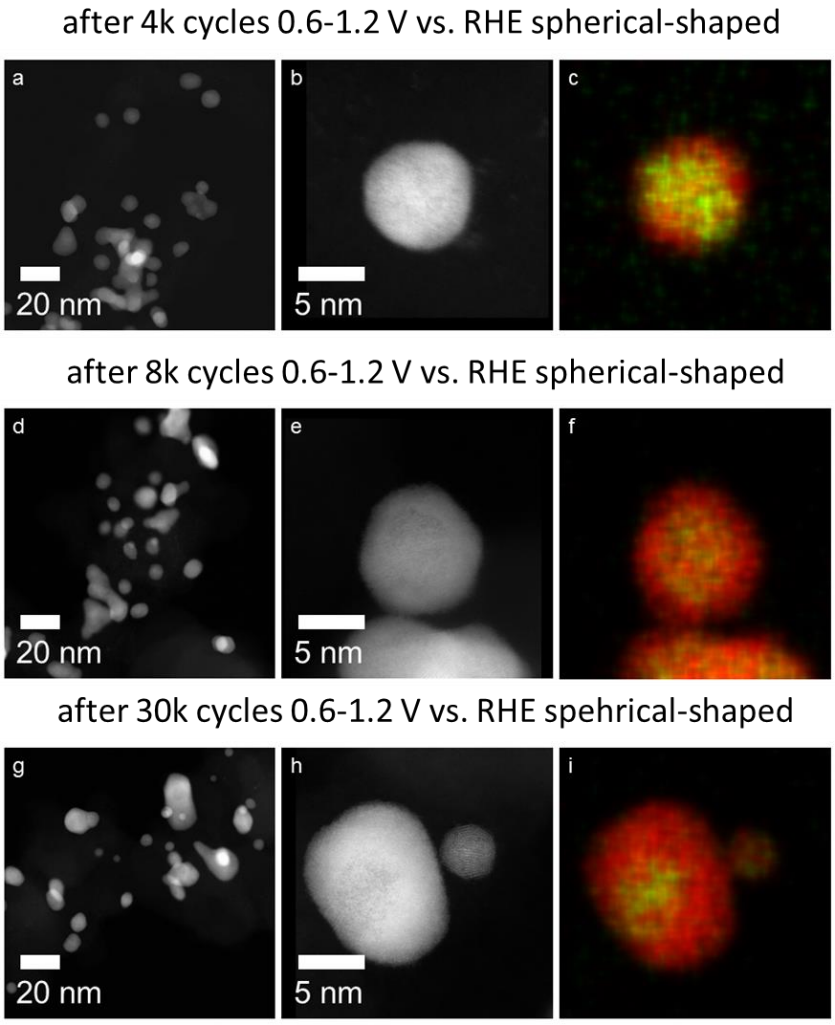

Figure S1.10 HAADF STEM images and EDX composition maps of spherical-shaped *Pt-Rh-Ni* nanoparticles after 4 k cycles **(a,b,c)**, after 8 k cycles **(d,e,f)** and after 30 k cycles **(g,h,i)** between 0.6 and 1.2 V vs. RHE. Overview **(a,d,g)** and high resolution HAADF STEM images **(b,e,h)** as well as Pt (red) and Ni (green) EDX composition maps of the corresponding nanoparticles **(c,f,i)**.

A2 Supplementary Information to Chapter 5

Tuning the Electrocatalytic Oxygen Reduction Reaction Activity and Stability of Shape-Controlled Pt-Ni Nanoparticles by Thermal Annealing - Elucidating the Surface Atomic Structural and Compositional Changes

Details to Rietveld Refinement:

- background: Chebychev with 4/5 polynomial coefficients
- phases:
  - two Pt fcc with Pt and Ni sites
    - phase 1: Pt and Ni occupancy was applied according to composition 0.6 and 0.4, respectively
    - phase 2: Pt and Ni occupancy was refined
  - one Ni fcc
  - additional peak phases to subtract carbon support or influence of holder: 24.98°2θ, 30.37°2θ and 43.2°2θ

Table S2.1 Phase composition as obtained by Rietveld refinement of XRD pattern – values given in weight%.

Sample	PtNi phase 1	PtNi phase 2	Ni phase
PtNi_raw	64.5	6.0	29.5
PtNi_300	63.2	13.8	23.0
PtNi_500	65.5	26.2	8.3

Table S2.2 Structural parameters obtained by Rietveld refinement of XRD pattern.

Sample	PtNi phase 1		PtNi phase 2		Ni phase		Rwp
	a	**LVol-IB**	**a**	**LVol-IB**	**a**	**LVol-IB**	
PtNi_raw	3.7707(24)	7.79	3.7783(34)	2.458(68)	3.4891(22)	7.85(22)	1.06
PtNi_300	3.7770(35)	7.30(52)	3.8060(65)	1.97(11)	3.4951(33)	8.76(40)	1.28
PtNi_500	3.7551(26)	8.493(53)	3.7256(31)	2.424(69)	3.5218(24)	7.45(25)	1.12

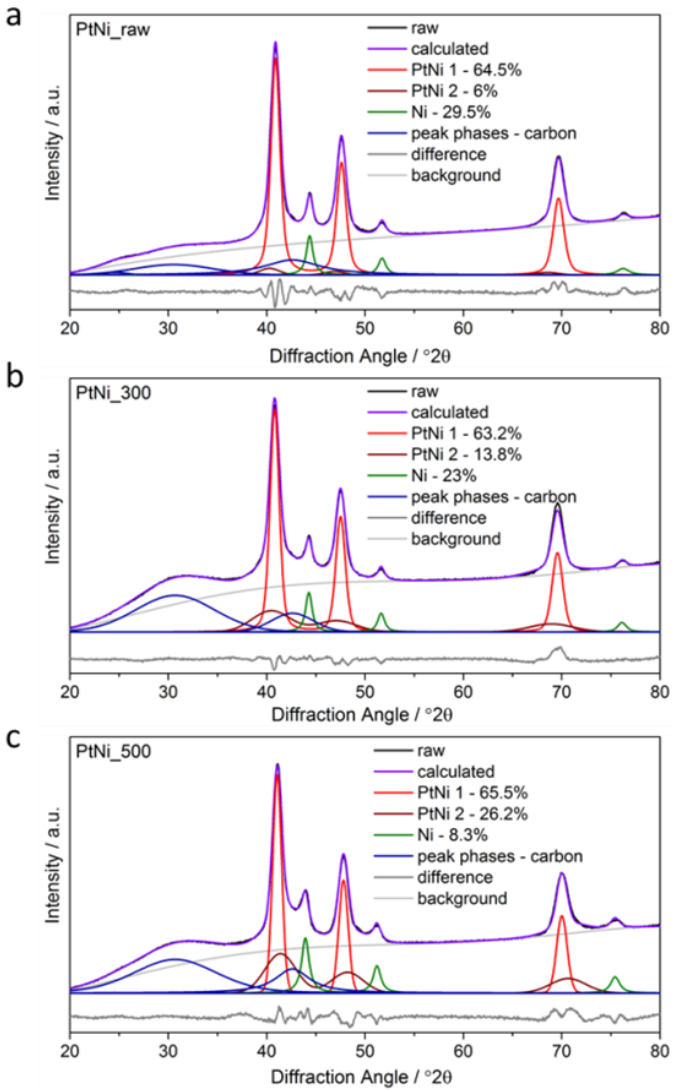

Figure S2.1 Rietveld refinement patterns of PtNi_raw, PtNi_300 and PtNi_500.

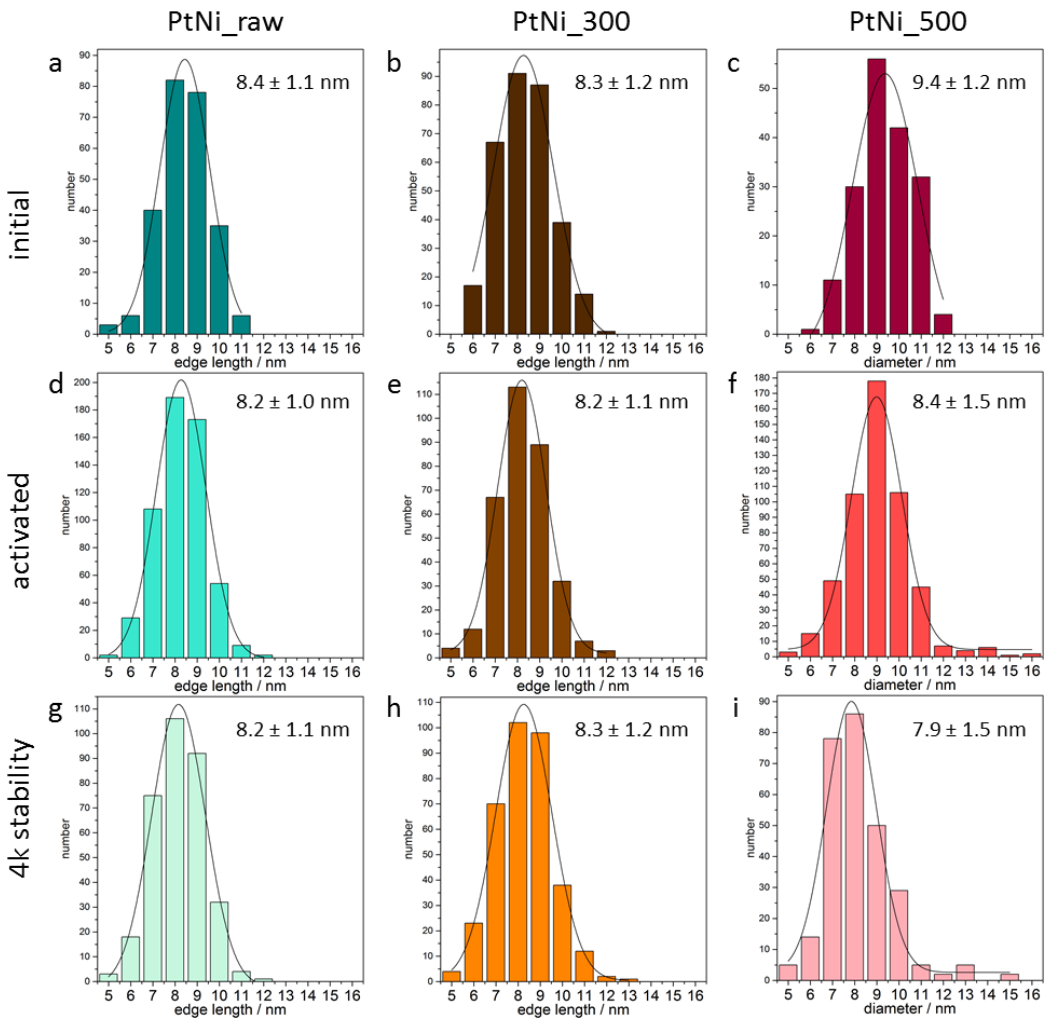

Figure S2.2 Particle size distribution of *PtNi_raw* ***(a, d, g)***, *PtNi_300* ***(b, e, h)*** and *PtNi_500* ***(c, f, i)*** in the initial state, after activation and after 4k stability test with the corresponding Gaussian fit.

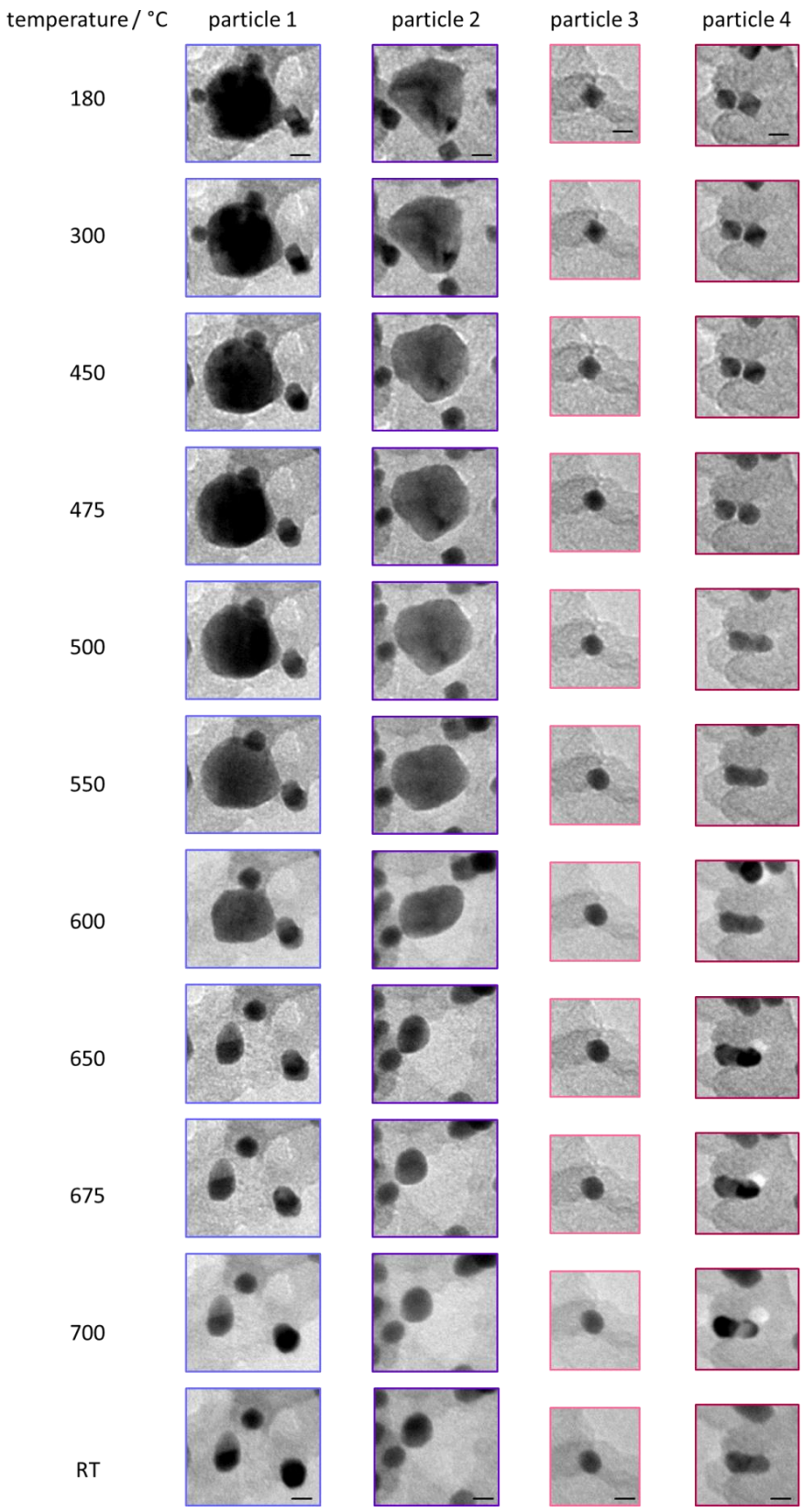

Figure S2.3 *In situ* heating TEM images selected from Figure 2. Selected images enlarged for improved disclosure of changes in nanoparticle shape. Scalebars: 10 nm.

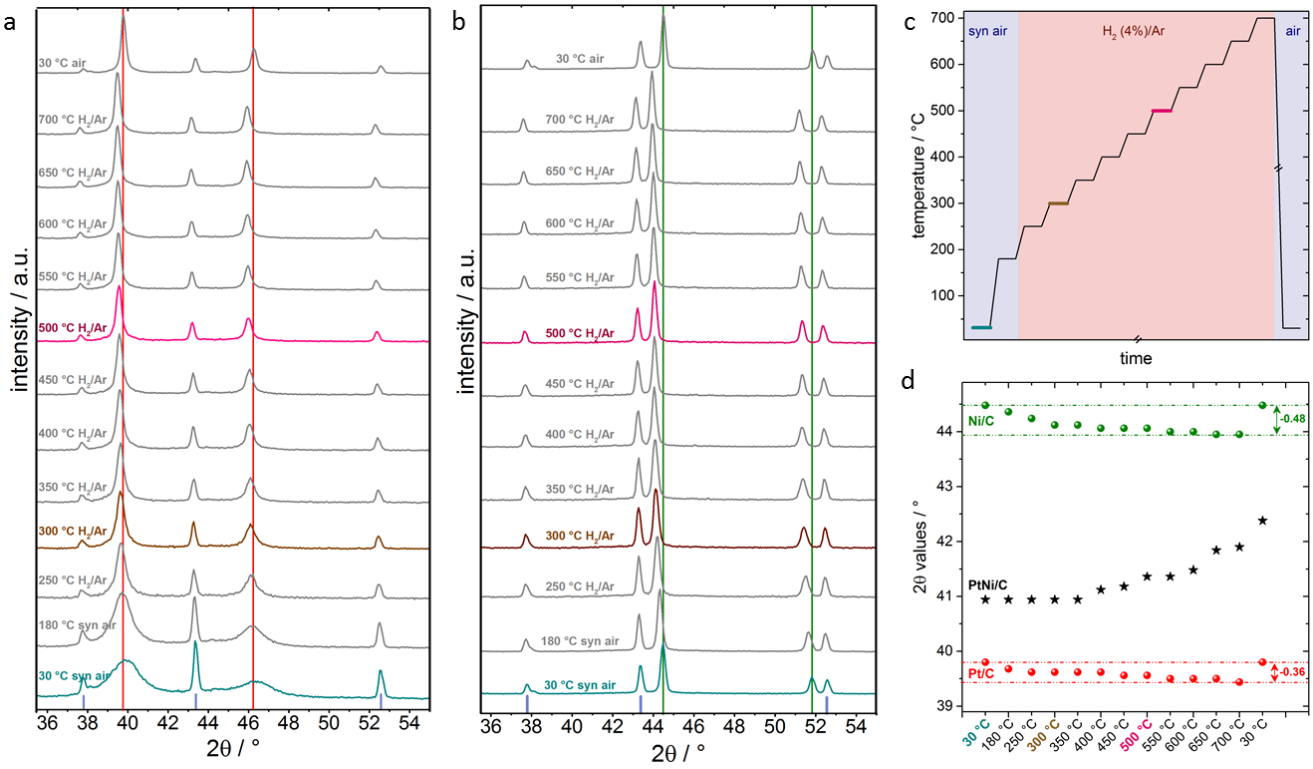

Figure S2.4 *situ* heating X-ray diffractograms of the (111) and (200) signals in the temperature range between 30 °C and 700 °C. Gas atmospheres were chosen comparably to the *ex situ* annealing conditions in the tube furnace and temperature range was chosen according to the *in situ* heating TEM experiment. **(*a*)** *in situ* heating XRD of Pt/C (fcc), **(*b*)** *in situ* heating XRD of Ni/C (fcc), red columns are assigned to pure Pt peaks, greens columns to pure Ni and blue to Al_2O_3 caused by the sample holder. **(*c*)** Temperature profile and gas atmospheres of the heating experiment; the whole *in situ* XRD experiment lasted 25 hours including delay time for purging gas and holding temperatures. ***(d)*** Shift of the (111) peak maximum with different temperatures of Pt/C (red squares), Ni/C (green squares) and Pt-Ni/C (black stars).

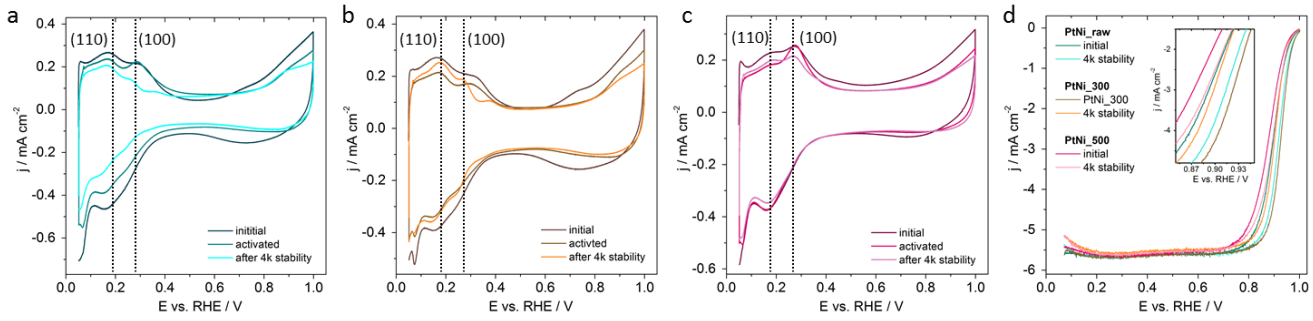

Figure S2.5 Electrochemical surface characterization and activity measurement of octahedral Pt-Ni/C; ***(a-c)*** cyclic voltammograms (CVs) with H_{upd} region after no electrochemical pre-treatment (initial), activation (activated) and 4k stability testing (4k stability); ***(d)*** linear sweep voltammetry of the three materials after activation and after 4k cycles stability test. H_{upd} CVs were measured between 0.05 and 1.0 V_{RHE} with 100 mV s^{-1} and 4k stability measurements were measured between 0.5 and 1.0 V_{RHE} with 50 mV s^{-1} in N_2 sat. 0.1 M $HClO_4$ and 0 rpm; LSVs were measured in O_2 sat. 0.1 M $HClO_4$ between 0.05 and 1.0 V_{RHE} with 5 mV s^{-1}, 1600 rpm and were iR corrected.

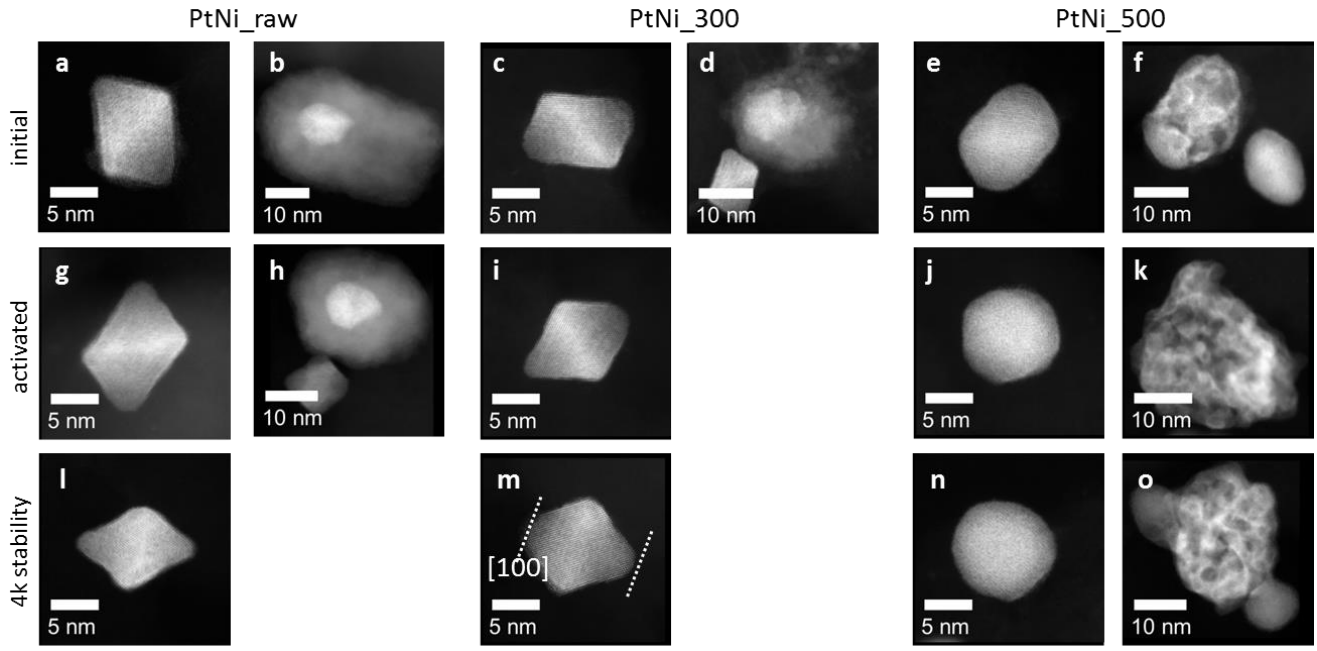

Figure S2.6 HAADF STEM images of *PtNi_raw* ***(a, b, g, h, l)***, *PtNi_300* ***(c, d, i, m)*** and *PtNi_500* ***(e, f, j, k, n, o)*** in the initial condition ***(a and b, c and d, e and f)***, after activation ***(g and h, i, j and k)*** and after 4k stability test ***(l, m, n and o)***. If present, also bigger mostly Ni-rich particles are depicted ***(b and h, d, f and k and o)***.

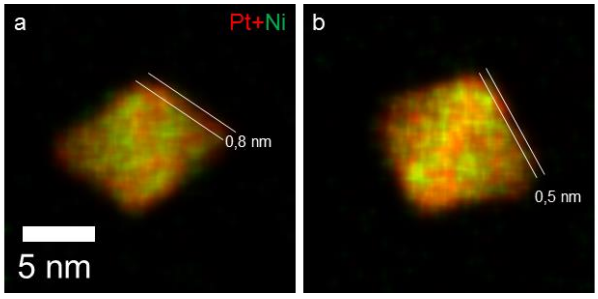

Figure S2.7 EDX elemental maps showing the composition of *PtNi_raw* **(*a*)** and *PtNi_300* **(*b*)** after 4k stability test. Pt: red and Ni: green.

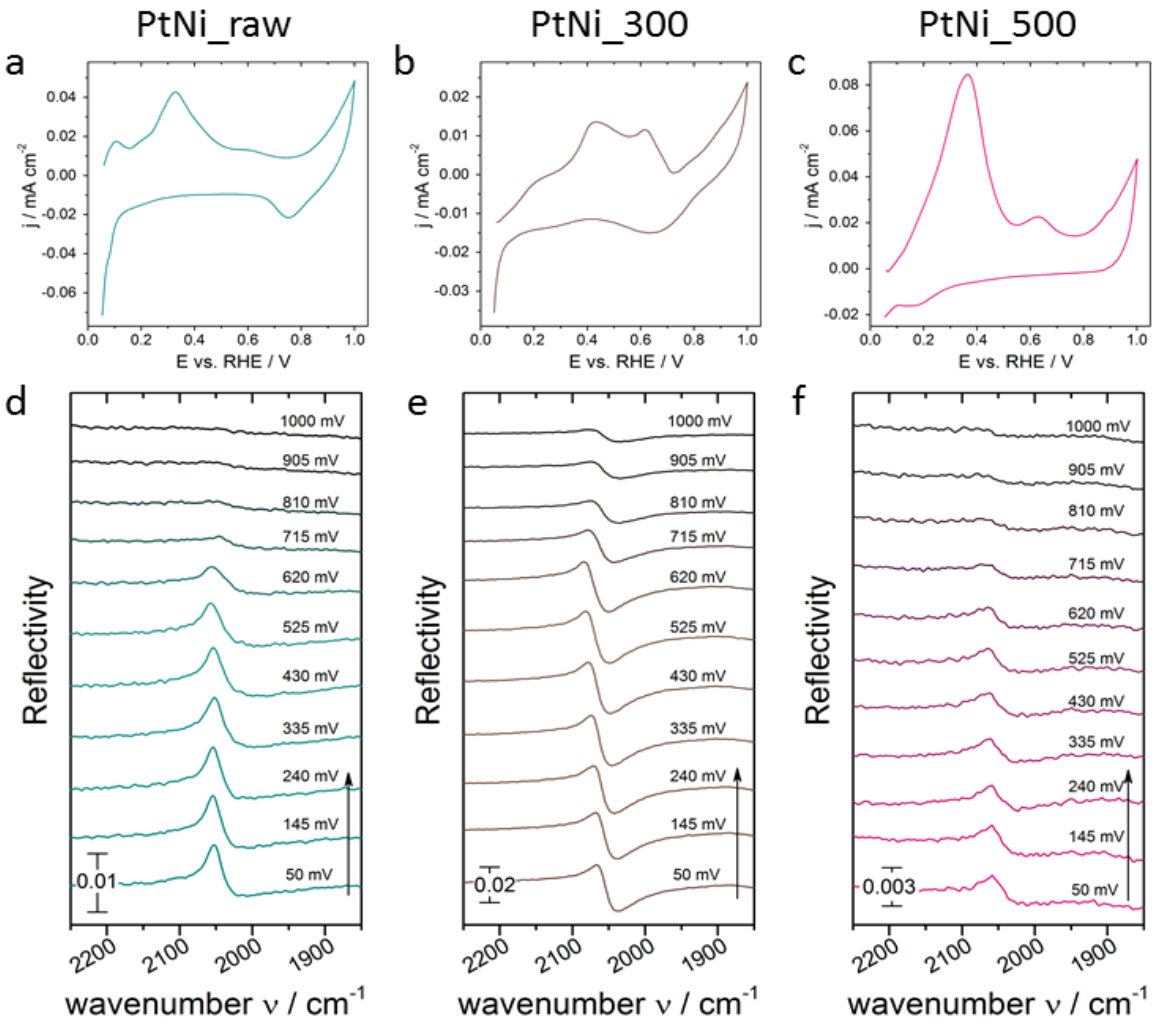

Figure S2.8 Representative sets of ATR FTIR reflectivity spectra of the catalyst surface during electrochemical CO oxidation with corresponding electrochemical curves. *PtNi_raw* ***(a, d)***, *PtNi_300* ***(b, e)*** and *PtNi_500* ***(c, f)*** are shown after electrochemical activation (20 cycles). The potential was scanned from 50 to 1000 mV_{RHE} and back (not shown) with a scan rate of 1 mV s^{-1} in 0.1 M $HClO_4$. An IR spectra is represented every 95 mV. The background spectrum was taken before adding CO at a constant potential of 50 mV_{RHE}.

An additional set of PtNi particles was synthesized as shown in Scheme S1 and tested in terms of their characteristics, comparable to the particles discussed in the main manuscript. As these samples descending from a different batch of particles than the previously discussed once, they are marked with PtNi*_raw, PtNi*_air and PtNi*_180.

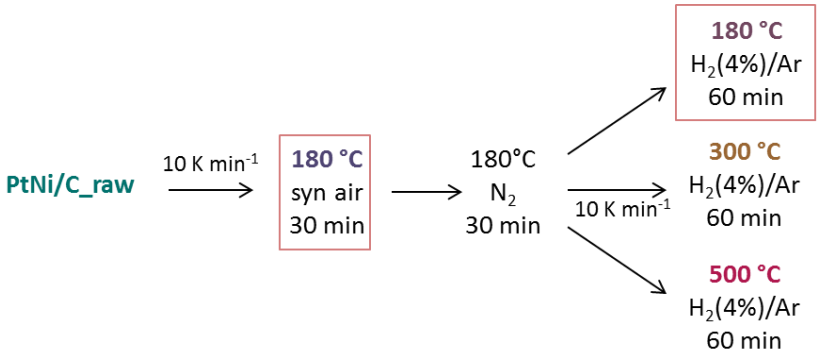

Scheme S1 Overview of post-synthesis treatments including acetic acid treatment and annealing protocols. Newly added samples are marked with red squares.

X-ray diffraction patterns show no significant change after annealing at 180 °C (Figure S9). The same is true for the electrochemical characteristics. The ORR activities and ECSA (Figure S10 a,b) values are all within the error, CO stripping profiles (Figure S10 c-e) and cyclic voltammetry (Figure S11 a-c) show no remarkable differences. We also performed FTIR spectroscopy on the three samples using CO as a surface probe molecule adsorbed on the particle surface at 50 mV_{RHE}. The CO stretching vibrations all appear at roughly the same wavenumber (Figure S12) and the corresponding *in situ* CO stripping profiles (Figure S13) show the same redox feature for all three samples.

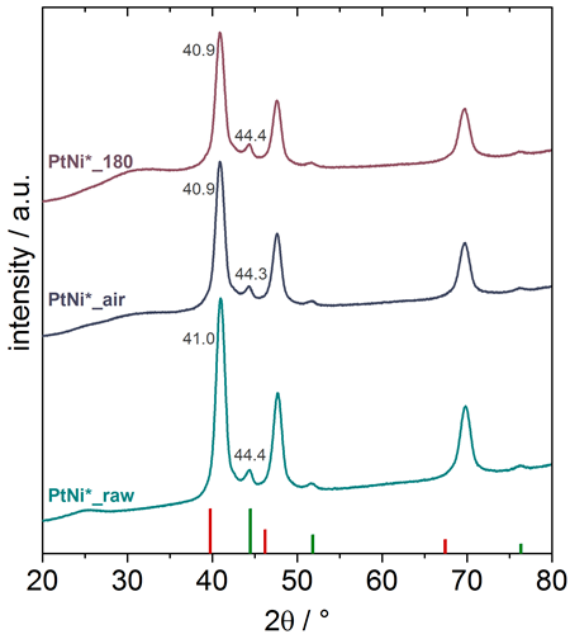

Figure S2.9 XRD pattern of *PtNi_raw*, *PtNi_180_air* and *PtNi_180*. Red columns correspond to pure Pt (PDF#00-004-0802) peaks and green columns to pure Ni (PDF#00-004-0850).

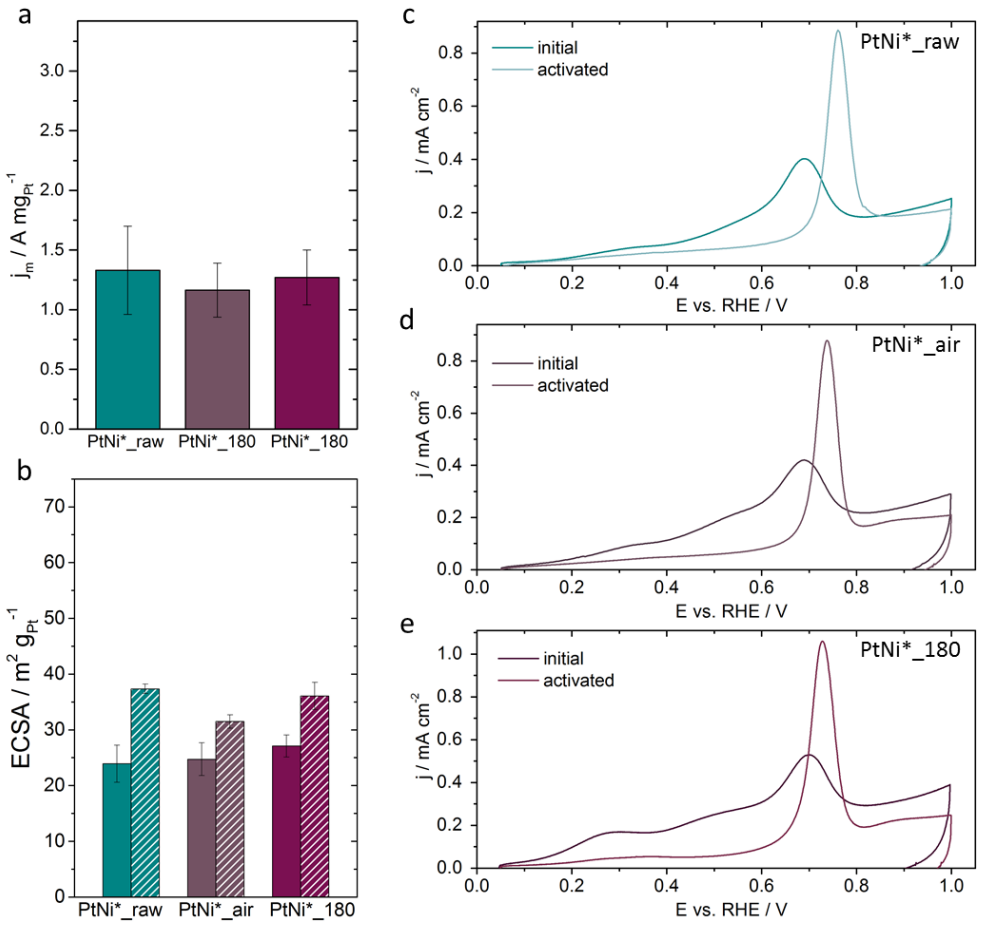

Figure S2.10 (*a*) Electrochemical ORR activity of the activated state (after 20 cyclic voltammograms (CV) activation) evaluated at 0.9 V; ORR was measured in O_2 sat. 0.1 M $HClO_4$ between 0.05 and 1.0 V_{RHE} with 5 mV s^{-1}, 1600 rpm and were iR corrected **(*b*)** Electrochemical active surface area determined by integration of the hydrogen under potential deposition region (H_{upd}) (solid colors) and the CO oxidation peak (striped colors) after activation. The error bars depicting the standard deviation between at least three different and independent measurements of freshly prepared catalyst films. **(*c-e*)** Positive CO oxidation profile of the initial samples and the activated. H_{upd} values were evaluated from CVs measured in N_2 sat. 0.1 M $HClO_4$ between 0.05 and 1.0 V_{RHE} with 100 mV s^{-1} H_{upd}, CO oxidation was performed in N_2 sat. 0.1 M $HClO_4$ between 0.05 and 1.0 V_{RHE} with 50 mV s^{-1} and 0 rpm.

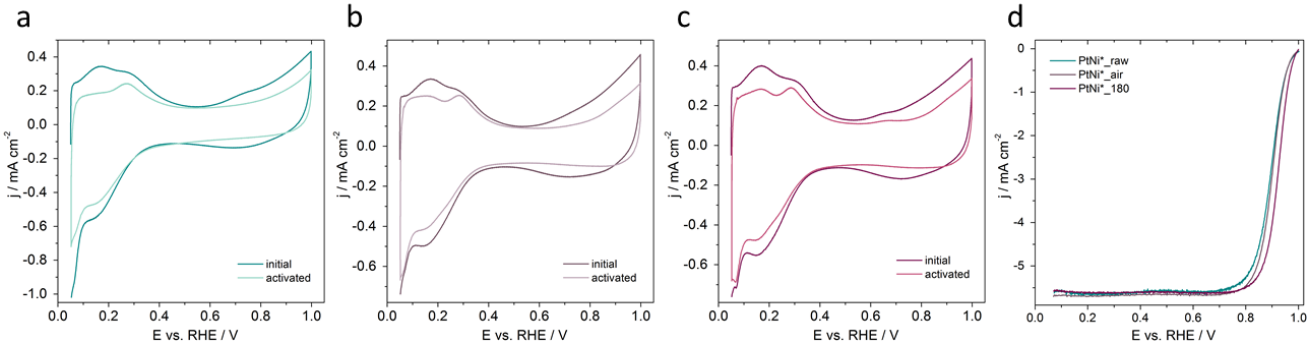

Figure S2.11 Electrochemical surface characterization and activity measurement of octahedral Pt-Ni*/C; ***(a-c)*** cyclic voltammograms (CVs) with H_{upd} region after no electrochemical pre-treatment (initial) and after activation (activated)); **(*d*)** linear sweep voltammetry of the three materials after activation. H_{upd} CVs were measured in N_2 sat. 0.1 M $HClO_4$ between 0.05 and 1.0 V_{RHE} with 100 mV s^{-1} and 0 rpm; LSVs were measured in O_2 sat. 0.1 M $HClO_4$ between 0.05 and 1.0 V_{RHE} with 5 mV s^{-1}, 1600 rpm and were iR corrected.

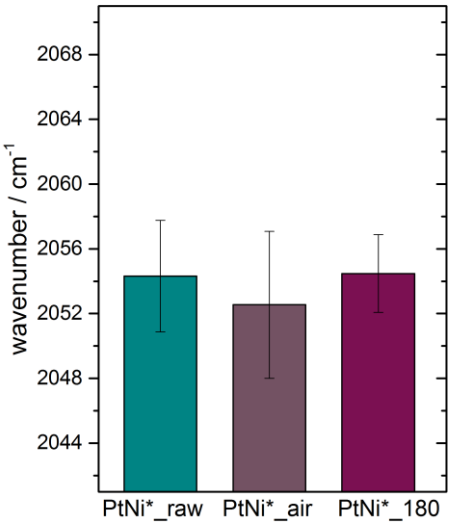

Figure S2.12 *In situ* FTIR spectroscopy measured in ATR mode showing the position of CO_{ad} band of the linear bounded CO collected at 50 mV_{RHE} in N_2 sat. 0.1 M $HClO_4$ for the different samples after electrochemical activation. The error bars depicting the standard deviation between at least three different and independent measurements of freshly prepared catalyst films.

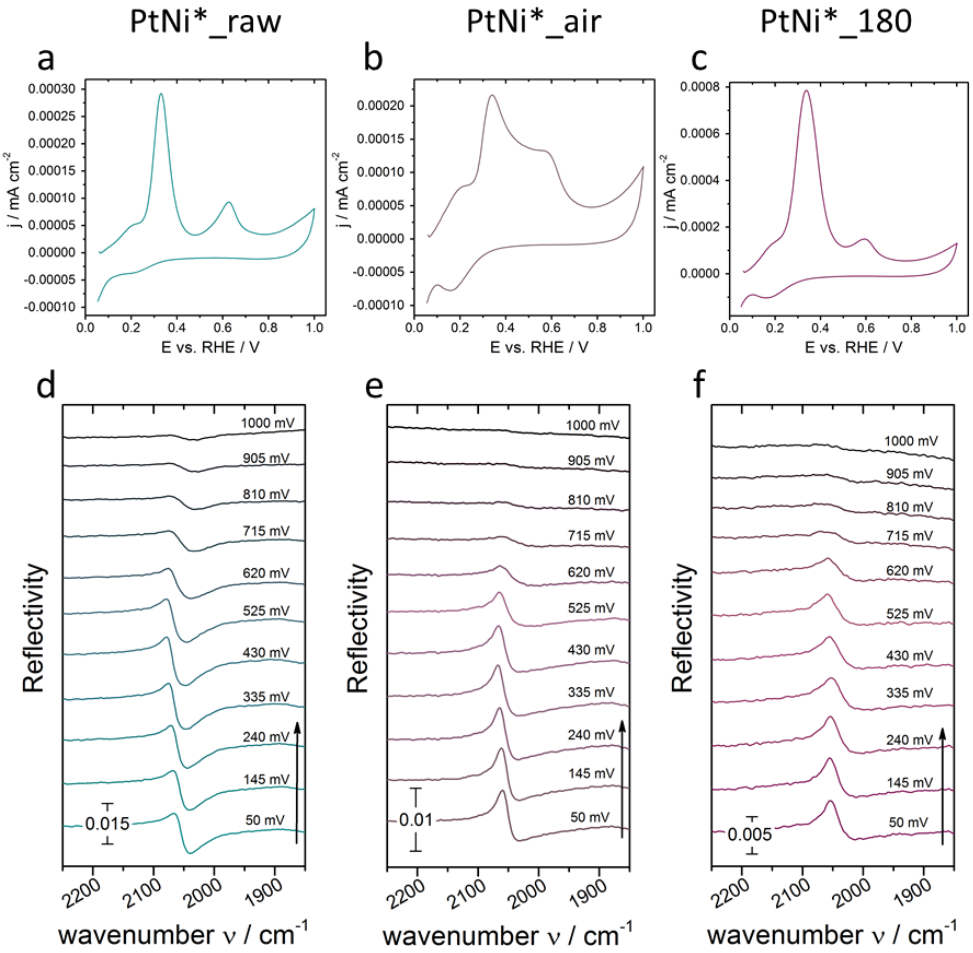

Figure S2.13 Representative sets of ATR FTIR reflectivity spectra of the catalyst surface during electrochemical CO oxidation with corresponding electrochemical curves. *PtNi*_raw* ***(a, d)***, *PtNi*_air* ***(b, e)*** and *PtNi*_180* ***(c, f)*** are shown after electrochemical activation (20 cycles). The potential was scanned from 50 to 1000 mV_{RHE} and back (not shown) with a scan rate of 1 mV s^{-1} in 0.1 M $HClO_4$. An IR spectra is represented every 95 mV. The background spectrum was taken before adding CO at a constant potential of 50 mV_{RHE}.

Figure S2.14 and Figure S2.15 show high angle annular dark field (HAADF) STEM images of PtNi* nanoparticles in different states and the corresponding EDX composition maps.

For the octahedral PtNi*_raw nanoparticle, oriented close to the ⟨110⟩ zone axis, the EDX map indicates an enrichment of Ni at the ⟨111⟩ facets, a Pt-rich frame, which is pointed out by a Pt-rich strip in the middle of the nanoparticle, and a Ni rich shell surrounding the octahedral nanoparticle (Figure S2.14c). EDX quantification yields an average composition of Pt 52 at.% and Ni 48 at.% for particles in the initial state. However, for the PtNi*_180 and PtNi*_air particles no significant difference in the elemental distribution nor in the composition. For PtNi*_180 the average composition is Pt 52 at.%, Ni 48 at.% and for PtNi*_air Pt 48 at.%, Ni 52 at.%, respectively.

After activation, EDX quantification yields an average composition of Pt 69 at.% and Ni 31 at.% for PtNi*_raw, Pt 72 at.% and Ni 28 at.% for PtNi*_180 and an average composition of Pt 68 at.%, Ni 32 at.% for PtNi*_air after 20 CV (Figure S2.15). Thus Ni dissolution is visible after electrochemical cycling in acidic solution. For PtNi*_raw, PtNi*_180 and PtNi*_air the EDX maps indicate the removal of the former Ni rich shell. Further in the EDX maps a thin Pt layer is observed at the outermost parts of the octahedra, which might be due to the presence of Pt-rich edges or the formation of a thin Pt-rich skin on the facets of the octahedra. Hence, also here no significant change for PtNi*_raw, PtNi*_180 and PtNi*_air in elemental distribution and composition is visible.

In addition to the octahedral nanoparticles, again bigger irregular-shaped nanoparticles are observed (Figure S2.14 d,e, i, j, n, o andFigure S2.15 d,e, i, j, n, o). The irregular-shaped nanoparticles consist always of a Pt rich nanoparticle which is encased by Ni. The overall average composition of the bigger nanoparticles is Pt 3 at.%, Ni 97 at.% for PtNi*_raw, PtNi*_180 and PtNi*_air. After 20 CV the bigger irregular nanoparticles are also found with no significant changes in composition and elemental distribution.

Thus, the 180 °C air annealed and 180 °C H_2/Ar annealed samples exhibit the same characteristics like the as prepared sample. Accordingly, PtNi_raw is suitable to be discussed as starting material for this study.

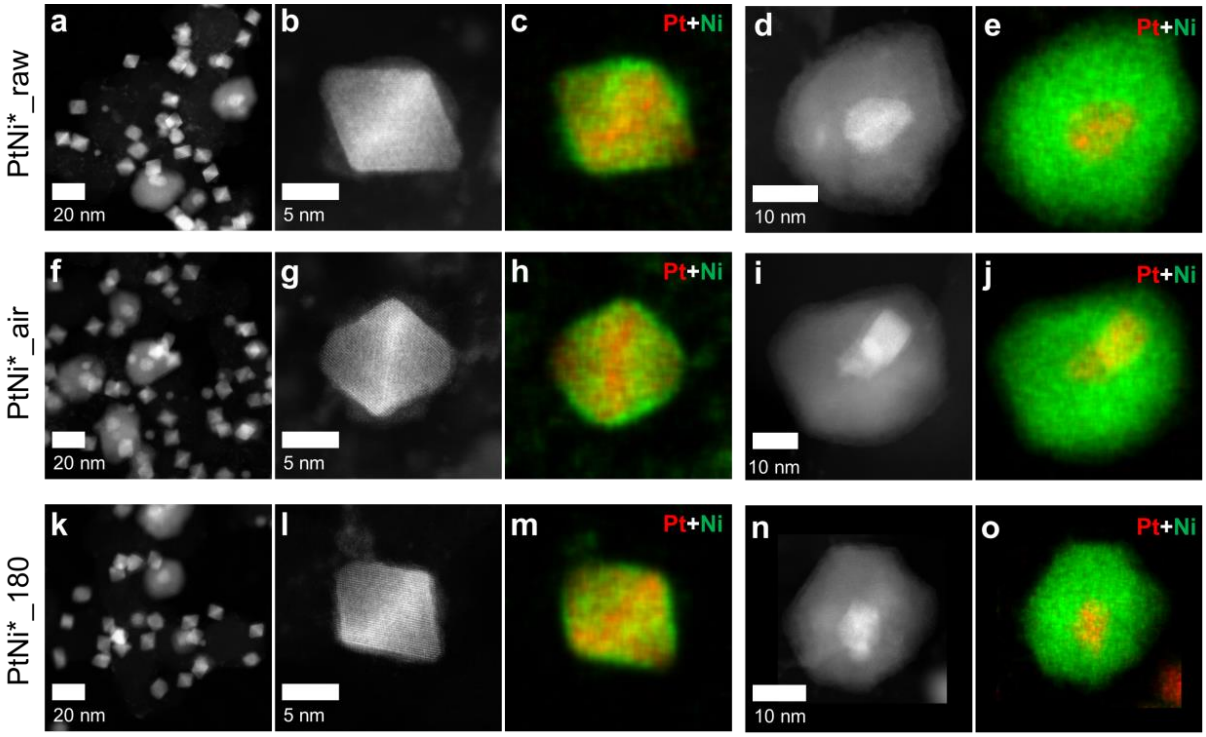

Figure S2.14 HAADF images and EDX elemental maps of the *initial PtNi*_raw* ***(a-e)***, *PtNi*_air* ***(f-j)*** and *PtNi*_180* ***(k-o)***. Octahedral and big irregular shaped Ni-rich particles are shown. Pt: red and Ni: green. Particle shape and size and elemental distribution show no remarkable difference between the samples. All samples are also comparable to PtNi_raw discussed in the main manuscript.

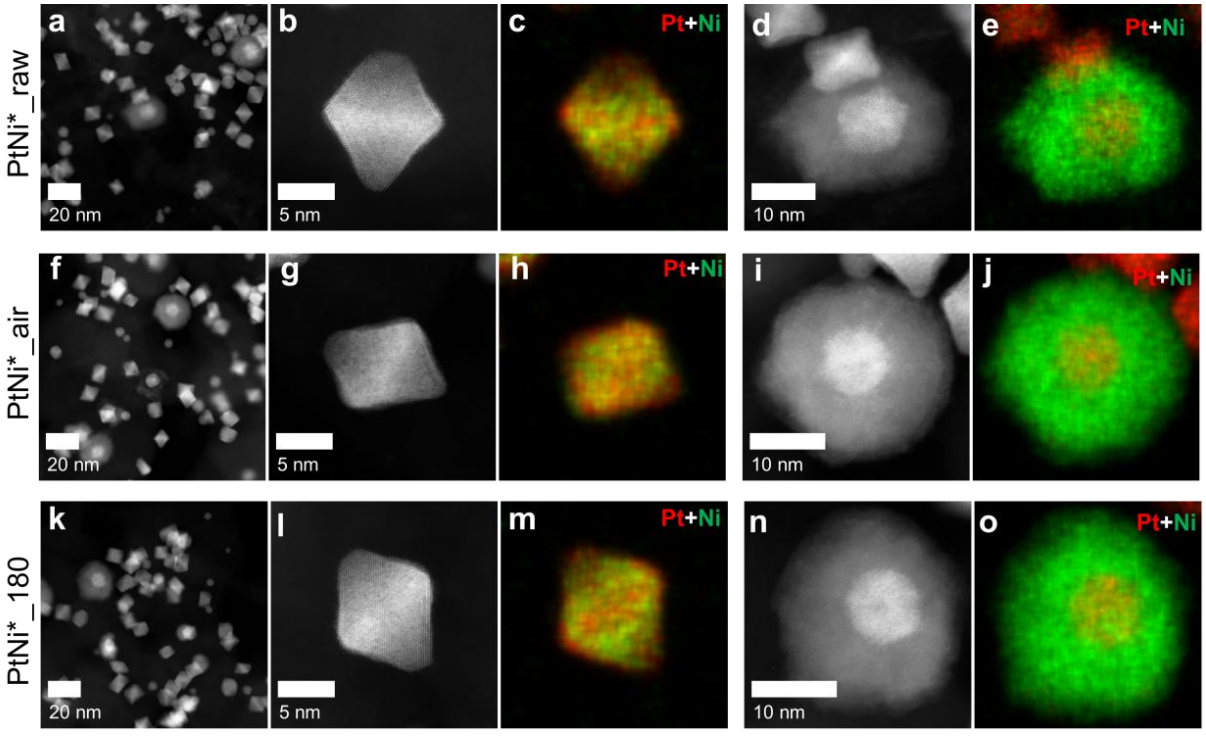

Figure S2.15 HAADF images and EDX elemental maps of the *activated PtNi*_raw* ***(a-e)***, *PtNi*_air* ***(f-j)*** and *PtNi*_180* ***(k-o)***. Octahedral and big irregular shaped Ni-rich particles are shown. Pt: red and Ni: green. Particle shape and size and elemental distribution show no remarkable difference between the samples. All samples are also comparable to PtNi_raw discussed in the main manuscript.

A3 Supplementary Information to Chapter 6

Tuning the Catalytic Oxygen Reduction Reaction Performance of Pt-Ni Octahedral Nanoparticles by Acid Treatments and Thermal Annealing

Reproduced from J. Electrochem. Soc. **2018***, 165(15), J3026-J3030 (Reference* [146]*).* This paper is part if the JES Focus Issue on Electrocatalysis – In Honor of Radislav Adzic, *Open access.*

Details to Rietveld Refinement:

Background: Chebychev with 5 polynomial coefficients

Phases:

- Two Pt fcc with Pt and Ni sites – Pt & Ni occupancy was applied according to composition 0.7 and 0.3, respectively
  - Both with preferred orientation in (111) and (200) required
- Graphite with additional peak phase at 24.98°2θ to subtract carbon support or influence of holder

Table S3.1 Phase composition as obtained by Rietveld refinement of XRD pattern – values given in weight%.

Sample	Pt-Ni phase 1	Pt-Ni phase 2	Ni phase
Initial Pt-Ni[132]	*64.5*	*6.0*	*29.5*
HAc	60.0	40.0	-
HAc_300	63.6	36.4	-
HAc_500	82.4	17.6	-

Table S3.2 Structural parameters obtained by Rietveld refinement of XRD pattern.

Sample	Pt-Ni phase 1			Pt-Ni phase 2			Rwp
	a / Å	LVol-IB / nm	e0	a / Å	LVol-IB / nm	e0	
HAc	3.7758(42)	8.32(61)	0	3.7889(44)	3.11(37)	0.36(14)	0.99
HAc_300	3.7817(23)	8.712(80)	0.008(12)	3.7963(24)	3.83(74)	0.64(15)	0.86
HAc_500	3.7803(23)	9.769(74)	0.1066(60)	3.7956(26)	3.38(19)	0.10(12)	0.98

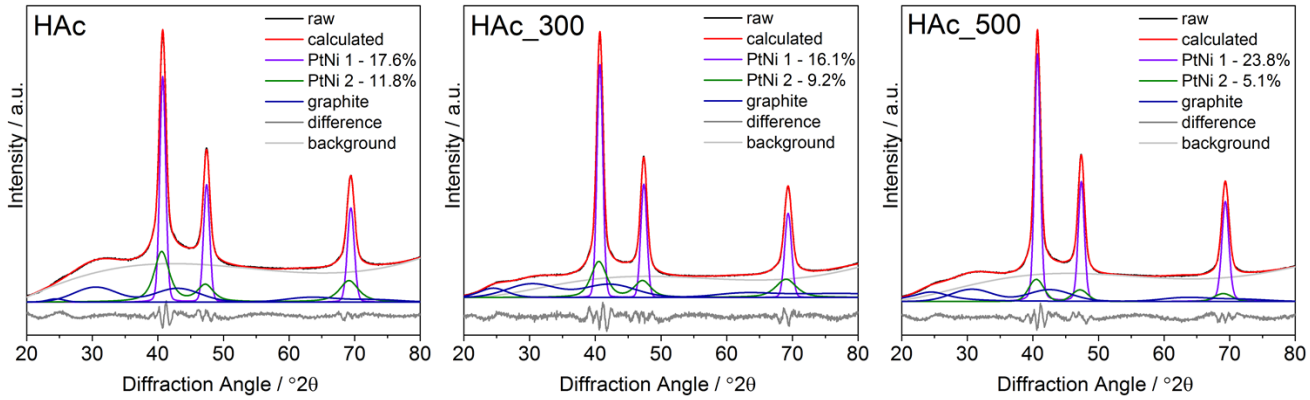

Figure S3.1 Rietveld refinement results of sample series.

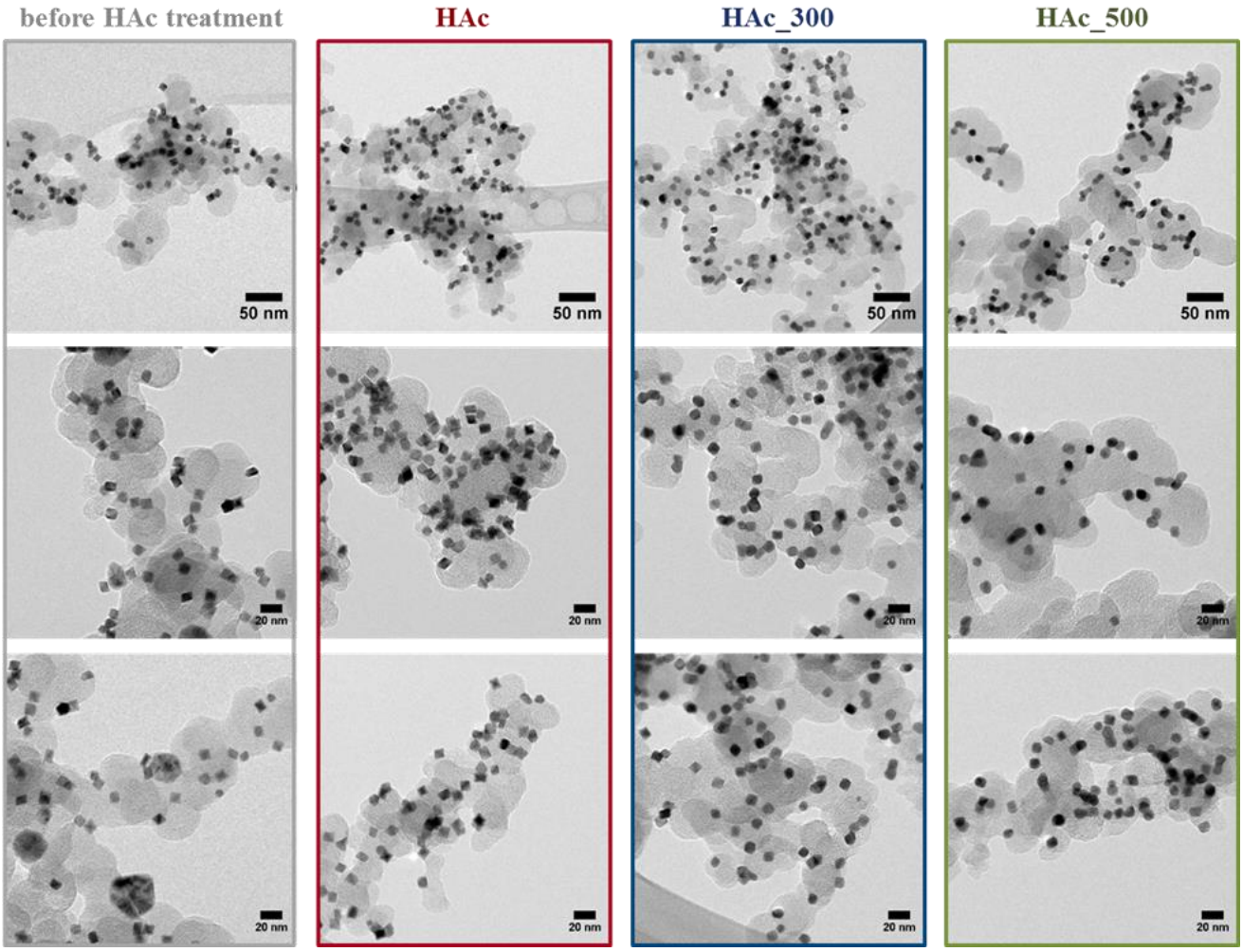

Figure S3.2 TEM images of the Pt-Ni/C samples as received (left column), i.e. before acetic acid treatment and annealing, and after post synthesis treatments HAc (2nd column), HAc_300 (3rd column) and HAc_500 (right column) in different magnifications.

A4 Supplementary Information to Chapter 7

Real-time Imaging of Activation and Degradation of Octahedral Pt-Ni Fuel Cell Catalysts at the Nanoscale

Chapter 7 and Appendix A4 Supplementary Information to Chapter 7 are reproduce from a manuscript submitted to the Nature Publishing group.

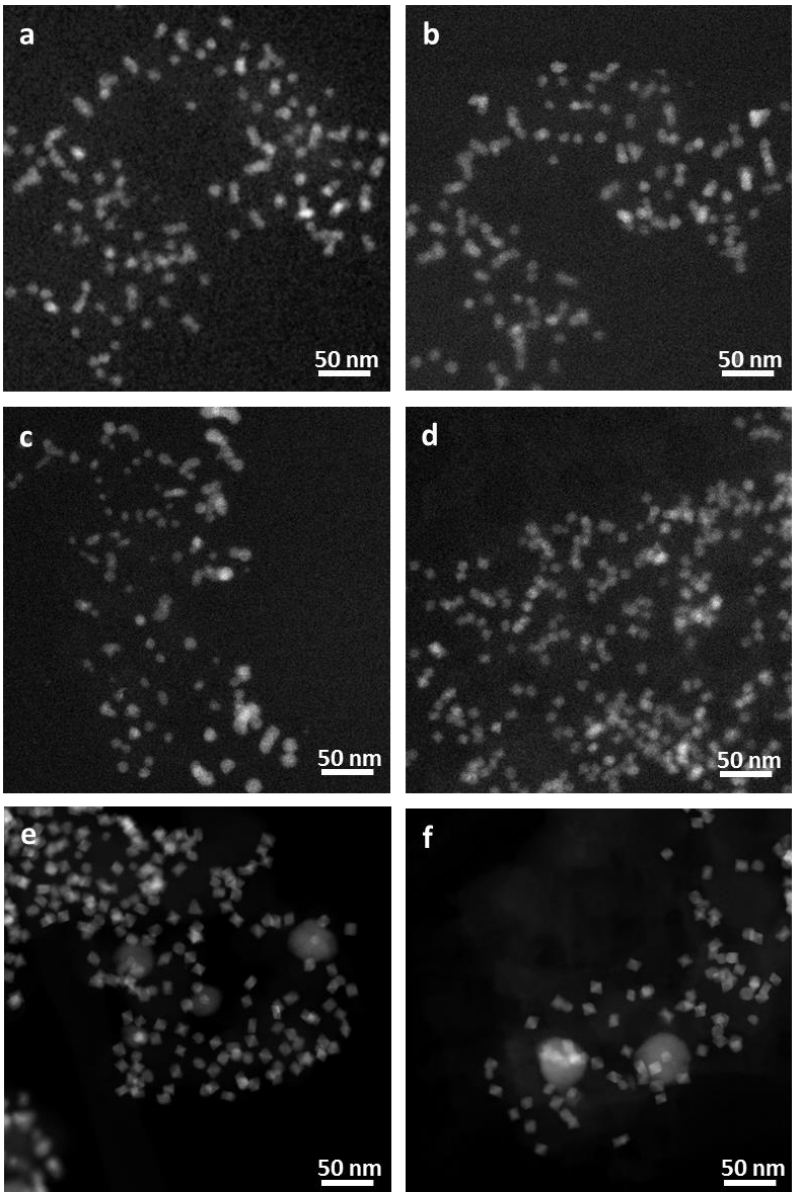

Figure S4.1 Comparisons of shape change with and without the electron beam. HAADF STEM images of particles before **a)** and after **b)** *in situ* cycling from 0 to +1.2 V_{RHE} with continual imaging. The carbon support bends during cycling and there is some coalescence leading to octahedral shape degradation. Images of the particles which are on **c)** and off **d)** the electrode in the *in situ* cell after cycling where neither region was exposed to the electron beam. Particles on the electrode show rounded surfaces and appear to be larger. Particles off the electrode maintain their octahedral shape and size. From this, we conclude that there were electrochemical effects on the particles on the electrode that cannot be accounted for by the electron beam or exposure to electrolyte alone. HAADF STEM images of the *ex situ* particles in an aberration corrected STEM before **e)** and after **f)** the same electrochemical procedure, showing significantly less shape change than the *in situ* experiment, although some shape change is observed.

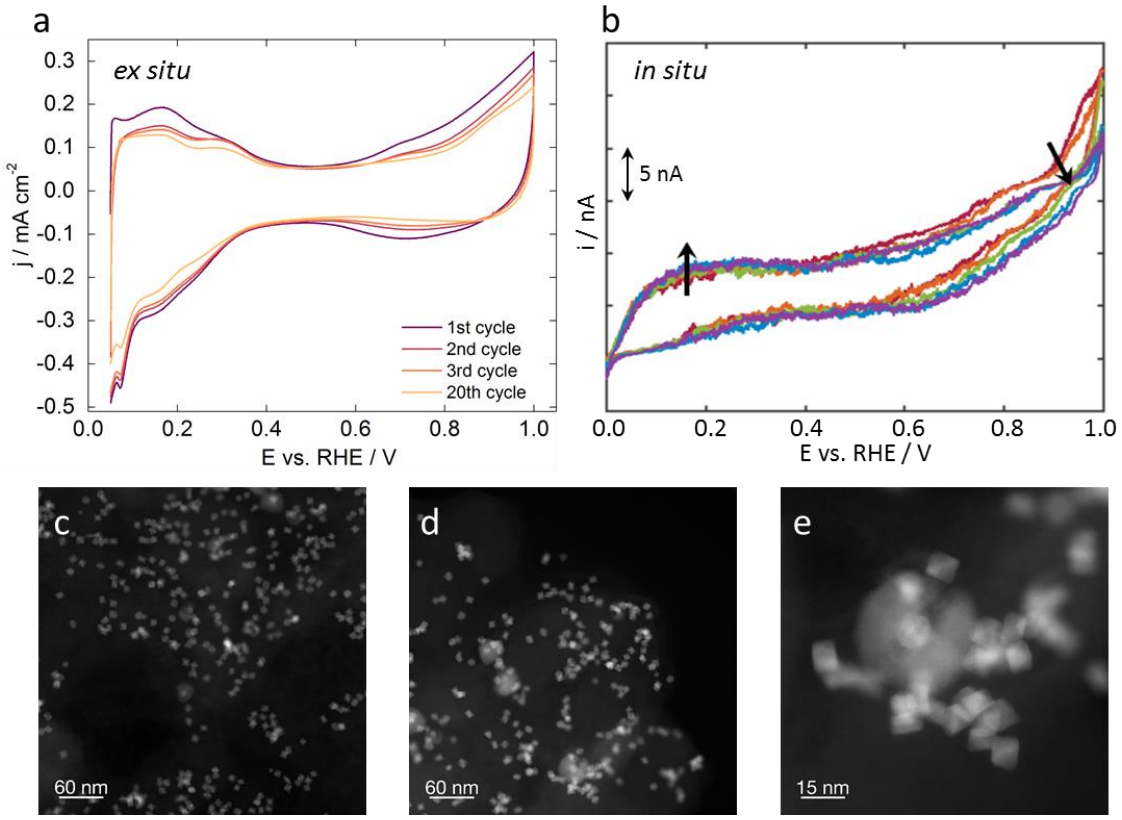

Figure S4.2 *Ex situ* electrochemical data measured in a three electrode RDE setup between **a)** 0.05 – 1.0 V_{RHE}, 20 (+5) cycles, 100 mV s^{-1}, N_2 sat. 0.1 M $HClO_4$); **b)** *In situ* electrochemical data measured in the protochips electrochemistry TEM holder (-0.8 – 0.2 V_{Pt}, 40 (+5) cycles, 100 mV s^{-1}, 0.1 M $HClO_4$); **c-d)** HAADF images of the catalyst after similar *ex situ* electrochemical treatment. Ni-rich particles remain (as shown in d,e) but some show signs of the beginning of the dissolution process observed *in situ*. In these images, the octahedral shape of the Pt-Ni nanoparticles remains.

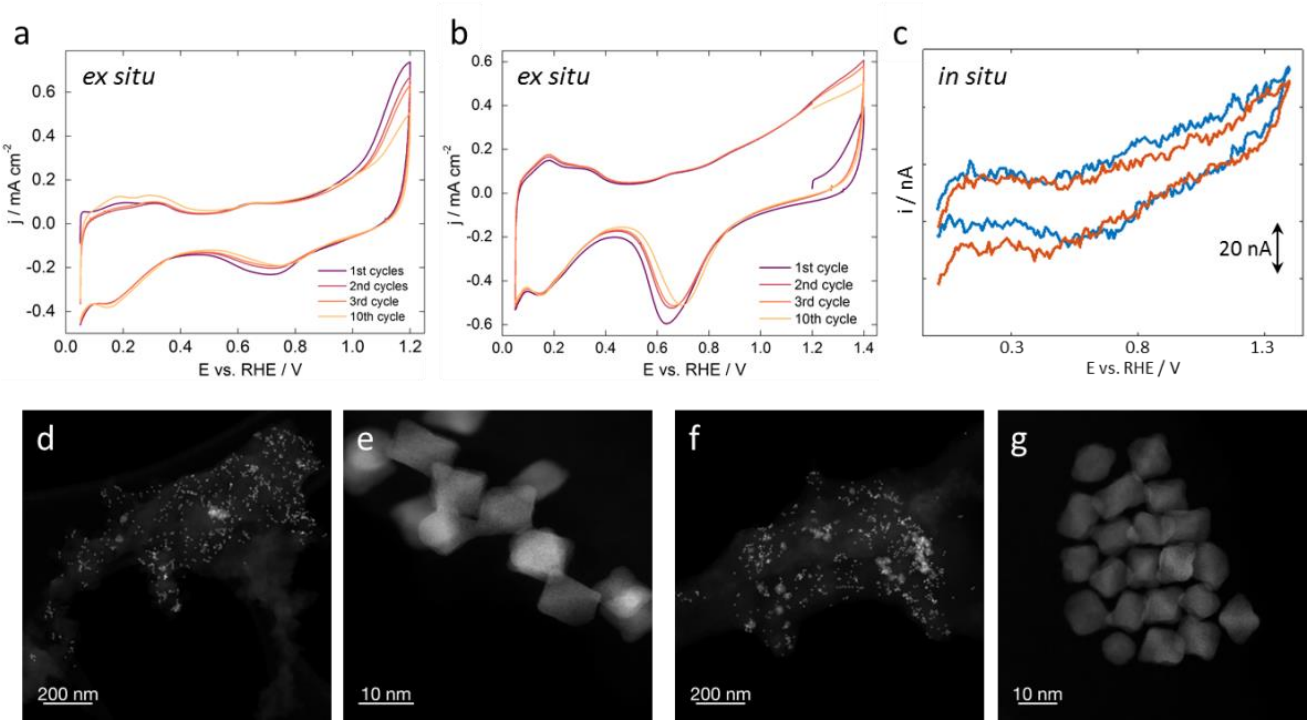

Figure S4.3 *Ex situ* electrochemical data measured in a three electrode RDE setup between **a)** 0.05 – 1.2 V_{RHE} and **b)** 0.05 – 1.4 V_{RHE}, 10 cycles, 100 mV s^{-1}, N_2 sat. 0.1 M $HClO_4$; **c** *In situ* electrochemical data measured in the protochips electrochemistry TEM holder (-0.8 – 0.6 V_{Pt}, 10 cycles, 100 mV s^{-1}, 0.1 M $HClO_4$); **d,e)** HAADF images of the catalyst after *ex situ* electrochemical treatmed between 0.05 – 1.2 V_{RHE}; particle facets remain but may be beginning to soften **f,g)** HAADF images of the catalyst after *ex situ* electrochemical treatmed between 0.05 – 1.4 V_{RHE}; faces of the particle are pulling in and the corners are more rounded. However, in both of these images, the particle shape hasn't changed as drastically as it did in the corresponding *in situ* experiment.

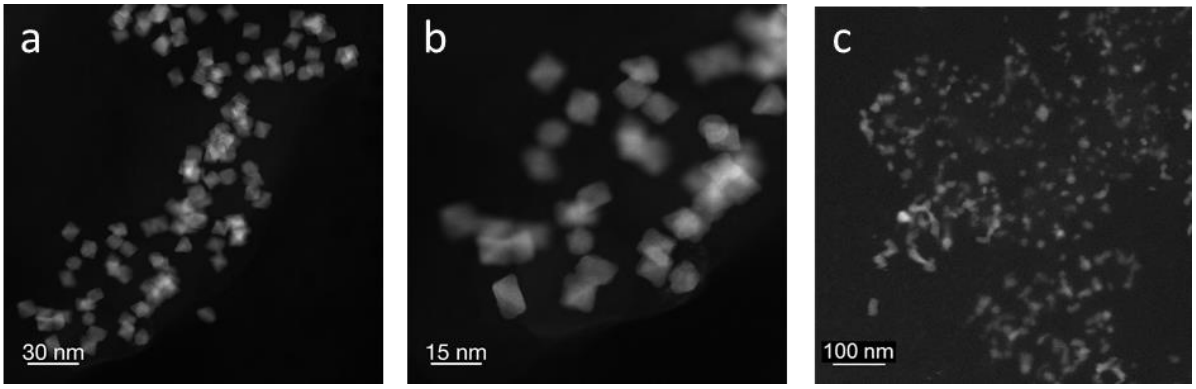

Figure S4.4 *Ex situ* HAADF STEM images. **a, b)** HAADF STEM images of the catalyst after *ex situ* electrochemical treatment for 20 cycles and subsequent step into high potential of +1.4 V_{RHE} (100 mV s^{-1}, 0.05 – 1.2 V_{RHE}). The octahedral shape remains, and the particles do not show strong coalescence. **c)** Image from the *in situ* cell, on other areas of the electrode which were not imaged during cycling, showing similar coarsening effects that were observed in the *in situ* imaged region.

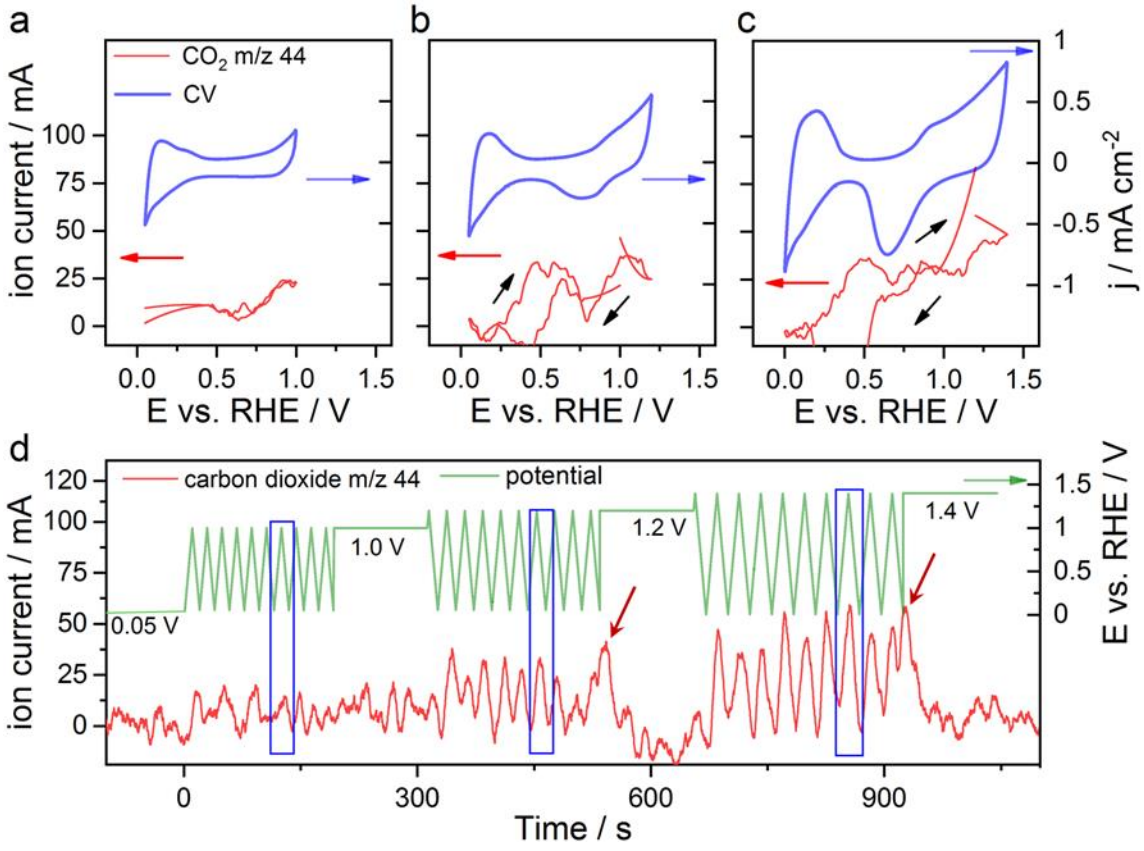

Figure S4.5 Simultaneously recorded of cyclic voltammograms (CV) and mass spectrometry cycle voltammograms (MSCV) during anodic potential step at dual thin-layer flow cell. a-c) Ion current for carbon dioxide (m/z 44) evolution over electrochemical potential (V_{RHE}) at left side and the corresponding measured current densities normalized to the electrode area on the right side. R and blue arrows indicate the axis, black arrow the scan direction. **d)** Variation of mass spectrum signal intensity m/z 44 over experimental time for each set of CVs and constant potential step shown on the left side and the corresponding potential shown on the right side, blue boxes indicate the region which were used to extract a-c. The electrochemical CVs on Pt-Ni/C was recorded in Ar sat. 0.1 M $HClO_4$ with 100mV s^{-1}. Measurements were done without any uncompensated ohmic resistance determined by electrochemical impedance spectroscopy. Green arrow indicate the axis.

Figure S4.5 represents detailed results from our Differential Electrochemical Mass Spectrocopy (DEMS) measurements. Figure S4.5a-c shows examples of the cyclic voltammograms with different upper potentials and the corresponding ion currents for carbon dioxide (CO_2). When cycling up to 1.0 V_{RHE} (Figure S4.5a) CO_2 was detected at a very low level which nearly equals the noise level and is still within the sensitivity of the mass spectra in the ppm range. Applying an upper potential of 1.2 V_{RHE} (Figure S4.5b) the values of the resulting ion currents nearly double, indicating an increased formation CO_2. At upper potentials of 1.4 V_{RHE} CO_2 shows an enormous increase in ion current intensity. From that we conclude, that potentials of 1.2 and 1.4 V_{RHE} cause carbon corrosion, which of course is more severe at 1.4 V_{RHE}.

Figure S4.5d presents the variation of the mass spectrum signal during the overall applied potential sequence with the corresponding potentials as function of time. During hold at 0.05 V_{RHE} the ion current stays at noise level until cycling up to 1.2 V_{RHE} starts. When cycling up to 1.2 V_{RHE} the ion current nicely follows the changes in potential, indicating an increase in CO_2 production during anodic scans. When changing to a constant potential

of 1.2 V_{RHE} a sudden increase of the CO_2 signal (highlighted by the red arrow) can be observed, which is in excellent agreement with our findings from Figure 7.3d,e and Movie S2. During hold at 1.2 V_{RHE} the CO_2 signal goes back to noise level again, indicating no further carbon corrosion. Cycling up to 1.4 V_{RHE} shows a nice connection between the potential and the ion current of both molecules again. In comparison to the previous one, the ion current intensity is higher, indicating a larger amount of CO_2 production and thus a higher degree of carbon corrosion, which is consistent with our discussion on the TEM movies (severe changes described for Figure 7.3h,i). Hold at 1.4 V_{RHE} causes again an increase in the CO_2 signal even though it is not as pronounced as for the hold at 1.2 V_{RHE}. For both transition to the constant potential hold however, the CO_2 signal goes back to static condition i.e. noise level. Again, this indicates and supports our statement from before, that most severe changes happening during the transition to a constant potential and that the constant potential itself does induce major changes in the catalyst.

Movie S1

HAADF STEM Movie of catalyst structure during electrochemical potential cycling between 0.0 and +1.0 V_{RHE} in 0.1 M $HClO_4$ for 20 CV with 100 mV s^{-1} sweep rate and the corresponding animated potential profile over time.

Movie S2

HAADF STEM Movie of the impact on the catalyst structure of an electrochemical sequence consisting of electrochemical potential cycling between 0.0 to +1.2 V_{RHE} and 0.0 to +1.4 V_{RHE} for 10 CV with 100 mV s^{-1} and holding on different upper potentials in 0.1 M $HClO_4$ and the corresponding animated potential profile over time.

Movie S3

HAADF STEM Movie imaging of the catalyst structure during electrochemical potential cycling between 0.0 and +1.2 V_{RHE} for 20 CV with 100 mV s^{-1} sweep rate, followed by a step into a high potential and the corresponding animated potential profile over time.

List of Abbreviations

AFC	Alkaline fuel cell	HOR	Hydrogen oxidation reaction
atm	atmospheres	HT XRD	High temperature X-ray diffraction
BF	Bright field	H_{UPD}	Hydrogen underpotential deposition
CCD	Charge-coupled device	ICP OES	Inductively Coupled Plasma Optical Emission Spectrometry
CE	Counter electrode	IR	Infra-red
CV	Cyclic voltammetry	LSV	Linear sweep voltammertry
DEMS	Differential electrochemical mass spectrometry	MCFC	Molten carbonate fuel cell
DF	Dark field	MCT	Mercury cadmium telluride
DFT	Density functional theory	MEA	Membrane electrode assembly
DOE	Department of energy	min	minutes
ECSA	Electrochemical active surface area	MMS	Mercury mercury-sulfate
E_d	d-band center	ORR	Oxygen reduction reaction
EDX	Energy dispersive X-ray spectroscopy	PEIS	Potentiostatic electrochemical impedance spectroscopy
EELS	Electron energy loss spectrocopy	PEM	Polymer electrolyte membrane
E_f	Fermi level	PGM	Platinum group metal
fcc	Face centered cubic	RDE	Rotation disc electrode
FTIR	Fourier transformed infra-red	RT	Room temperature
GC	Glassy carbon	WE	Working electrode
HAADF	High angle annular dark field	XRD	X-ray diffraction
hkl	Miller indices		

List of Chemicals

Name	Acronym	Purity/Concentration	Supplier
1,2-Tetradecanediol	-	90.0 %	Sigma Aldrich
1-Octadecene	-	90.0 %	Alfa Aesar
Acetic acid	HAc	≥ 99.9 %	Sigma Aldrich
Carbon monoxide	CO	99.997 %	Air Liquide
Cetyltrimethylmmonium bromide	CTAB	-	Alfa Aesar
Dibenzylether	Bn_2O	98.0 %	Fluka
Dichlormethan	DCM	-	Sigma Aldrich
Ethanol	EtOH	100 %	VWR Chemicals
Hydrochloric acid	HCl	37.0 %	VWR Chemicals
Hydrogen	H_2	99.999 %	Air Liquide
Isopropanol	iPrOH	100 %	VWR Chemicals
Methanol	MeOH	anhydrous, 99.9 %	Alfa Aesar
n-Hexane	-	99.0 %	Alfa Aesar
Nafion	-	5 wt%	Sigma Aldrich
Nickel(II) acetylacetonate	$Ni(acac)_2$	95.0 %	Alfa Aesar
Nickel chloride hexahydrate	$NiCl_2 \cdot 6H_2O$	99.5 %	Sigma Aldrich
Nitric acid	HNO_3	69.0 %	Merck
Nitrogen	N_2	99.999 %	Air Liquide
Oleic acid	OAc	90.0%	Alfa Aesar
Oleylamine	OAm	70.0 %	Sigma Aldrich
Oxygen	O_2	99.998 %	Air Liquide
Perchloric acid	$HClO_4$	70 % conc., 99.999 % trace metal bases	Sigma Aldrich
Platinum(II) acetylacetonate	$Pt(acac)_2$	Pt 48 % min.	Alfa Aesar
Rhodium(III) acetylacetonate	$Rh(acac)_3$	97.0 %	Sigma Aldrich
Sodium oleate	-	≥82.0 % fatty acids	Sigma Aldrich
Sulfuric acid	H_2SO_4	95.0 %	VWR Chemicals
Toluene	-	99.8 %	Roth
Tungsten hexacarbonyl	$W(CO)_6$	97.0 %	Alfa Aesar
Ultra-pure water	Milli-Q water	16.8 MΩ cm	-

List of Figures and Schemes

List of Tables

List of Publications

Accepted manuscripts, which are part of this thesis and link to the final versions:

V. Beermann, M. Gocyla, E. Willinger, S. Rudi, M. Heggen, R. E. Dunin-Borkowski, M.-G. Willinger, P. Strasser, "Rh-doped Pt-Ni octahedral nanoparticles: understanding the correlation between elemental distribution, ORR and shape stability", Nanoletters **2016**, 16 (3), 1719-1725, DOI: 10.1021/acs.nanolett.5b04636 (https://pubs.acs.org/doi/abs/10.1021/acs.nanolett.5b04636)

V. Beermann, M. Gocyla, S. Kühl, E. Padgett, H. Schmies, M. Goerlin, N. Erini, M. Shviro, M. Heggen, R. E. Dunin-Borkowski, D. A. Muller, P. Strasser, "*Tuning the Electrocatalytic Oxygen Reduction Reaction Activity and Stability of Shape-Controlled Pt–Ni Nanoparticles by Thermal Annealing − Elucidating the Surface Atomic Structural and Compositional Changes*" JACS **2017**, 139 (46), 16536–16547, DOI: 10.1021/jacs.7b06846 (https://pubs.acs.org/doi/10.1021/jacs.7b06846)

V. Beermann, S. Kühl, P. Strasser, *"Tuning the Catalytic Oxygen Reduction Reaction Performance of Pt-Ni Octahedral Nanoparticles by Acid Treatments and Thermal Annealing*", Journal of The Electrochemical Society **2018***,* 165(15), *J3026-J3030,* DOI: 10.1149/2.0051815jes (http://jes.ecsdl.org/content/165/15/J3026.full) Open access article distributed under the terms of the Creative Commons Attribution 4.0 License (CC BY).

Other accepted manuscripts:

N. Erini, S. Rudi, V. Beermann, P. Krause, R. Yang, Y. Huang, P. Strasser; "*Exceptional Activity of a Pt–Rh–Ni Ternary Nanostructured Catalyst for the Electrochemical Oxidation of Ethanol*", ChemElectroChem **2015**, 2, 903-908; DOI: 10.1002/celc.201402390

N. Erini, V. Beermann, M. Gocyla, M. Gliech, M. Heggen, R. E. Dunin-Borkowski, P. Strasser, "*The Effect of Surface Site Ensembles on the Activity and Selectivity of Ethanol Electrooxidation by Octahedral PtNiRh Nanoparticles*", Angewandte Chemie **2017**, 56, 653-6538, DOI: 10.1002/anie.201702332

S. Rudi, D. Teschner, V. Beermann, W. Hetaba, L. Gan, C. Cui, M. Gliech, R. Schlögl, P. Strasser, "*pH-Induced versus Oxygen-Induced Surface Enrichment and Segregation Effects in Pt–Ni Alloy Nanoparticle Fuel Cell Catalysts*", ACS Catalysis **2017**, *7* (9), 6376–6384, DOI: 10.1021/acscatal.7b00996

R. Chattot, O. Le Bacq, V. Beermann, S. Kühl, J. Herranz, S. Henning, L. Kühn, T. Asset, L. Guétaz, G. Renou, J. Drnec, P. Bordet, A. Pasturel, A. Eychmüller, T. J. Schmidt, P. Strasser, L. Dubau, F. Maillard, "*Surface distortion as a unifying concept and descriptor in oxygen reduction reaction electrocatalysis*", Nature Materials **2018**, DOI: 10.1038/s41563-018-0133-2